Cone Beam Computed Tomography (CBCT) Dosimetry: Measurements and Monte Carlo Simulations

by

Sangroh Kim

Department of Medical Physics
Duke University

Date:_____

Approved:

_____
Terry T. Yoshizumi, PhD, Supervisor

_____
Fang-Fang Yin, PhD

_____
Shiva K. Das, PhD

_____
Donald P. Frush, MD

_____
Ehsan Samei, PhD

_____
Robert E. Reiman, MD

Dissertation submitted in partial fulfillment of
the requirements for the degree of Doctor of Philosophy in
the Department of Medical Physics in the
Graduate School of Duke University

2010

ABSTRACT

Cone Beam Computed Tomography (CBCT) Dosimetry:
Measurements and Monte Carlo Simulations

by

Sangroh Kim

Department of Medical Physics
Duke University

Date:_____
Approved:

_____
Terry T. Yoshizumi, PhD, Supervisor

_____
Fang-Fang Yin, PhD

_____
Shiva K. Das, PhD

_____
Donald P. Frush, MD

_____
Ehsan Samei, PhD

_____
Robert E. Reiman, MD

An abstract of a dissertation submitted in partial fulfillment of
the requirements for the degree of Doctor of Philosophy in
the Department of Medical Physics in the
Graduate School of Duke University

2010

ABTRACT

Cone beam computed tomography (CBCT) is a 3D x-ray imaging technique in which the x-ray beam is transmitted to an object with wide beam geometry producing a 2D image per projection. Due to its faster image acquisition time, wide coverage length per scan, and fewer motion artifacts, the CBCT system is rapidly replacing the conventional CT system and becoming popular in diagnostic and therapeutic radiology. However, there are few studies performed in CBCT dosimetry because of the absence of a standard dosimetric protocol for CBCT. Computed tomography dose index (CTDI), a standardized metric in conventional CT dosimetry, or direct organ dose measurements have been limitedly used in the CBCT dosimetry.

This dissertation investigated the CBCT dosimetry from the CTDI method to the organ, effective dose, risk estimations with physical measurements and Monte Carlo (MC) simulations.

An On-Board Imager (OBI, Varian Medical Systems, Palo Alto, CA) was used to perform old and new CBCT scan protocols. The new CBCT protocols introduced both partial and full angle scan modes while the old CBCT protocols only used the full angle mode. A metal-oxide-semiconductor-field-effect transistor (MOSFET) and an ion chamber were employed to measure the cone beam CTDI ($CTDI_{CB}$) in CT phantoms and organ dose in a 5-year-old pediatric anthropomorphic phantom. Radiochromic film was also employed to measure the axial dose profiles. A point dose method was used in the CTDI estimation.

The BEAMnrc/EGSnrc MC system was used to simulate the CBCT scans; the MC model of the OBI x-ray tube was built into the system and validated by measurements characterizing the cone beam quality in the aspects of the x-ray spectrum, half value layer (HVL) and dose profiles for both full-fan and half-fan modes. Using the validated MC model, $CTDI_{CB}$, dose profile integral (DPI), cone beam dose length product (DLP_{CB}), and organ doses were calculated with voxelized MC CT phantoms or anthropomorphic phantoms. Effective dose and radiation risks were estimated from the organ dose results.

The $CTDI_{CB}$ of the old protocols were found to be 84 and 45 mGy for standard dose, head and body protocols. The $CTDI_{CB}$ of the new protocols were found to be 6.0, 3.2, 29.0, 25.4, 23.8, and 7.7 mGy for the standard dose head, low dose head, high quality head, pelvis, pelvis spotlight, and low dose thorax protocols respectively. The new scan protocols were found to be advantageous in reducing the patient dose while offering acceptable image quality.

The mean effective dose (ED) was found to be 37.8 ±0.7 mSv for the standard head and 8.1±0.2 mSv for the low dose head protocols (old) in the 5-year-old phantom. The lifetime attributable risk (LAR) of cancer incidence ranged from 23 to 144 cases per 100,000 exposed persons for the standard-dose mode and from five to 31 cases per 100,000 exposed persons for the low-dose mode. The relative risk (RR) of cancer incidence ranged from 1.003 to 1.054 for the standard-dose mode and from 1.001 to 1.012 for the low-dose mode.

The MC method successfully estimated the $CTDI_{CB}$, organ and effective dose despite the heavy calculation time. The point dose method was found to be capable of estimating the CBCT dose with reasonable accuracy in the clinical environment.

DEDICATION

To my wife, Mingu, for her endless love and support, and my parents and brother, for their unconditional support.

CONTENTS

LIST OF TABLES

LIST OF FIGURES

Figure Page

LIST OF ABBREVIATIONS

1D	One-dimensional
2D	Two-dimensional
3D	Three-dimensional
BEAM	Monte Carlo code for particle transport (old version)
BEAMDP	BEAM data processor
BEAMnrc	Monte Carlo code for particle transport (NRC version)
BEIR	Biological Effects of Ionizing Radiation
BM	Bone marrow
CAVRZnrc	Monte Carlo code for cavity dose calculation (NRC version)
CBCT	Cone beam computed tomography
CBFFold	Cone beam full-fan protocol (old protocol)
CBHFold	Cone beam half-fan protocol (old protocol)
CBHQH	Cone beam high-quality head protocol
CBLDH	Cone beam low-dos head protocol
CBLDT	Cone beam low-dose thorax protocol
CBPEL	Cone beam pelvis protocol
CBPSL	Cone beam pelvis spotlight protocol
CBSDH	Cone beam standard-dose head protocol
CM	Component module
CPU	Central processing unit
CT	Computed tomography
CTCREATE	BEAMnrc user code for MC phantom generation
CTDI	Computed tomography dose index

$CTDI_{2D}$	Computed tomography dose index from center slice dose averaging
$CTDI_{3D}$	Computed tomography dose index from 3D volume dose averaging
$CTDI_{a}$	Computed tomography dose index proposed by Dixon et al
$CTDI_{CB}$	Computed tomography dose index for CBCT scan
$CTDI_{L}$	Computed tomography dose index proposed by Mori et al
$CTDI_{w}$	Weighted computed tomography dose index
$CTDI_{wb}$	Computed tomography dose index calculated by Bakalyar's method
CTP	Catphan (image quality analysis phantom)
DBS	Directional bremsstrahlung splitting
DICOM	Digital imaging and communications in medicine
DLI	Dose line integral
DLP	Dose length product
DLP_{CB}	Dose length product for CBCT scan
DOSXYZ_SHOW	BEAMnrc user code for 3D phantom and dose visualization
DOSXYZnrc	Monte Carlo code for dose calculation in voxels (NRC version)
DPI	Dose profile integral
ECUT	Electron cutoff energy
ED	Effective dose
EGS4	Electron gamma shower Monte Carlo engine (Version 4)
EGSnrc	Electron gamma shower Monte Carlo engine (NRC version)
FDA	Food and drug administration
GB	Giga-byte
GE	General electric
GHz	Giga-hertz
HU	Hounsfield unit

HVL	Half value layer
ICRP	International commission on radiological protection
ICRU	International commission on radiation units and measurements
IGRT	Image guided radiation therapy
IPEM	Institute of physics and engineering in medicine
keV	Kilo-electron volt
kV	Kilovoltage
kVp	Kilovoltage peak
LAR	Lifetime attributable risk
LDPE	Low-density polyethylene
mA	Milli-ampere (tube current unit)
mAs	Milli-ampere-second (tube current time product unit)
MATLAB	A computer software for matrix calculation
MC	Monte Carlo
MDCT	multi-detector computed tomography
MeV	Mega-electron volt
MOSFET	Metal-oxide-semiconductor field-effect transistor
msec	Milli-second
MSAD	Multiple scan average dose
MV	Megavoltage
NF	Normalized factor
NIST	National institute of standards and technology
NOD	Net optical density
NP	Number of projection
NRC	National Research Council

OBI	On-board imager
OMEGA	Ottawa-Madison electron gamma algorithm
PCUT	Photon cutoff energy
PEGS4	Preprocessor for EGS (Material generator for EGS)
PET	Positron Emission Tomography
PMMA	Polymethyl-methacrylate
PMP	Polymethylpentene
POLYFIT	A MATLAB function of polynomial fitting
PV	Pixel value
QA	Quality assurance
RAM	Random-access memory
RGB	Red-green-blue
ROI	Region of interest
RR	Relative risk
RT	Radiation therapy
SBS	Selective bremsstrahlung splitting
SID	Source to isocenter distance
SSD	Source to surface distance
STATDOSE	BEAMnrc user code for dose profile analysis
TLD	Thermoluminescent dosimeter
UBS	Uniform bremsstrahlung splitting
$_{w}CTDI_{CB}$	Weighted cone beam computed tomography dose index
$_{w}DPI$	Weighted dose profile integral
XCOM	Photon cross sections database of NIST
XVI	X-ray volume imaging (Elekta system)

ACKNOWLEDGEMENTS

This work would never have been completed without the tremendous support and sacrifice from my family, friends, colleagues and mentors. I would like to express my sincere appreciation to them with all my heart for their kind, warm, and unconditional support. They have enriched my five years at Duke; this I will never forget.

First, I owe the most gratitude to my lovely wife, Mingu, who experienced all the hard times and challenges as well as the beautiful and happy days here with me. She always guided me the right way when I was wandering and struggling with some problems. With her warm love and wholehearted support, I was able to explore this long journey to the academic professional without any fear. I would like to give this back to her when she starts her own career.

I also would like to thank my parents and elder brother who made this study-abroad possible. With their encouragement and concrete trust on me, I was able to decide to initiate my academic career and finish my studies in the US. They have always provided me with invaluable wisdom and insights with unconditional support.

My advisor, Dr. Terry Yoshizumi, I want to sincerely thank you for your consistent support and guidance. During these five years, you taught me not only academic knowledge but also the art of living so I could survive here very well. You also have always inspired me to explore diverse research topics, which have strengthened my research ability. You have been a truly great mentor and a good friend as well.

To Greta Toncheva, you have been a great supporter and I would like to show my appreciation for all the help you gave me during this study. You supported many difficult experiments without a single complaint; those efforts became fundamental for my study.

To Dr. Shiva Das, you are an admirable mentor as well as a good friend. With your warm and kind heart, I could discuss any of my difficulties with you and find the solutions. You also enlightened me a lot with your beautiful engineering and physics mind. I truly appreciate all the things you gave to me.

To Dr. Fang-Fang Yin, your consistent support made it possible for me to complete this study. You are a truly great mentor and a respectful director. I appreciate all of your help.

To Dr. Sua Yoo, you helped me endlessly without any doubt even with your busy schedule. I would like to sincerely thank you for all your support.

To Drs. Donald Frush, Ehsan Samei, and Robert Reiman, I can't say enough to thank all of you. Without your guidance, this work definitely would not have been possible. You fully supported me while involved with your busy schedules and I will never forget your kindness. Thank you.

To my colleagues and friends, you filled my life with happiness, fun and excitement. Because of you, I was able to make my life more colorful with you. The invaluable memories we had together will always be with me. Thank you.

Chapter 4 and 5 is related to the paper to be published in Health Physics: S. Kim, T. Yoshizumi, G. Toncheva, S. Yoo, F. Yin, and D. Frush, "Estimation of computed tomography dose index in cone beam computed tomography: MOSFET measurements and Monte Carlo simulations."

Chapter 6 is related to the paper to be published in Medical Physics: S. Kim, S. Yoo, F. Yin, E. Samei, and T. Yoshizumi, "Kilovoltage cone-beam CT: comparative dose and image quality evaluations in partial and full-angle scan protocols."

Chapter 7 is related to the paper to be submitted to Medical Physics: S. Kim, H. Song, E. Samei, F. Yin, and T. Yoshizumi, "Computed tomography dose index and dose length product for cone-beam CT: Monte Carlo simulations of a commercial system."

Chapter 8 is related to the published paper: S. Kim, T. Yoshizumi, G. Toncheva, D. Frush, and F. Yin, "Estimation of Absorbed Doses from Pediatric Cone-Beam CT Scans: MOSFET Measurements and Monte Carlo Simulations," Radiat. Prot. Dosim. Advance access published on Nov. 4, (2009).

Chapter 9 is related to the published paper: S. Kim, T. Yoshizumi, G. Toncheva, F. Yin, and D. Frush, "Radiation Dose from Cone Beam Computed Tomography in a Pediatric Phantom: Risk Estimation of Cancer Incidence," Am. J. Roent. 194, 1-5 (2010).

This PhD study has been funded in part by the U.S. Nuclear Regulatory Commission Nuclear Education Grant (NRC-38-07-494), General Electric CT Research Grant, and Carestream Graduate Fellowship.

1. INTRODUCTION

Since Sir Hounsfield invented the computed tomography (CT) scanner in 1972, CT technology has rapidly advanced in several aspects; first, the image acquisition speed has been enormously improved from approximately ten days to a few seconds. [1] Second, the image resolution of a CT scan has been improved from 80×80 pixels to 512×512 or even 1024×1024 pixels in high resolution.[2] Third, the CT system geometry has been improved from the first generation (pencil beam geometry) to the seventh generation[2] (multi-detector cone beam geometry). Beside these major improvements, current CT technology still advances in order to produce best quality of the images introducing the dual energy technique and the high-resolution detectors.

CT imaging is widely used today for multiple applications in the subfields of radiology, in nuclear medicine, and in cardiology: e.g. multi-detector CT (MDCT) in diagnostic radiology, CT fluoroscopy in interventional radiology, positron emission tomography (PET)/CT applications in nuclear medicine. In cardiology, a 320-slice multi-detector CT (model: Aquilion ONE, Toshiba America Medical Systems, Tustin, CA) is commercially available for cardiac CT imaging. This CT system can cover the entire size of the heart (16 cm) for one single rotation per second, so it can almost perfectly reduce the motion artifact of the heart.

Since 1993, the number of CT examinations has been dramatically increased in diagnostic radiology by ~ 10% per year. [3] As reported in 2006, 67 million CT

examinations are performed annually in the U.S. and now; CT covers half of the collective dose in all diagnostic x-ray modalities.[3] Because CT uses the x-ray with the photon energy ranging from 80 to 140 kVp with multiple projections, the radiation dose to the patient is a concern. Note that general 360 degree CT imaging results in approximately 1000 projections and total tube current time of 200 mAs per rotation with the effective photon energy of 60-70 keV. As a result, the average effective dose from CT imaging is roughly 100-250 times higher than that of regular chest x-ray imaging. Because of the significant dose contribution, the radiation dose of the CT examinations should be carefully monitored and the CT scan techniques need to be optimized to reduce the patient dose.

Shope et al.[4] proposed the CT dose index (CTDI) concept in order to establish a convenient dose measure for a single slice CT system in 1981. The conventional CTDI is defined as follows:

$$CTDI = \frac{1}{nT}\int_{-z}^{+z} D(z)dz, \tag{1}$$

where n = number of slices per single rotation,
T = thickness of a slice,
z = range of the axial profile measurement

This quantity is well known as $CTDI_{FDA}$ (2z range of profile measurement); there are other variants such as $CTDI_{100}$ (10 cm range) and $CTDI_{\infty}$ (infinitesimal range). It should be mentioned that there are no conceptual differences among these quantities. Note that Shope et al.'s original suggestion was $CTDI_{\infty}$, which fully contains the whole

tail portion of the CT profile. Due to the technical convenience of the CT chamber measurements, $CTDI_{100}$ has been generally used as a standard these days. The $CTDI_{100}$ is typically measured by a 10 cm pencil ion chamber or thermoluminescent dosimters (TLD) with CT phantoms. Usually two sizes of cylinder phantoms (head and body), made of a polymethyl-methacrylate (PMMA) material, are used in this CT dosimetry. The 10 cm pencil ion chamber, located at the center and peripheries in the phantom, collects all the ionization longitudinally generated inside the chamber within the range of 10 cm. The TLD can also measure the longitudinal profile dose at individual locations. These point doses can be integrated over the range of the profile as the definition of the $CTDI_{100}$. Note that the original idea of the CTDI was (1) to integrate all the longitudinal ionization per single rotation at the center of the CT phantom, and (2) to normalize the integration by nominal beam width, in order to standardize it as a reference dosimetric quantity in a single slice CT scan.

As briefly aforementioned, the CT technology has advanced in the direction of widening the beam width; this created the capability of acquiring a larger imaging area with fewer numbers of scans, while reducing the scan duration. Despite all the benefits of the wide beam CT system, this wide beam geometry (i.e. cone beam geometry) introduced the difficulty of patient dosimetry because the conventional CTDI concept is not directly applicable to the cone beam CT (CBCT) geometry for the purpose of accurate radiation dose estimation in the phantoms. The reason for this is that the ionization created by a wide cone beam can not completely be collected without any loss

by a conventional CT pencil ion chamber; the wide cone beam creates a longer CT profile (approximately 30-100 cm). This makes it difficult for the current pencil ion chamber to physically cover the entire length. Even if one could create such a long pencil ion chamber, there would be many technical problems such as electron collection efficiency, electric field inhomogeneity, charged particle equilibrium, and so forth. Additionally, longer CT phantoms would also be needed for the measurements.

Much research has been performed to evaluate the limitation of the direct application of CTDI to CBCT dosimetry. Mori et al.[5] studied the beam width effect on a 256 slice CT and found that the length of the body phantom needs to be larger than 300 mm to collect 90% of the dose profile integral if the beam width is over 20 mm. Boone[6] found from his Monte Carlo simulations that the use of $CTDI_{100}$ even for a 10 mm slice thickness is not efficient.

Dixon[7] suggested a point dose measurement to estimate the CTDI by scanning the entire CT phantom long enough to establish the dose equilibrium using a small ion chamber to overcome the limitation of the 100 mm pencil ion chamber. The rationale is that a multiple scanning process generates the dose equilibrium that would be equivalent to the multiple scan average dose (MSAD). Thus, by measuring a point dose in the dose equilibrium region, a CTDI could be derived that is equivalent to the MSAD described in Shope's study.[4] Nakonechny et al.[8] measured the CTDI with a diamond detector with the point dose measurement. Song et al.[9] also evaluated the CTDI values for XVI and OBI CBCT systems using an Farmer type ion chamber following the point dose measurements.

Apparently Dixon's method can also be applied to the CBCT geometry. However, there is no extensive research that has been performed for this methodology; therefore it is not understood how well the point dose method could estimate the CTDI in the CBCT geometry compared to the estimation from the original CBCT concept.

As the beam collimation is becoming wider in CBCT, the number of scatter photons increases and proportionally the length of the CT phantom should be increased in order to collect all the scatter photons inside the phantom for the accurate CT dosimetry. In addition, there is a physical and experimental limitation that exists to measure the CT dose accurately – that is, the length limitations of the CT phantom and the pencil ion chamber.

To overcome these limitations, the Monte Carlo (MC) technique can be used for the accurate CBCT dosimetry. MC simulation has been widely used in radiation therapy applications for its calculation accuracy and high speed computing power. Especially, BEAMnrc/EGSnrc (NRCC, Canada) MC code[10,11] has been validated for the simulations of medical linear accelerator and x-ray treatment units. Jarry et al.[12] used the BEAMnrc/EGSnrc code to investigate the scatter contribution in kV CBCT. Ding et al.[13] established a MC model of OBI and investigated the characteristics of the kilovoltage x-ray beam. They also applied their model to patient dosimetry in radiation therapy.[14] However, they did not apply their model to the CTDI calculations.

In this study, the applicability of the MC method to the CBCT dosimetry has been investigated from the CTDI to organ/effective dose estimation of an anthropomorphic phantom using the BEAMnrc/EGSnrc MC system.

2. SPECIFIC AIMS

The purpose of this study is to investigate the CBCT dosimetry – cone beam CTDI ($CTDI_{CB}$), organ/effective dose and risk estimation – using the BEAMnrc/EGSnrc MC system. To achieve this, this study has followed several steps: (1) MC model validation in the aspect of beam output (beam quality) – x-ray spectrum and half-value layer (HVL), and tube geometry with lateral and depth dose profiles, (2) cone beam CTDI dose simulations with the MC model and physical measurements with metal-oxide-semiconductor-field-effect transistor (MOSFET) detectors for 360 degree full angle rotation (old protocol), (3) cone beam CTDI dose simulations with the MC model and physical measurements with an ion chamber detector for partial-angle (200 degree) rotation (new protocol), (4) cone beam CTDI ($CTDI_{CB}$) and cone beam dose length product (DLP_{CB}) estimations with the MC simulations, (5) Organ/effective dose estimation in an anthropomorphic phantom with the MOSFET measurements and the MC simulations, and (6) Risk estimation of cancer incidence in an anthropomorphic phantom with the MOSFET measurements.

Each topic includes its own goal, which can be an essential ingredient for the full investigation of the CBCT dosimetry.

3. CLINICAL SIGNIFICANCE

Owing to the advanced modern technologies – the powerful x-ray tube, flat-panel detector, and novel image reconstruction algorithm – image guidance applications to medicine are becoming popular to improve the quality of the patient's healthcare. In diagnostic radiology, the multi-detector CT (MDCT) imaging technique has emerged and is used for diagnosis purposes or image guidance such as CT fluoroscopy. Highly penetrating photon beams generated from a powerful CT x-ray tube can help a physician to more accurately locate his/her medical apparatus inside a patient's body. In cardiology, a few institutions started to use the 320-slice CT system acquiring a patient's heart images without motion artifacts. This system can also improve cardiac and brain perfusion studies due to the scanner's ability to dynamically visualize organs and blood flow. 16 cm wide coverage of the scanner removed the stitching artifact as well as reduced the radiation dose. In interventional radiology, the C-arm CBCT system also became usable to improve the localization of the needle for aneurysm and stenosis treatments. In radiation oncology, CBCT imaging has started to minimize the patient's localization error for image guided radiation therapy (IGRT). This IGRT application includes not only external radiation therapy but also brachytherapy; radioisotope seeds can be more accurately placed with the help of image guidance.

Since CBCT imaging is relatively a new imaging modality, the dosimetric study for CBCT is still limited. From the conventional CT dosimetric approach, some

researchers[5,6] have investigated the applicability of the original CTDI concept for CBCT dosimetry. They found that a direct application of the CTDI to the CBCT dosimetry is inappropriate due to the limitation of the physical measurement system in the original CTDI; the 10 cm long pencil ion chamber is unable to collect the tail portion of the ionizations in the 15 cm long CT phantoms. Although Dixon[7] proposed a point dose measurement method to avoid this limitation, there is still no consensus about how to accurately evaluate the CBCT doses. Thus, it would be of a great interest to investigate a methodology for CBCT dosimetry in order to accurately estimate the CBCT dose to the patient and to reduce the dose if possible.

To overcome the limitation of the physical measurements in CBCT dosimetry, the MC method is introduced to estimate the CBCT doses in this study. The MC method is a powerful tool to simulate a physical phenomenon, governed by random events, using a stochastic approach. In the MC simulations of particle physics, computer-generated pseudo-random numbers are used in simulating the random walks of the particle transports. Although it might be slightly different depending on the kind of MC system and computing power, it generally takes moderate computation time (a few hours to weeks) for a personal computer to achieve reasonable accuracy (about 2-5%) in the particle transport MC simulations. Much research[15-20] has been performed in various ways to reduce the computation time. In software engineering approaches, some studies have introduced several variance reduction techniques in biasing the simulation results. Fundamentally, they are categorized into two general concepts: particle splitting and

Russian roulette (particle killing).[19,20] This kind of biasing technique can also be applied not only to the number of particle splittings but also to the geometry of the particle direction and location; Kawrakow et al.[21] developed a variance reduction technique called "Directional Bremsstrahlung Splitting (DBS)," which splits the bremsstrahlung photons within a certain area to maximize the efficiency of the splitting techniques. They reported that the use of DBS can result in 8 to 20 times higher efficiency than Selective Bremsstrahlung Splitting (SBS) and Uniform Bremsstrahlung Splitting (UBS) in a 6 MV photon beam (10×10 cm^2 field) fluence simulation. [21]

A similar improvement in electron fluence efficiency was also reported. For the total dose efficiency in a central-axis depth-dose curve, a factor of 6.4 improvements over SBS at all depths in the phantom was reported. [21] In sum, all these advanced variance reduction techniques have helped to significantly reduce the computation times in MC simulations.

Nowadays, CBCT dosimetry is becoming important because of its widespread applications as described above. In this study, the MC technique was employed to overcome the limitation of current CBCT dosimetry; the cone beam CTDI ($CTDI_{CB}$) was evaluated by using the point dose method with MC as well as physical measurements; the cone beam dose length product (DLP_{CB}) was estimated from the $CTDI_{CB}$ and its accuracy was validated by comparing the results of the dose profile integral (DPI) method. This methodology, which can be applicable not only to the CBCT dosimetry but also to the MDCT and interventional dosimetry, could improve the accuracy of all kinds of wide

beam x-ray systems' dose estimation removing cumbersome and labor intensive physical measurements.

4. MONTE CARLO MODEL OF OBI X-RAY TUBE

4.1. Introduction

The Monte Carlo (MC) technique is a stochastic approach to finding a numerical solution to a problem that involves object interaction with other objects or their environments.[18] It models physical phenomena of the objects in mathematical expressions and simulates them by using a random sampling method. It has been widely used to solve complex problems in many scientific fields that deterministic approaches cannot easily solve. Especially in particle transport problems, it simulates the random trajectories of individual particles by using machine-generated (pseudo-) random numbers to sample the probability distributions governing the physical processes involved. By simulating a large number of particle histories, information can be obtained about average values of macroscopic quantities such as energy deposition of the particle or microscopic quantities of statistical fluctuations in particular kinds of events.[22] In 1940s, Von Neumann and Ulam firstly started to use the MC method for a scientific purpose – to estimate neutron diffusion behavior in fission material.

To solve the particle transport problem with the MC method, a time-independent linear Boltzmann transport equation is usually used[23]. The general form of the Boltzmann equation is described as follows:

$$\psi(\vec{r},\vec{v}) = \int\left[\int \psi(\vec{r}\,',\vec{v}\,')C(\vec{v}\,' \to \vec{v},\vec{r}\,')d\vec{v}\,' + Q(\vec{r}\,',\vec{v})\right]T(\vec{r}\,' \to \vec{r},\vec{v})d\vec{r}\,', \tag{2}$$

where $\psi(\vec{r},\vec{v})$ = particle collision density (angular flux)

$Q(\vec{r}\,',\vec{v})$ = source term

$C(\vec{v}\,' \to \vec{v},\vec{r}\,')$ = collision kernel

$T(\vec{r}\,' \to \vec{r},\vec{v})$ = transport kernel

There are several assumptions that must be made to use this equation – static, homogeneous medium, time-independent linear system, Markovian, no interactions between particles, etc.

Because a particle interacts (collides) with the medium several times before it stops, a superposition principle can be used to explain the whole particle track. For example, let a particle $p(\vec{r},\vec{v})$ interacts based on the combined kernel $R(p' \to p) = C(\vec{v}\,' \to \vec{v},\vec{r}\,')T(\vec{r}\,' \to \vec{r},\vec{v})$. Then, the angular flux of the particle $\psi(p)$ can be extended into the components having 0, 1, 2, …, k collisions $\psi(p) = \sum_{k=0}^{\infty}\psi_k(p)$ with $\psi_0(p) = \int Q(\vec{r}\,',\vec{v})T(\vec{r}\,' \to \vec{r},\vec{v})d\vec{r}\,'$ and $\psi_k(p) = \int \psi_{k-1}(p')\cdot R(p' \to p)dp'$. Note that collision k depends only on the results of previous collision k-1. After the angular flux is substituted for each collision with the previous flux, the following equation can be derived:

$$\begin{aligned}\psi_k(p) &= \int \psi_{k-1}(p')\cdot R(p' \to p)dp' \\ &= \int\ldots\int \psi_0(p_0)\cdot R(p_0 \to p_1)\cdot R(p_1 \to p_2)\ldots R(p_{k-1} \to p)dp_0\ldots dp_{k-1}\end{aligned} \tag{3}$$

To apply the MC method to the above equation, two steps need to be performed – (1) generation of a sequence of particle states ($p_0, p_1, p_2, \cdots$) by randomly sampling the angular flux $\psi_0(p_0)$ and the combined kernel $R(p_{k-1} \rightarrow p_k)$ from each probability density function, and (2) generation of the total estimate by averaging individual particle estimates for M histories as following equation:

$$A_{total} = \int A(p) \cdot \psi(p) dp \approx \frac{1}{M} \sum_{m=1}^{M} \left(\sum_{k=1}^{\infty} A(p_{k,m}) \right), \quad (4)$$

where A = estimate of individual particle state,

A_{total} = total estimate

The EGS4 based BEAM MC system was developed from the OMEGA project, which was a joint work done by the National Council Research (NRC, Canada) and the University of Wisconsin Madison, in order to simulate the radiation beams from radiotherapy units including high-energy electron and photon beams ^{60}Co beams and orthovoltage units.[10,24] Although BEAM was developed for the purpose of medical linear accelerator simulation, BEAM also has the capability of simulating the beam output of a diagnostic x-ray tube; the XTUBE component module (CM) can be used to model an anode target of a diagnostic x-ray tube.[11,25]

4.2. Materials and methods

The BEAMnrc/EGSnrc system (Version 05) was established to simulate the OBI head based on the specifications provided by the manufacturer. A G242 x-ray tube model

(Varian Medical Systems, Palo Alto, CA) was built using XTUBE CM with a pure tungsten target, CONSTAK CM for the tube exit window, JAWS CM for the blades (i.e. collimators), and SLABS CM for the window of the On-board Imager®. For both full-bowtie and half-bowtie filters, we employed JAWS CM. The detailed geometries for the "full-fan" and "half-fan" modes are shown in FIG. 1. Note that the "full-fan" and "half-fan" modes have different blade openings.

Two procedures were performed to validate the MC model – beam quality assurance and tube geometry verification. For the beam quality check, 6 cm^3 ion chamber responses were simulated by varying the thickness of aluminum filters in the narrow beam geometry to estimate the HVL of the x-ray system without bowtie filters. This was compared to the ion chamber measurements as well as from the previous study by Ding et al.[13] and the data from the IPEM report 78.[26] The aluminum filters used were located fairly close to the x-ray tube so that the backscatter from the filter to the ion chamber was minimized. The HVL was simulated from 0 mm to 6 mm Al thickness with 1 mm step. The step size was reduced to 0.2 mm in the range of 4 mm to 5 mm Al where the expected HVL exists. In order to simulate the ion chamber response, CAVRZnrc user code[27] was employed to calculate the absorbed dose in the air cavity of the chamber.

Lateral profiles and depth doses were measured in a water tank to verify the geometry of the OBI head - especially the location of bowtie filters in the MC model. As shown in FIG. 2, a large water tank (MT-150, CIVCO medical solutions, Kalona, IA) was employed with a manual depth dose system.

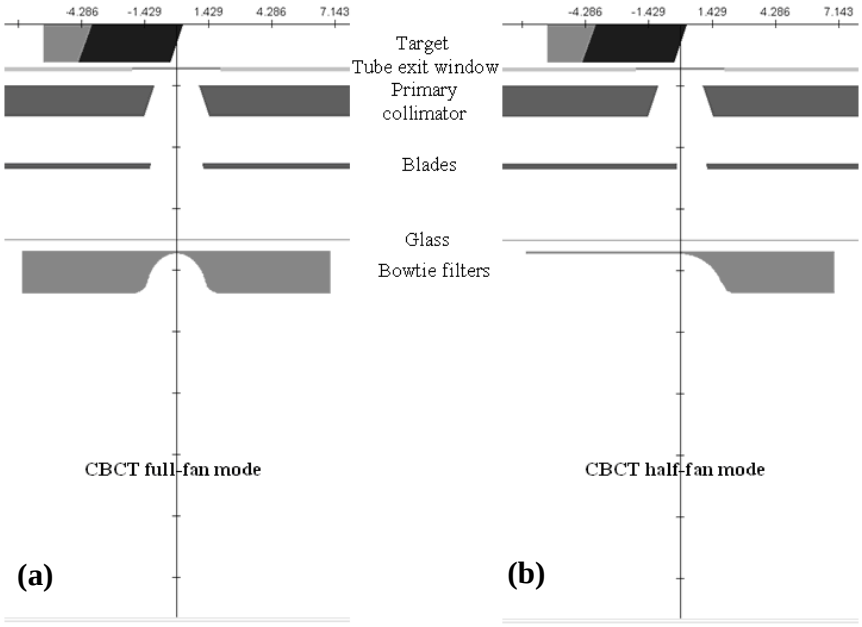

FIG. 1. Varian On-board Imager® x-ray tube geometries for full-fan mode and half-fan mode in BEAMnrc. (a) Full-fan mode uses full bowtie filter, and (b) half bowtie filter is used for half-fan mode.

(FC65-P/BNC, IBA dosimetry GmbH, Schwarzenbruck, Germany) was also used with an electrometer (model 35040, Cardinal Health, Dublin, OH). The lateral profiles without bowtie, with full bowtie filter, and with half bowtie filter were scanned at a 3 cm depth below the water surface; the depth dose profiles for each filter mode were acquired at the central axis. Because it was intended to compare the output of MC simulations to the measurements of relative dosimetry, only the readings of charges were collected from the electrometer without considering calibration factors necessary for an absolute dosimetry.

FIG. 2. Lateral and depth dose profile measurement setup with a water tank and an ion chamber.

To validate the tube geometry, especially the location of the bowtie filters, MC simulations of the same profile experiments were performed. A 125 keV mono-energetic electron beam with a 0.6 mm diameter circular shape was impinged to the tungsten target

to generate the bremsstrahlung x-rays in BEAMnrc simulations. The number of histories was set to 200 million to achieve the reasonable statistics of the particle fluence within 2%. A phase space file was acquired at the source to surface distance (SSD) of 100 cm.

Mainegra-Hing and Kawraokow[25] have reported the inefficiency of x-ray tube MC simulations without variance reduction techniques due to the small number of bremsstrahlung photons produced from low energy incident electrons. To increase the simulation efficiency, the following variance reduction techniques were applied to the simulations recommended by them[25]: (1) a directional bremsstrahlung splitting number of 10,000 with 1MeV range rejection technique, (2) Electron impact ionization, (3) bound Compton scattering, (4) photoelectron angular sampling, (5) Rayleigh scattering, and (6) Atomic relaxation. In addition, simple bremsstrahlung angular sampling was also used. For the bremsstrahlung cross sections, the National Institute of Standards and Technology (NIST) data was used for all simulations and XCOM data[28,29] was used for photoabsorption and Rayleigh scattering cross sections. An electron splitting method was also used to prevent high-weighted electrons from interacting with other tube component's materials. To obtain the best simulations, both electrons and photons were tracked down to the threshold energy of 1 keV. To reduce these cutoff energies in different materials, all the material data were reproduced by using PEGS4 user code.[30]

After BEAMnrc simulations were finished, the phase space files from BEAMnrc were used to run DOSXYZnrc user code[31] to calculate the absorbed dose in the phantoms. A simple rectangular voxel phantom was assigned to calculate the dose distribution in

water. The dimension was 40×40×35 cm^3. The number of histories was assigned as nine billion in order to obtain reasonably smooth profiles in DOSXYZnrc simulations. Just as with the ion chamber measurements, the lateral profiles were plotted at 3 cm below the water surface and the depth dose profiles was obtained at the central axis.

4.3. Results and discussion

The HVL obtained from the MC simulation was 4.4 mm Al, which is the same as that generated by Ding et al. [13] and IPEM report 78. [26] Slight differences were found beyond the aluminum filter thickness of 5 mm (FIG. 3); this can be explained by the interpolation errors between the two datasets.

The x-ray spectrum data obtained from our simulations were also compared to the data of the IPEM report 78 with the filter parameters provided by the manufacturer. The spectrum was simulated following the same protocol and tube geometry used in the head scan without bowtie filters. BEAMDP (BEAM Data Processor) user code[32] was used to analyze the phase space files acquired from BEAMnrc simulations. The x-ray spectrum acquired by the BEAMnrc simulation was normalized to the IPEM spectrum at the maximum number of photons disregarding k-edge characteristic x-rays. Results indicated that the two x-ray spectra were very well matched over the entire energy range including both k-alpha1 (59.31 keV) and k beta1 (67.23 keV) peaks[33] as shown in FIG. 4.

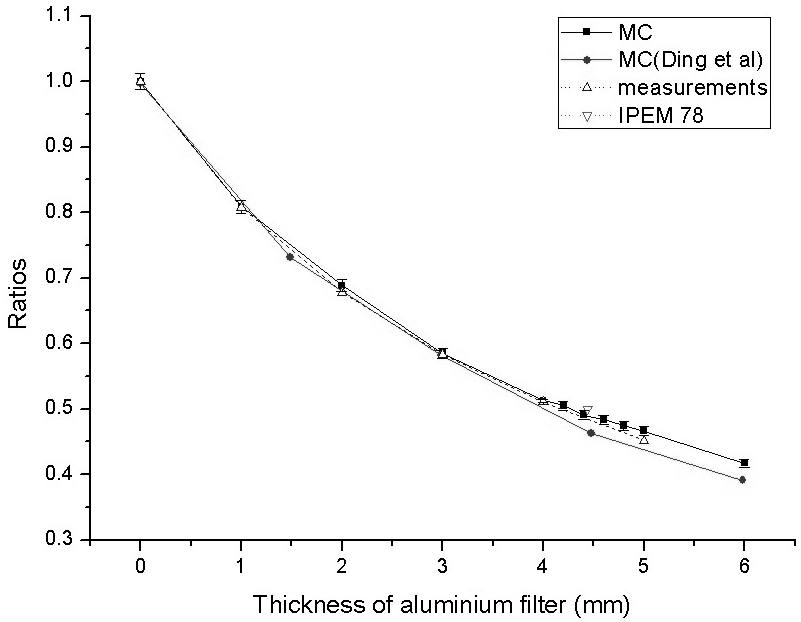

FIG. 3. Comparison of HVL MC data with ion chamber measurements, MC data of Ding et al. and IPEM report 78. The three curves are quite well matched in the overall ranges but MC data of Ding et al. shows lower ratios in the range over 4.6 mm Al. Note that the data of IPEM report 78 is a point value.

The mean energies (keV) of both x-ray spectra were calculated using the following equation.

$$E_{mean} = \frac{\sum_{i=1}^{N_{bin}} E_i \times N_i}{\sum_{i=1}^{N_{bin}} N_i}, \tag{5}$$

where E_i = photon energy of i_{th} bin,

N_i = number of photon in i_{th} bin and

N_{bin} = total number of bin

From the results, the difference of the mean energy of the photon was 0.01 keV - 55.6 keV from the IPEM report 78 and 55.5 keV from the MC simulation.

In the results, the central axis dose was set to unity and other readings were normalized corresponding to the dose for both ion chamber measurements and MC simulations in lateral profiles. For the depth dose profiles, the maximum point dose in the ion chamber measurements was set to unity and all other readings were scaled from that point. As shown in FIG. 5, all the data obtained from MC were well matched with the ion chamber measurements within 2% except the no bowtie case was within 3%. Note that the no bowtie case (FIG. 5 (a)) produced the highest discrepancy while the full bowtie and half bowtie cases (FIG. 5 (b), (c)) showed very good matches. This may be caused by the slight difference in target angle between the actual target and the target in MC. In depth dose profiles, some discrepancies at the buildup region were founded (FIG. 5 (d)).

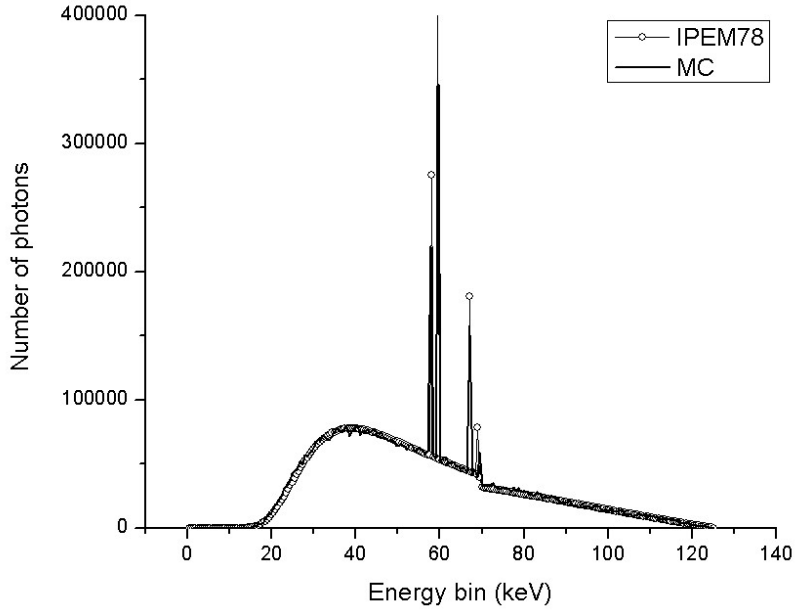

FIG. 4. Comparison of x-ray spectra between IPEM report 78 data and MC simulation.

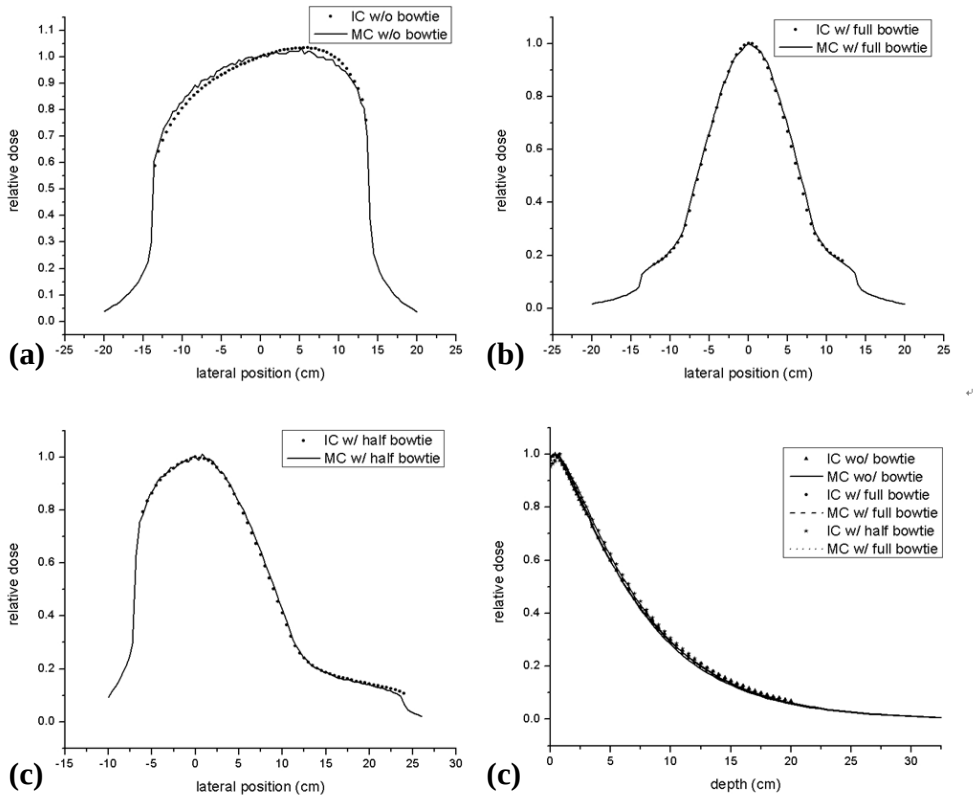

FIG. 5. Comparison of lateral and depth dose profiles with and without bowtie filters between ion chamber measurements and MC. (a) lateral profile without bowtie filter, (b) lateral profile with full bowtie filter, (c) lateral profile with half bowtie filter, and (d) depth dose profiles for all the cases.

This is caused by the effect of the buildup cap in the ion chamber. The dimension of the buildup cap was not negligible (several mm) while the active volume of the chamber was small. However, after ~4 mm depth, the depth dose profiles of MC were well matched with the MOSFET measurements.

5. CONE BEAM CTDI SIMULATIONS/MEASUREMENTS (Old Protocol)

Point doses and weighted CTDI ($CTDI_w$) of the CBCT imaging procedures were estimated from MOSFET measurements and MC simulations. These data were also compared with the results of Song et al.[9] to verify the applicability of the MOSFET technology and Monte Carlo (MC) method in CBCT dosimetry.

5.1. MOSFET measurements

The point doses were measured in the cylindrical phantoms using an On-Board Imager® (Varian Medical Systems, Palo Alto, CA). This imaging system consisted of a kilovoltage x-ray source and kilovoltage amorphous silicon detector orthogonally mounted on the linear accelerator.[34] The phantoms were made of polymethyl-methacrylate (PMMA) with density, ρ=1.19 g cm^{-3}. The head phantom has a diameter of 16 cm and the body phantom has a diameter of 32 cm. Both phantoms have the same axial length of 15.2 cm.

Using the imaging system, the head phantom was scanned with “full-fan” mode, a typical cone-beam scanning method, whereas “half-fan” mode was used for the body phantom. In the “half-fan” mode, the kilovoltage amorphous silicon detector was shifted by 14.8 cm laterally so that the opening of the blades was automatically adjusted corresponding to the location of the detector[34] as shown in FIG. 6.

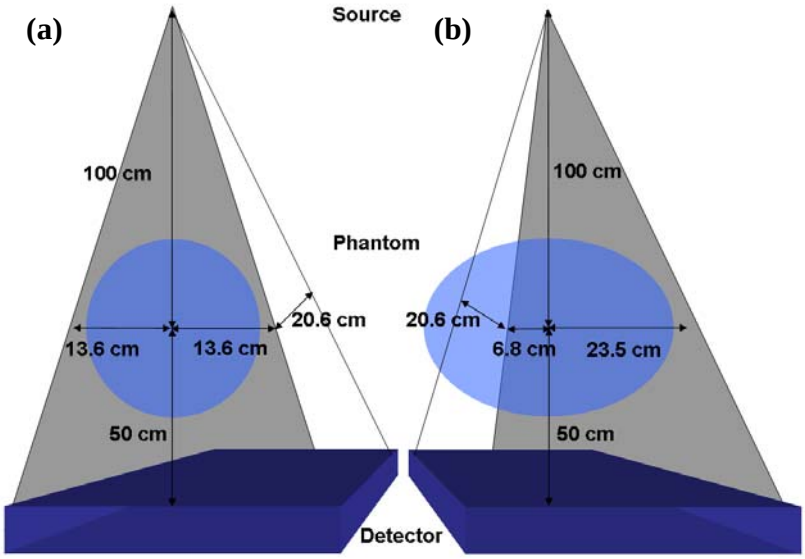

FIG. 6. Schematic diagram of "full-fan" and "half-fan" mode. (a) Full-fan mode was used for head phantom scan and (b) half-fan mode was used for body phantom scan.

For both head and body scans, two x-ray source parameters were used for the pulsed x-ray beam: standard dose mode with peak voltage of 125 kVp, tube current of 80 mA, and exposure time of 25 msec and low dose mode with the same kVp, 40 mA and 10 msec. Other CBCT scan parameters include focal size: 0.4~0.8 mm, source to image distance of 100 cm, total number of projections: 650-700, field of view: 25×25 cm^2 (head scan), 40×40 cm^2 (body scan), filters: full bowtie (head scan), half bowtie (body scan). The MOSFET detectors were calibrated by adding a 1.5 mm aluminum filter to a conventional radiographic x-ray tube - HVL 4.2 mm Al, to approximate the beam quality measured for the CBCT. Individual MOSFET detectors were calibrated with a 6 cm^3 ion chamber (Model: 10x5-6, Radcal, Monrovia, CA). Ten high sensitivity diagnostic

radiology MOSFET detectors (Model: TN-1002RD, Best Medical Canada, Ottawa, Canada) with AutoSense System (Model: TN-RD-49, Best Medical Canada) were employed to measure the point doses in the air at each measurement point. Identical experimental setups were used for both head and body phantoms. Two MOSFETs were placed parallel to the longitudinal axis at the midpoint of each of five cylindrical cavities, which were positioned at 3, 6, 9, 12 o'clock, and at the center. Each measured value represented the average of the two MOSFET readings located at the midpoint of each cavity. The experimental setting for the head phantom with MOSFET dosimeters is shown in FIG. 7. MOSFET Readers were connected to a personal computer via RS-232 cable and data were read immediately after the scan.

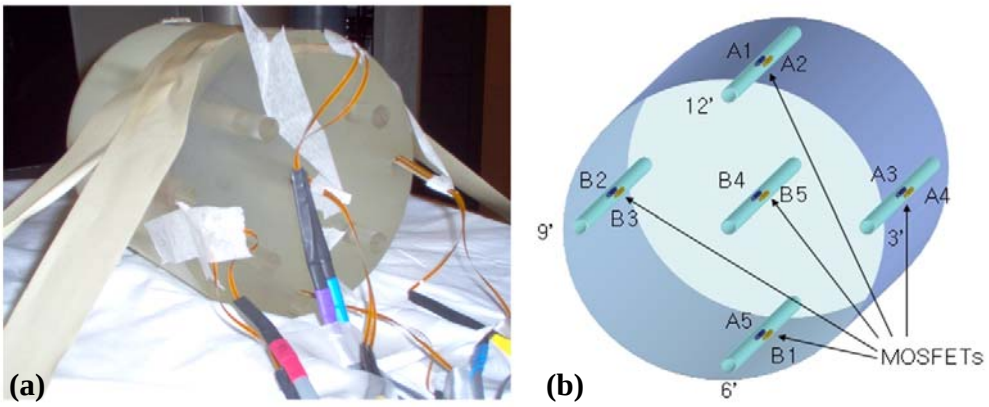

FIG. 7. PMMA head phantom and MOSFET set-up. (a) PMMA head phantom installed with MOSFET detectors. (b) MOSFET placement in the PMMA phantom. Two MOSFET detectors were placed at the midpoint of five clockwise cylindrical cavities - center, 3, 6, 9, 12 o'clock.

A normalization factor (NF) was introduced to establish the absolute dose correlation between the MOSFET measurements and MC simulations following previous work by Jarry et al.[12] MOSFET dose-in-air, $D_{\text{MOSFET air}}$ and MC dose-in-air, $D_{\text{MC air}}$ were divided by each number of projections, i.e., NP_{MOSFET} and NP_{MC} to remove the effect of the different number of projections. With this normalization factor, the absolute dose per projection was calculated from MC simulations using the following equation:

$$\begin{aligned} &D_{\text{MC}} = NF \times D_{\text{MC phantom}} \times \text{total mAs}, \\ &\text{where } NF = \left(D_{\text{MOSFET air}} \Big/ D_{\text{MC air}} \right) \times \left(NP_{\text{MC}} \Big/ NP_{\text{MOSFET}} \right), \\ &\quad D_{\text{MC}} = \text{normalized MC dose to the measurements and} \\ &\quad D_{\text{MC phantom}} = \text{MC dose before the normalization.} \end{aligned} \tag{6}$$

Then, all the absorbed doses per projection were multiplied by the number 660, which represents the average projection number of CBCT in our OBI system.

To obtain the $D_{\text{MOSFET air}}$, dose-in-air exposure measurements were performed for both “half-fan” and “full-fan” modes using a 6 cm^3 ion chamber and a monitor (Model: 9015, Radcal, Monrovia, CA). The ion chamber was placed at the central axis (source to isocenter distance (SID) = 100 cm) and irradiated for 360 degrees in CBCT acquisition mode. The ion chamber was also used to measure the HVL without bowtie filters in the narrow beam geometry (SID = 100 cm). Conversion from exposure (R) to absorbed dose (rad) was performed by multiplying by an f-factor (f_{air} = 0.869) and chamber correction factor. (ccf = 1.001)

Weighted CTDI ($CTDI_w$) for the MOSFET measurements and MC simulations were calculated from the point dose measurements. The $CTDI_w$ can be expressed by the following equation:

$$CTDI_w = \frac{1}{3}CTDI_{center} + \frac{2}{3}CTDI_{peripheries}, \quad (7)$$

where $CTDI_{center}$ = a point dose at a central axis,

$CTDI_{peripheries}$ = an average point dose at peripheries

As aforementioned, the $CTDI_{center}$ and $CTDI_{peripheries}$ of this study were compared with Song et al.[9]'s results to confirm the usability of MOSFET technology for the CBCT dosimetry.

5.2. Monte Carlo simulations

The MC x-ray tube model developed in Section 4 was employed in this study. A tungsten target and other inherent filters were modeled in the BEAMnrc MC system. A 125 keV mono-energetic electron beam was impinged to the target. Detailed schematics can be found in FIG. 1. From the BEAMnrc simulations, a phase space file for each full-bowtie and half-bowtie scan was acquired at SSD = 80 cm. Thus, the distance from the phase space file to the isocenter was 20 cm, enough space to place CT phantoms whose radii were smaller than 16 cm. The number of histories was two billion for both full and half-bowtie simulations; this was enough to achieve the statistical accuracy.

After the BEAMnrc simulation was finished, the phase space file obtained from the BEAMnrc simulation was re-used as an input in order to run DOSXYZnrc user code[31] to calculate the absorbed dose in the phantoms. For the rotational irradiation simulation, we used the source type 8 (phase-space source from multiple directions) with the parameter of 660 projections that were the average number of projections for CBCT image acquisition. Due to the difficulty of building a cylindrical phantom in DOSXYZnrc, the phantoms were CT-scanned by using GE Lightspeed® RT (GE Healthcare, Milwaukee, WI) and CTCREATE user code was used to convert the Hounsfield unit (HU) attenuation values of the phantom CT images into the physical density format, which DOSXYZnrc requires as an input phantom. The converted voxel dimension was $2\times2\times2$ mm^3. DOSXYZ_SHOW user code[35] was employed to find the point dose of each hole for the sake of simplicity. Note that the purpose of this study is to establish and validate the MC model of a clinical OBI, not to implement a MC model for MOSFET detectors. For the HU-to-density conversion, the CT calibration curve of the GE CT machine was used with the reference of default CTCREATE conversion table.[36,37]

5.3. Results

The point doses and $CTDI_w$ of the MOSFET measurements were compared to those of the MC simulations at the four peripheries and in the center for the head and the body phantoms presented in Table I.

TABLE I. Comparison of MOSFET measurements and MC simulations in standard dose and low dose modes.

	Locations	Head phantom			Body phantom		
		MOSFET (cGy)	MC (cGy)	†Differences (%)	MOSFET (cGy)	MC (cGy)	†Differences (%)
Standard dose mode	Center	8.78±0.25	8.77±0.10	0.11	3.09±0.12	3.08±0.05	0.32
	12 o'clock	9.11±0.14	8.81±0.16	3.40	5.64±0.32	5.60±0.08	0.71
	3 o'clock	7.72±0.04	8.76±0.15	11.87	5.45±0.17	5.45±0.06	0.00
	6 o'clock	8.21±0.22	8.74±0.12	6.06	5.20±0.22	5.23±0.06	0.57
	9 o'clock	7.78±0.10	8.74±0.33	10.98	4.99±0.16	5.47±0.08	8.78
	Avg. of peripheries	8.20±0.28	8.76±0.28	6.39	5.32±0.45	5.44±0.14	2.21
	$CTDI_w$	8.39	8.76	4.41	4.58	4.65	1.53
	$CTDI_w$ (Song *et al.*)	8.3	-	-	5.4	-	-
Low dose mode	Center	1.98±0.05	1.97±0.02	0.51	0.72±0.06	0.77±0.01	6.49
	12 o'clock	1.98±0.07	1.97±0.03	0.51	1.39±0.07	1.40±0.02	0.71
	3 o'clock	1.85±0.14	1.96±0.03	5.61	1.34±0.11	1.37±0.02	2.19
	6 o'clock	1.86±0.07	1.96±0.03	5.10	1.26±0.07	1.31±0.02	3.82
	9 o'clock	1.70±0.15	1.96±0.03	13.27	1.22±0.06	1.37±0.02	10.95
	Avg. of peripheries	1.84±0.22	1.96±0.06	6.12	1.30±0.16	1.36±0.04	4.41
	$CTDI_w$	1.89	1.96	3.7	1.11	1.16	4.5
	$CTDI_w$ (Song *et al.*)	1.7	-	-	1.1	-	-

†The difference was calculated by the equation, $(D_{MC} - D_{MOSFET}) / D_{MOSFET} \times 100$.

As shown in Table I, the CTDI were found in the range from 0.72 to 9.11 cGy for both standard and low dose modes. The differences of CTDI between the MOSFET measurements and the MC calculations in standard dose mode were 11.9% for the head phantom, 8.8% for the body phantom and in low dose mode 13.3% for the head phantom, 11.0% for the body phantom.

The $CTDI_w$ acquired from MOSFET measurements ranged from 1.11 to 8.39 cGy and those from MC ranged from 1.16 to 8.76 cGy for both the standard and low dose mode. The differences between the two modalities were within 5%.

The $CTDI_w$ of the MOSFET measurements were also compared with those of Song et al.[9] in Table I. It was found that the differences were 1.1% for the head phantom, 17.9% for the body phantom in standard dose mode and 10.1% for the head phantom, 1.0% for the body phantom in low dose mode.

5.4. Discussion

For the point dose measurements, the data acquired from MOSFET dosimeters was found to be close to the MC simulations within 13.3% for the head phantom and 11.0% for the body phantom. These ranges of differences between MOSFET measurements and MC simulations were what we expected from a previous study.[38] These percentage differences could be explained by three things – energy sensitivity,[39] angular dependency[40] of the MOSFET detector and output fluctuation of the OBI system. First, the variation of the energy spectrum of the photon beam could be one reason. As

the incident poly-energetic photon beam passes through the phantom material from various angles, the energy spectrum of the CBCT beam will be varied significantly due to beam hardening and scattering. Thus, the mean energy of the photon beam will also be changed and this could affect the response of the MOSET detector. For example, if a poly-energetic photon beam generated by 125 kVp with a 14 degree target angle travels 1 cm PMMA, the mean energy in the air could be increased by 29.8%.[23] This increase would lead to a change in the rate of photoelectric absorption in the detector and alter its response. Second, as is well-known, a MOSFET detector has the physical characteristic of angular dependency. That is, the absorbed dose of the MOSFET detector is highly dependent upon the orientation of the beam. It has been observed that angular dependency of a MOSFET detector disappears in a tissue-equivalent medium[40] for an x-ray beam of 70 kVp and 250 mAs. However, the measurements of previous work[40] performed under the condition of a uniform scattering environment – rotating the dosimeter at the center of the phantom with lower kVp – represents a different situation from that in this study. In addition, the treatment couch used in this study could reproduce non-uniform scatter distribution to the phantom. In sum, further investigation would be needed to characterize the MOSFET detector's responses to various x-ray energies and non-uniform irradiation conditions. Third, it has been observed that the output of our OBI system fluctuates slightly for each CBCT image acquisition with a variation in the number of projections. This also could affect the accuracy of the CBCT dosimetry.

Note that the standard deviations of the MOSFET measurements are not comparable to those of the MC results. The standard deviations of the MOSFET represent the experimental deviations, while those of the MC are statistical uncertainties of particle histories.

Comparing the $CTDI_w$ data of this study to those of Song et al.,[9] it was found that the MOSFET measurements were consistent with their data within 10%. It should be mentioned that the phantom sizes Song et al. used were slightly different from the CT phantoms used in this study. 18 cm diameter head phantom (16 cm diameter in this study) and 30 cm diameter body phantom (32 cm diameter in this study) were employed in Song et al.'s study. The reason, the $CTDI_w$ of Song et al. was slightly smaller than that of this study for the head phantom, can be explained by the larger size of their phantom (2 cm larger in diameter). The larger size would cause higher beam attenuation due to the longer path length of the beam and these beams would deposit fewer radiation doses not only to the center but also to the peripheries; e.g. the dose from the 12 o'clock beam would give almost the same amount of radiation dose to the detector located at 12 o'clock. However, it would give smaller doses to the detector at 6 o'clock because it would become softer when it reaches the detector. The same explanation can be applied to the body phantom scan. The slightly smaller size of their body phantom could be responsible for the increase in the $CTDI_w$ of this study. Consequently, the same size effect was also observed for both standard and low dose modes.

A limitation of this study is the couch effect, which was not included in the MC simulations because the information of couch geometry and material data was unable to be obtained by the manufacturer. It was recognized that $CTDI_w$ is an interim dose index for CBCT geometry. Much research is being performed to develop a new CBCT dose index. This research represents a preliminary study to estimate the absorbed doses in a clinical CBCT system. The ultimate goal of this study is to establish an anthropomorphic phantom dosimetry using the MC model for estimation of organ doses and an effective dose.

5.5. Conclusion

CTDI for CBCT were measured by using MOSFET detectors and simulated with MC in head and body CT phantoms. The results showed that the maximum differences between the MOSFET measurements and the MC calculations were within 14%; this is acceptable for MC simulations in low energy photon dosimetry. For the $CTDI_w$, the discrepancies were within 5%. It was also found that our data is comparable to the previously published study.[9]

6. CONE BEAM CTDI SIMULATIONS/MEASUREMENTS WITH IMAGE QUALITY ANALYSIS (New Protocol)

In August 2008, Varian Medical Systems updated the cone beam CT scan protocols of the OBI system in order to minimize the CBCT dose to the patient, while maintaining similar CBCT image qualities. They released six new CBCT scan protocols based on the scan locations and image qualities. With all the reductions of the peak x-ray tube voltage (kVp), tube current (mA), and number of projections with rotation angles, the CBCT imaging dose has largely been decreased. In this study, the $CTDI_w$ for the new scan protocols of the OBI system were assessed with ion chamber measurements and MC simulations and compared to those of old scan protocols. In addition, the image quality parameters were assessed for the new protocols using the CBCT image quality assurance (QA) protocol.[34] Five parameters were tested: Hounsfield Unit (HU) linearity, spatial linearity, spatial resolution, contrast resolution, and HU uniformity.

6.1. Point dose measurements

The point doses were measured in head and body cylindrical PMMA phantoms using a 0.18 cm^3 ion chamber (Model: 10x5-0.18, Radcal Corporation, Monrovia, CA). For each CBCT scan, the ion chamber was sequentially placed at the midpoint of the cylindrical cavities located in the center and four peripheral positions (FIG. 8 (a) for head scan and FIG. 8 (b) for body scan). Different cavity positions were labeled as 3, 6, 9, 12 o'clock and center position. Thus, five CBCT scans produced one set of scan data. A total

of six new CBCT scan protocols were employed: (1) standard-dose head, (2) low-dose head, (3) high-quality head, (4) pelvis, (5) pelvis spotlight, and (6) low-dose thorax. The scan parameters for each scan protocol are presented in Table II. Note that all the head protocols (standard-dose, low-dose, and high-quality) and pelvis spotlight protocol use the "partial-angle scan" technique while the pelvis and low dose thorax protocols use the "full angle scan" technique. For each scan mode, several sets of scans were performed to check the systematic stability of the ion chamber measurements. The f-factor in the air (0.873) was used to convert the measured exposures to the absorbed doses.[41] These point doses were considered as CTDI assuming that the dose equilibrium was achieved. The $CTDI_w$ for each protocol was computed and compared with those of old scan protocols for the dosimetric evaluation.

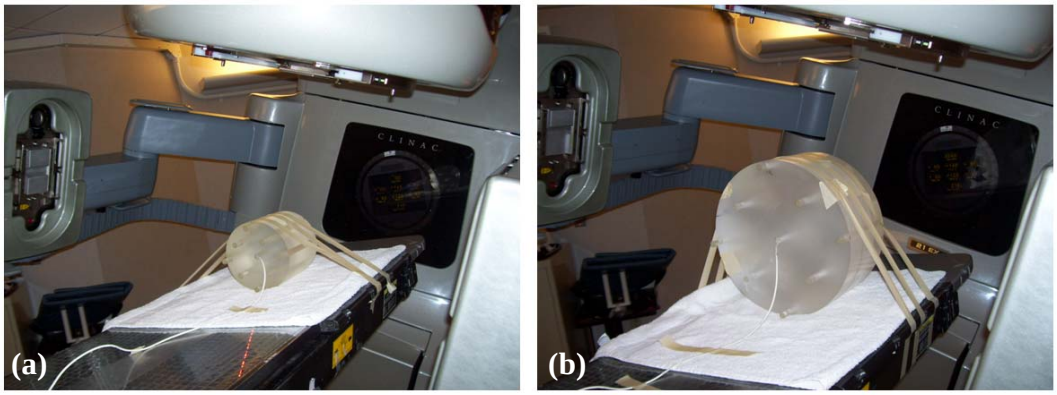

FIG. 8. Experimental setups for new CBCT scan protocols. (a) standard-dose head, low-dose head, and high-quality head, (b) pelvis, pelvis spotlight, and low-dose thorax scans.

Table II. Detailed scan parameters and $CTDI_w$ values for new CBCT scan protocols.

	Standard-Dose Head	Low-Dose Head	High-Quality Head	Pelvis	Pelvis Spotlight	Low-Dose Thorax
Peak Voltage (kVp)	100	100	100	125	125	110
Tube Current (mA)	20	10	80	80	80	20
Exposure time (msec)	20	20	25	13	25	20
Rotation Range (deg)	200	200	200	360	200	360
Number of projections	377	376	377	679	376	677
Exposure (mAs)	150.8	75.2	754	706.2	752	270.8
Fan type	Full fan	Full fan	Full fan	Half fan	Full fan	Half fan
Default Pixel Matrix	384 x 384	384 x 384	384 x 384	384 x 384	384 x 384	384 x 384
Slice Thickness (mm)	2.5	2.5	2.5	2.5	2.5	2.5

6.2. Monte Carlo Simulations

The CTDI values of the new CBCT scan protocols were calculated by using the BEAMnrc/EGSnrc MC system. CBCT beam outputs were characterized by the peak tube voltages and filtrations in the MC simulations; all six scan protocols were categorized into four CBCT beam output modes: 100 kVp full-bowtie, 125 kVp full and half-bowtie, and 110 kVp half-bowtie. These four CBCT modes were simulated in the BEAMnrc system. Thus, a total of four corresponding phase space files were acquired from the BEAMnrc simulations. As dose is linearly proportional to tube-current-time product (mAs), all the MC results were normalized by mAs. It may be noted that the pelvis mode scan parameters in the new protocol were the same as those of the old protocol, with the exception of the tube-current-time-product. Thus, the phase space file of the old scan protocol was re-used for the pelvis scan simulation of the new protocol. The MC parameters for particle transports were the same as in Section, 4.2.

After these three CBCT beam data were acquired from BEAMnrc simulations, the CBCT photon beams were transported into the CT phantoms in DOSXYZnrc simulations with different irradiation patterns as described in Table II. The number of histories was set to 30 billion to obtain smooth dose distributions. The CTDI values at the center and peripheral locations were extracted from the DOSXYZnrc results and averaged the same as in the physical experiments. In order to compare the MC doses to the measurements, the MC doses were normalized by using the 6 o'clock dose measurements. The 6 o'clock

dose value was chosen because it was more stable – higher exposure produces less statistical uncertainty due to larger ionizations in the detector.

6.3. CTDI estimations with various methods

Leitz et al.[42] proposed a method to estimate the average CTDI values for a single slice CT scan in CT phantoms. Assuming two premises: (1) dose outside the nominal slice thickness is zero, and (2) a linear dose decrease between the peripheral and center positions; they derived the average dose equation by integrating the CTDI in the phantoms. This concept is equivalent to the current weighted CTDI ($CTDI_w$), which is well known as follows:

$$\begin{aligned} &CTDI_w = W_{center} CTDI_{center} + W_{peripheries} CTDI_{peripheries}, \\ &\text{where } W_{center} = \text{ weighting factor for } CTDI_{center}, \\ &\qquad W_{peripheries} = \text{ weighting factor for } CTDI_{peripheries}, \\ &\qquad CTDI_{center} = \text{a point dose at a central axis, and} \\ &\qquad CTDI_{peripheries} = \text{an average point dose at peripheries} \end{aligned} \tag{8}$$

They found that the $CTDI_w$ equation with W_{center}=1/3 and $W_{peripheries}$=2/3 produces the average dose in the phantom for which the above equation becomes same as the equation (7).

Recently, Bakalyar[43] investigated the accuracy of the numerical coefficients in this $CTDI_w$ method. On the basis of six premises: (1) a homogeneous cylinder phantom,

(2) full lateral coverage of the CT beam to the phantom, (3) smooth variation of the CT beam density, (4) uniform 360 degree irradiation, (5) monotonic dose delivery rate, and (6) smooth change of the bowtie filter thickness, he found that the numerical coefficients, W_{center}=1/3 and $W_{peripheries}$=2/3 are not best fits because the discontinuity of the dose gradient at the center position is not physically real in the CT dosimetry. From the second order (parabolic) Taylor expansion, he found the numerical coefficients, W_{center}=1/2 and $W_{peripheries}$=1/2 produce a more accurate fit in averaging the volumetric CT doses.

In this study, four calculation methods were used to estimate the CTDI values: (1) conventional $CTDI_w$ calculation (W_{center}=1/3 and $W_{peripheries}$=2/3), (2) Bakalyar's method (CTDIwb: W_{center}=1/2 and $W_{peripheries}$=1/2), (3) averaging the absorbed doses within a center slice ($CTDI_{2D}$), and (4) averaging the absorbed doses through entire phantom slices ($CTDI_{3D}$). Note that methods (3) and (4) numerically average the dose distribution in a slice and a volume, respectively, without using $CTDI_w$ equations. Methods (1) and (2) were applied to the ion chamber data, and all four methods were applied to the MC data. To perform methods (3) and (4), 3D dose distribution data from MC simulations were imported into the MATLAB system (Mathworks, Natick, MA) and analyzed to calculate the average slice and volume doses. All the results were cross-compared to each other. In the analysis, we assume that the $CTDI_w$ of the method (4) is the most accurate $CTDI_w$ estimate because it is the numerically averaged value directly calculated from the 3D dose distribution in the phantoms; that is, there are no assumptions employed in method (4), such as the fitting and dose equilibrium used in methods (1) and (2). Note

that the results of method (3) are not expected as accurate as those of method (4) because the dose also decreases along the longitudinal direction.

6.4. Image quality analysis

The CBCT image quality QA protocol was performed to evaluate the image quality of the new protocols following the work of Yoo et al.[34] At the present time, no standard CBCT image quality QA protocol exists. The Catphan 504 phantom (The Phantom Laboratory, Salem, NY) was employed for all the image quality tests. The Catphan 504 phantom consists of four different modules; each module serves its own purpose in the QA test. The CT images of each module are shown in FIG. 9(a) to 9(e). The phantom was hung at the end of the couch with the aid of its wooden case as a counter balance and was aligned to the treatment isocenter. Six CBCT scan protocols were evaluated and each image was assessed for the five QA criteria – HU linearity, spatial linearity, spatial resolution, contrast resolution, and HU uniformity. All the image tests were performed in an Eclipse treatment planning workstation (Varian Medical Systems, Palo Alto, CA).

a. HU verification. The CTP 404 module contains seven materials that have different densities. The materials and corresponding HU values can be referred to as those from the manual of the phantom. A region of interest (ROI) was selected in the designated material section using the "Area profile" tool to measure the mean HU values.

The ROI size was about 0.7×0.7 cm^2 and the acceptance criteria was ±40 HU. (See FIG. 9(a))

b. Spatial linearity. There are four rods of 3 mm diameter forming a 5 cm square in the CTP 404 module. The distance between two adjacent rods was calculated using the "Distance" tool in the Eclipse system. The tolerance range was ±0.5 cm. (See FIG. 9(b))

c. Spatial resolution. The CTP 528 module contains a 21 line pair/cm high resolution test gauge; the least discernable bar group was determined in the test. The acceptance tolerance was 6 lp/cm.(See FIG. 9(c))

d. Contrast resolution. The CTP 515 module contains three groups of nine supra-slice disks with diameters of 2-15 mm and subject contrasts of 0.3%, 0.5%, and 1.0%. The image was visually inspected to determine the lowest contrast disk visible. The recommended tolerance was 1% fourth disk. (See FIG. 9(d))

e. HU uniformity. The CTP 486 module consists of a single uniform disk of 20 cm diameter. Mean HU was measured for five selected ROI regions – center, top, left, right, and bottom. The size of ROI was about 1.0×1.0 cm^2 and the acceptance criterion was ±40 HU. (See FIG. 9(e))

6.5. Results

Table III presents the CTDI values obtained from IC measurements and MC simulations and CTDI differences between each calculation method. All the CTDI values ($CTDI_w$, $CTDI_{wb}$, $CTDI_{2D}$, and $CTDI_{3D}$) of the new CBCT protocols ranged from 3 to 29 mGy for

both IC measurements and MC simulations, while those of the old protocols ranged from 39 to 85 mGy. The CTDI of the new protocols were found to be lower by about a factor of 14 for a standard dose head scan mode and 1.8 times for standard body scan mode (pelvis) than the old head and body protocols, respectively. Note that the $CTDI_w$ per 100 mAs calculated from method (1) are similar across the same kVp and filtration to 7%.

As can be seen in Table II, the differences between IC measurements and MC simulations were <2% for method (1) and <3% for method (2). The differences between methods (1) conventional $CTDI_w$ method and (2) Bakalyar's $CTDI_w$ method were less than 2% for the head scans, while they were about 8~12% for the body scans. The differences between point dose method of IC measurements ($CTDI_w$ and $CTDI_{wb}$) and the central slice averaging method ($CTDI_{2D}$) were found as <4% for head scans while <6% for body scans. Large differences (9-21 %) were found between the results of method (1) conventional $CTDI_w$ method, (2) Bakalyar's $CTDI_w$ method, (3) central slice averaging method and that of method (4) entire volume averaging method.

Two-dimensional (2D) dose distributions of each CBCT scan protocol were visualized in the MATLAB system as shown in FIG. 10. The differences of dose distributions are noted between partial-angle and full-angle CBCT scan protocols, i.e., the partial-angle CBCT scan protocols show a larger dose along the scanning angles than in the non-irradiation angles, while full angle CBCT scan protocols produce uniform angular dose distribution. The phantom size effect in the dose distribution of the short scan can be also noticed between the head and body protocols;

TABLE III. CTDI values and comparisons between the CTDI values acquired from method (1) to method (4). The CTDI differences were calculated by following equation: $(CTDI_{\text{front}} - CTDI_{\text{rear}})/CTDI_{\text{rear}} \times 100$. Note that the abbreviations IC and MC represent ion chamber measurements and Monte Carlo simulations.

CTDI values		New scan protocols						Old scan protocols	
		Standard-dose head	Low-dose head	High-quality head	Pelvis	Pelvis spotlight	Low-dose thorax	Standard head	Standard body
$CTDI_w$	IC (mGy/100mAs)	4.00	4.24	3.84	3.60	3.16	2.83	6.27	3.41
	IC (mGy)	6.03	3.19	28.96	25.44	23.78	7.68	83.97	45.75
	MC (mGy)	5.99	3.16	28.78	25.09	23.53	7.58	83.50	45.22
$CTDI_{wb}$	IC (mGy)	6.08	3.24	29.27	23.44	21.97	6.99	84.94	42.03
	MC (mGy)	6.01	3.17	28.85	22.66	21.40	6.77	83.87	40.84
$CTDI_{2D}$	MC (mGy)	5.93	3.13	28.48	24.34	22.40	7.30	83.65	43.88
$CTDI_{3D}$	MC (mGy)	5.36	2.83	25.74	21.52	19.72	6.43	75.68	38.80
Comparison between each CTDI value									
$CTDI_w$ (IC vs MC, %)		+0.67	+0.95	+0.63	+1.39	+1.06	+1.32	+0.56	+1.17
$CTDI_{wb}$ (IC vs MC, %)		+1.16	2.21	+1.46	+3.44	+2.66	+3.25	+1.28	+2.91
$CTDI_w$ vs $CTDI_{wb}$ (IC, %)		-0.82	-1.54	-1.06	+8.53	+8.24	+9.87	-1.14	+8.85
$CTDI_w$ vs $CTDI_{wb}$ (MC, %)		-0.33	-0.32	-0.24	+10.72	+9.95	+11.96	-0.44	+10.72
$CTDI_w$ vs $CTDI_{2D}$ (IC, %)		+1.69	+1.92	+1.69	+4.52	+6.16	+5.21	+0.38	+4.26
$CTDI_{wb}$ vs $CTDI_{2D}$ (IC, %)		+2.53	+3.51	+2.77	-3.70	-1.92	-4.25	+1.54	-4.22
$CTDI_w$ vs $CTDI_{3D}$ (IC, %)		+12.50	+12.72	+12.51	+18.22	+20.59	+19.44	+10.95	+17.91
$CTDI_{wb}$ vs $CTDI_{3D}$ (IC, %)		+13.43	+14.49	+13.71	+8.92	+11.41	+8.71	+12.24	+8.32
$CTDI_{2D}$ vs $CTDI_{3D}$ (%)		+10.63	+10.60	+10.64	+13.10	+13.59	+13.53	+10.53	+13.09

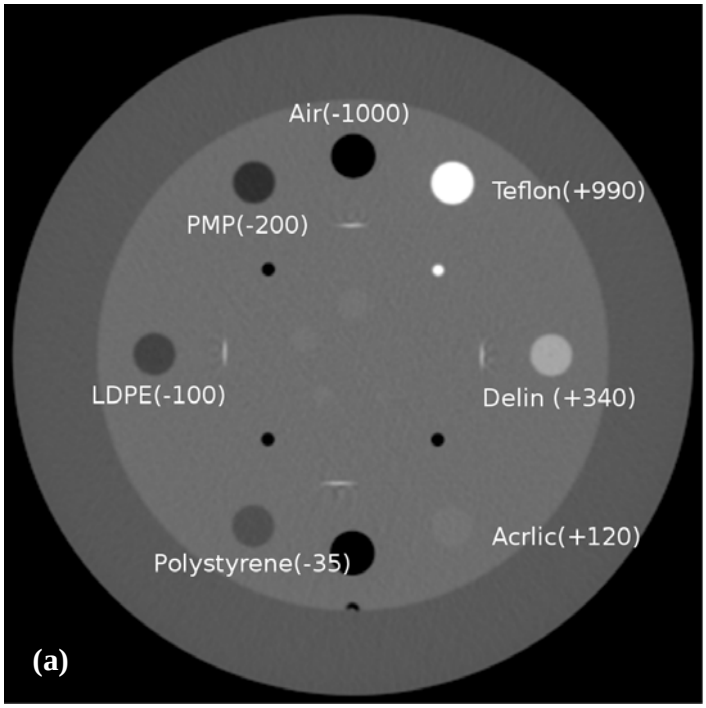
Air(-1000)
Teflon(+990)
PMP(-200)
LDPE(-100)
Delin (+340)
Acrlic(+120)
Polystyrene(-35)
(a)

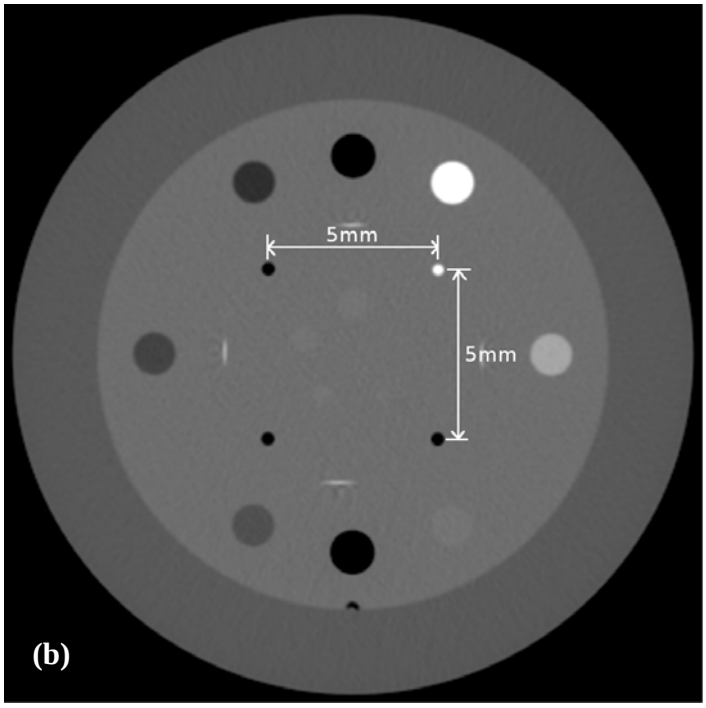
5mm
5mm
(b)

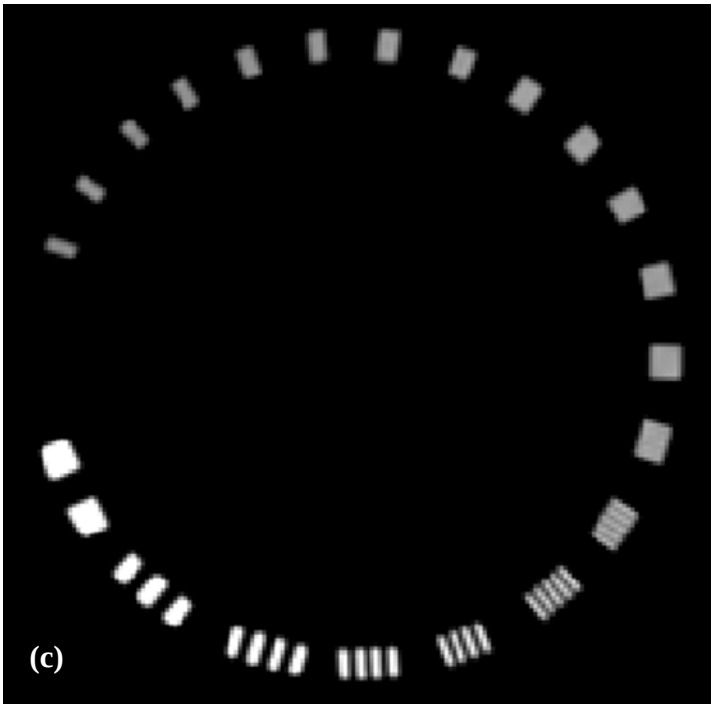
(c)

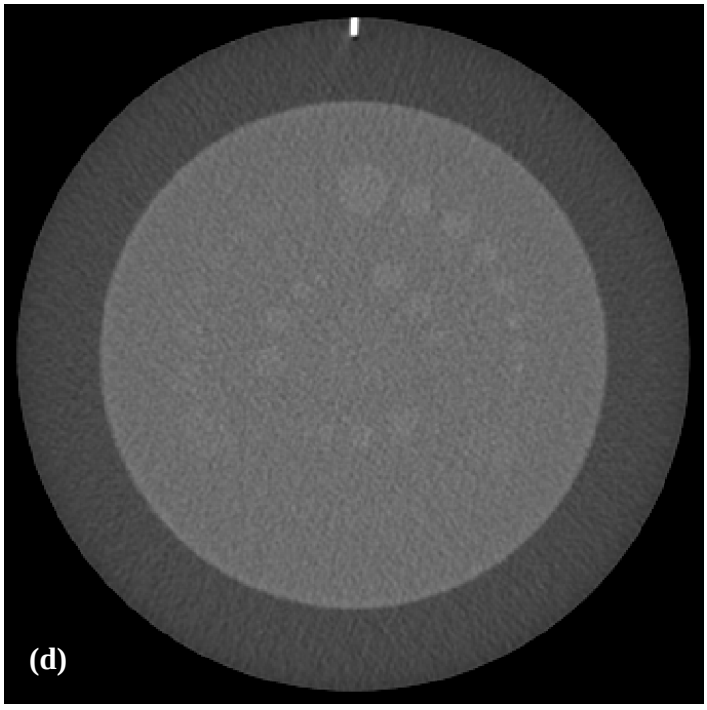
(d)

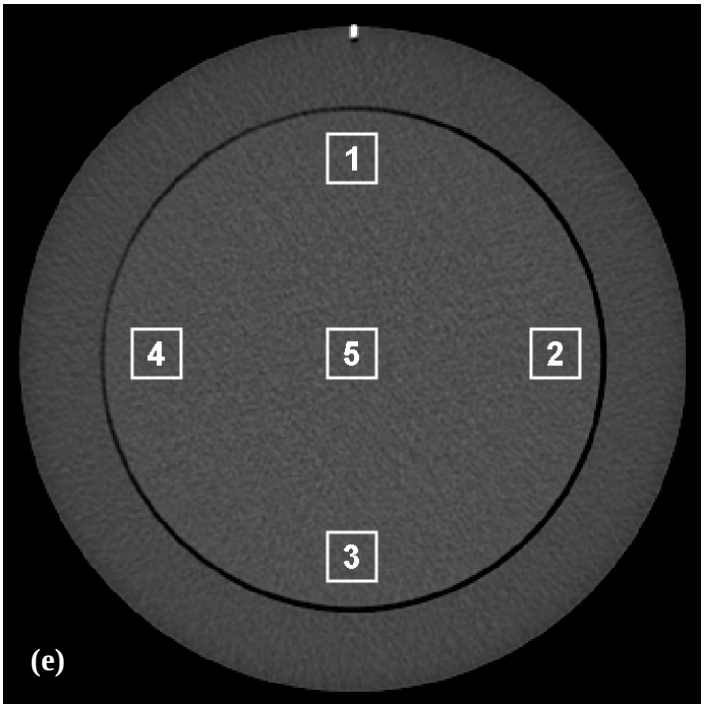

FIG. 9. CT images of the CATPHAN 504 phantom for the image quality tests of (a) HU verification (module: CTP 404), (b) spatial linearity (CTP 404), (c) spatial resolution (CTP 528), (d) contrast resolution (CTP 515), and (e) HU uniformity (CTP 486).

the pelvis spotlight protocol delivers more crescent-shaped dose distributions (FIG. 10(c)), while head protocols show more half-moon dose distributions (FIG. 10(a)).

Table IV shows the results of image quality QA tests for new and old scan protocols. In the HU verification test, all the protocols were within the tolerance (±40 HU) except low dose head and low dose thorax scan protocols; low-dose head failed in Teflon and Delin and low-dose thorax failed every material except air. As can be seen in FIG. 11, the measured HU values of the low-dose head scan start to deviate at the

nominal value of ~340 HU and the deviation becomes more significant in the higher HU region.

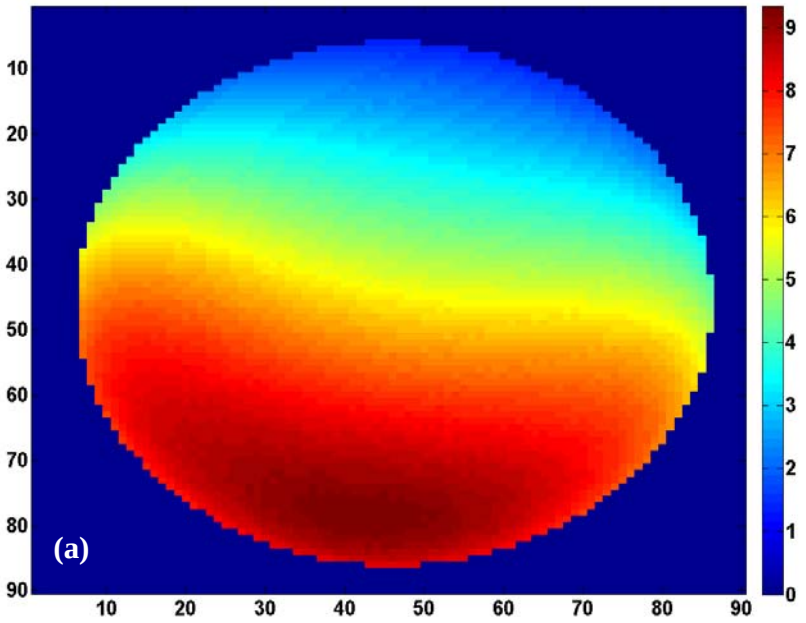

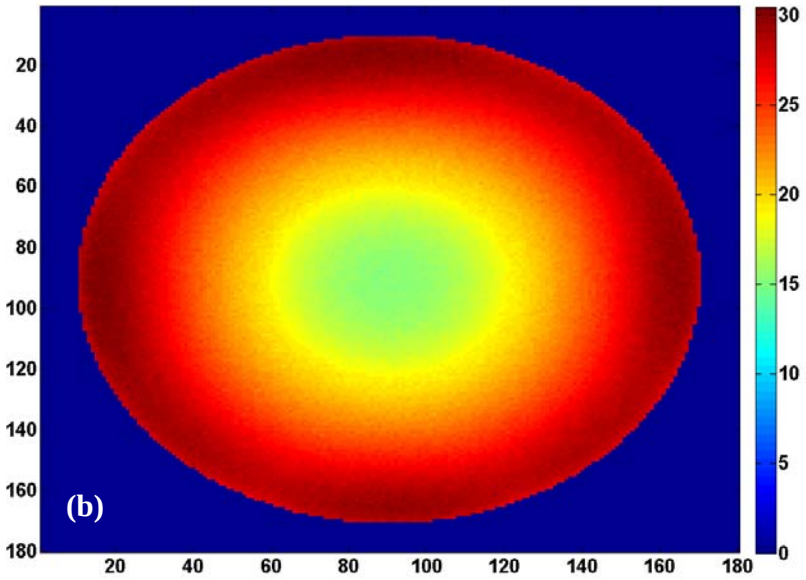

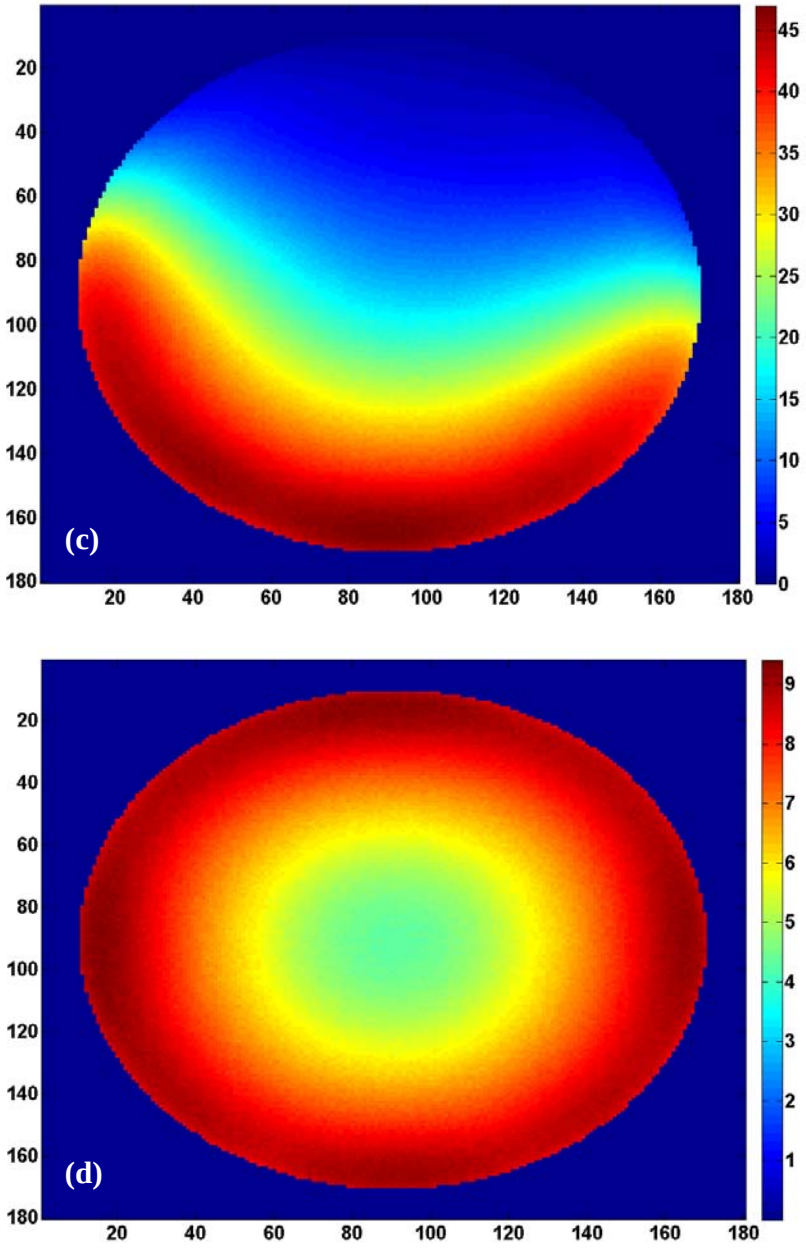

FIG. 10. Visualization of the 2D dose distribution for each new CBCT scan protocol: (a) head, (b) pelvis, (c) pelvis spotlight, and (d) low-dose thorax scans.

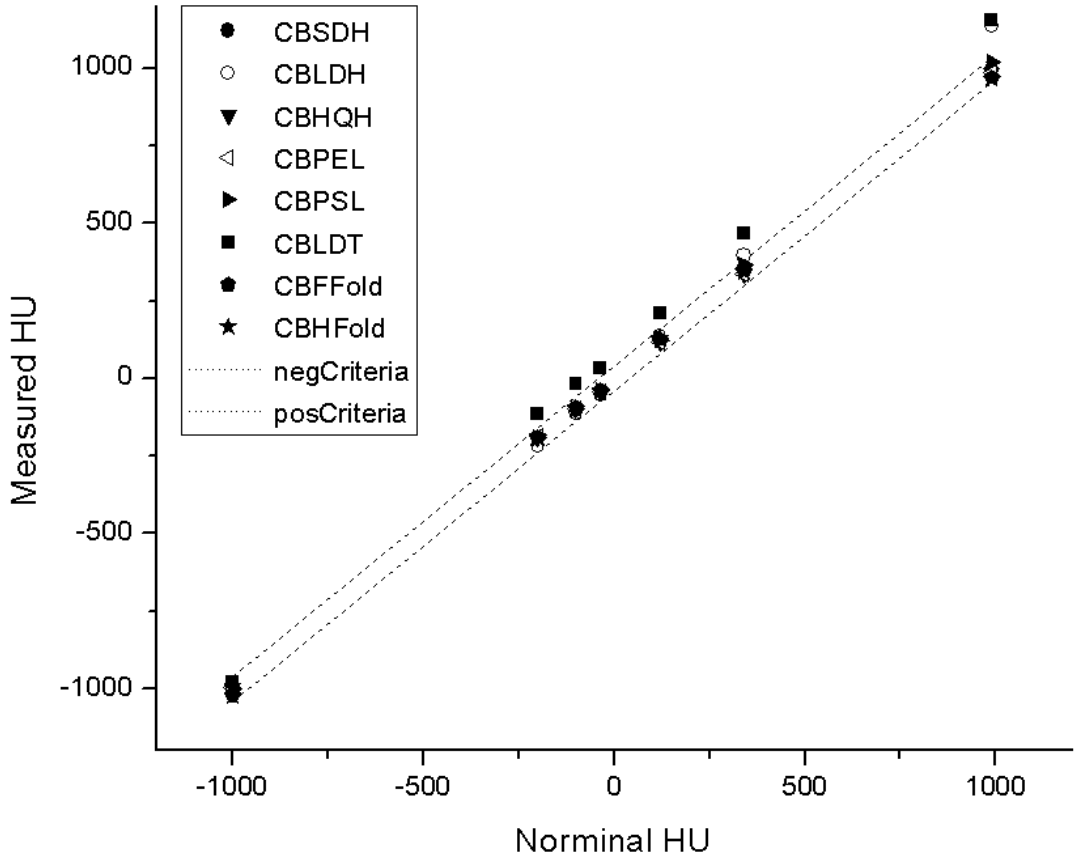

FIG. 11. HU linearity test for the new CBCT protocols. Legends are as follows; CBSDH: standard dose head, CBLDH: low dose head, CBHQH: high quality head, CBPEL: pelvis, CBPSL: pelvis spotlight, CBLDT: low dose thorax, CBFFold: old full-fan, and CBHFold: old half-fan.

The low-dose thorax protocol shows the same pattern; the HU values increase at the nominal HU of -1000 and the deviation becomes larger as the HU increases. All the tests of the spatial linearity, spatial resolution, and HU uniformity met the manufacturer's suggested tolerances. In the contrast resolution test, only high-quality head and pelvis

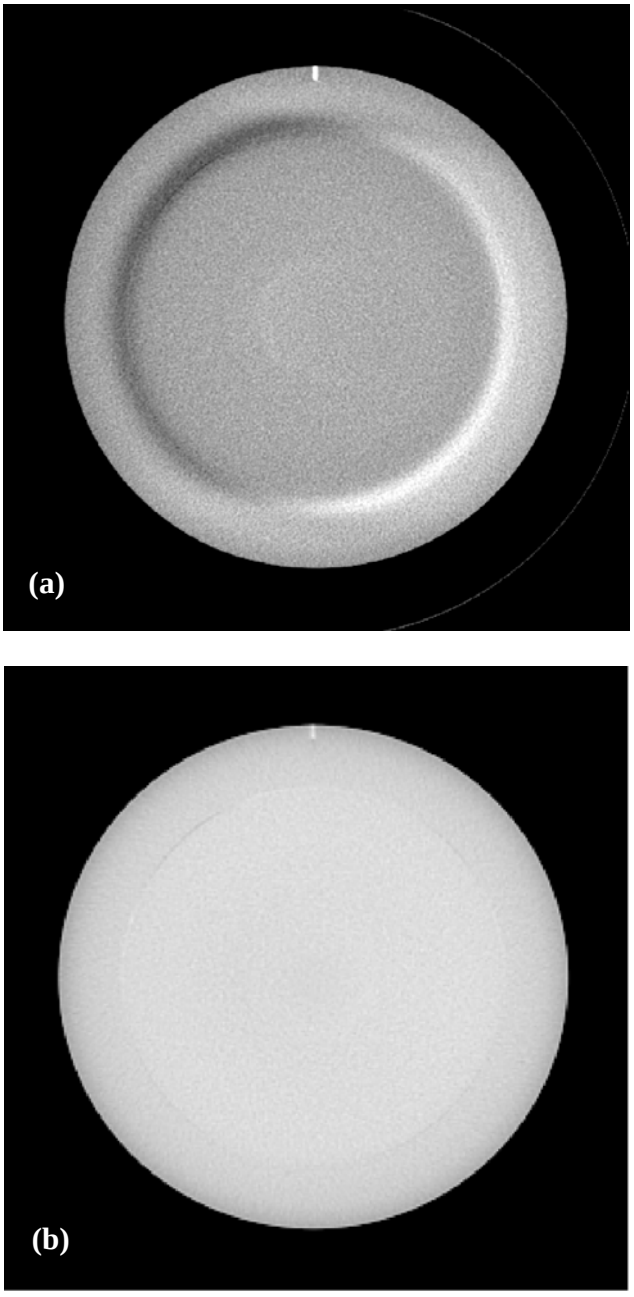

FIG. 12. CBCT images for the HU uniformity test obtained from (a) CBHQH (partial-angle scan) and (b) CBPEL (full-angle scan) protocols. Note the crescent effect at the interface of the two different density materials.

Table IV. Results of image quality QA tests for new and old CBCT scan protocols. Note that all the QA data of the old protocols are referenced from Ref. 34. The HU differences were calculated by the following equation: $(HU_{\text{measured}} - HU_{\text{nominal}})$. Note that the abbreviation n.HU represents nominal HU.

	QA parameters		New scan protocols						Old scan protocols	
			Standard-dose head	Low-dose head	High-quality head	Pelvis	Pelvis spotlight	Low-dose thorax	Standard head	Standard body
	Material	n.HU	Image quality analysis							
HU verification	Air	-1000	-991±13.8	-998±3.8	-996±5.7	-994±16.0	-999±2.2	-980±22.9	-1022±1.8	-1023±1.9
	Teflon	990	996±37.9	1135±41.8	1001±17	985±20.3	1019±16.4	1155±19.1	970±7.3	964±20.4
	Delin	340	352±43.4	395±48.2	344±17.2	336±10.7	365±17.0	465±12.7	349±13.4	343±18.0
	Acrylic	120	123±33.6	133±35.8	121±16.6	116±10.6	123±14.3	211±12.8	128±5.8	128±13.9
	Polystylene	-35	-45±38.9	-51±39.3	-41±14.8	-43±11.0	-39±13.1	35±13.3	-39±5.2	-44±13.8
	LDPE	-100	-99±32.9	-110±40.6	-100±13.8	-98±8.4	-99±12.4	-19±13.4	-94±3.6	-99±11.0
	PMP	-200	-192±34.9	-215±30.4	-193±14.3	-187±10.3	-192±11.5	-115±13.1	-189±8.2	-193±10.4
HU difference	Air	Unit : %, Tolerance: ±40 HU	+9	+2	+4	+6	+1	+20	-22	-23
	Teflon		+6	+145	+11	-5	+29	+165	-20	-26
	Delin		+12	+55	+4	-4	+25	+125	+9	3
	Acrylic		+3	+13	+1	-4	+3	+91	+8	8
	Polystylene		-10	-16	-6	-8	-4	+70	-4	-9
	LDPE		+1	-10	0	+2	+1	+81	+6	+1
	PMP		+8	-15	+7	+13	+8	+85	+11	+7
Spatial linearity (cm)			4.99±0.01	4.99±0.02	4.99±0.02	5.00±0.01	5.01±0.01	4.98±0.02	4.97~5.01	4.97~5.01
Spatial resolution (group)			8	8	9	6	8	6	8	6
Contrast resolution (disk)			0	0	4	5	3	1	5	4
HU uniformity	ROI #1 (HU)		12±32.6	14±31.4	12±15.2	-9±7.5	13±12.2	74±8.5	12±8.3	14±48.1
	ROI #2 (HU)		-6±32.1	-12±34.1	-6±13.6	2±8.7	-6±12.2	82±11.8	-2±4.5	-15±20.9
	ROI #3 (HU)		-3±32.4	-9±36.0	-4±14.4	4±8.7	0±10.8	80±11.8	-1±3.8	-19±20.0
	ROI #4 (HU)		-12±33.1	-19±31.7	-11±15.4	-4±7.8	-11±12.3	80±11.9	-3±5.1	-20±18.4
	ROI #5 (HU)		-4±34.6	-9±34.3	-1±15.2	-1±9.1	-1±12.4	80±12.7	-7±5.1	-20±12.7
	Mean		-2.6	-7	-2	-1.6	-1	79.2	-0.2	-12
	Standard deviation		8.9	12.4	8.6	5.1	9.0	3.0	7.2	14.7

scan protocols were within the acceptance level (disk 4 in supra-slice 1.0% group). In addition, a crescent effect was especially found at the interface of two different materials in the partial-angle scan protocols shown in FIG. 12(a).

6.6. Discussion

Since the introduction of the kV CBCT imaging technique to radiation oncology, significant efforts[6-9] have been made to accurately quantify the CBCT imaging dose in order to minimize it. Theoretically, one can perfectly reconstruct a 3D image of a fan-beam CT scan with a partial-angle scan, which acquires the projections of 180 degree plus fan angle. With the similar fan geometry, this concept may also be applicable to the CBCT scan. The partial-angle CBCT scan protocols have been employed in the new OBI system (V1.4) in order to achieve a lower dose while maintaining similar CBCT image quality.

To the best of our knowledge, this study presents the first dosimetric data for the partial-angle CBCT scan protocols where the dose distribution is angularly inhomogeneous. In addition, no suitable technology exists to accurately measure the whole non-uniform 3D dose distribution for the kV energy range at the present time. Radiochromic film or a large number of thermoluminescent dosimeters (TLD) may be used to acquire the 2D dose distribution; however, the latter, in particular, would be highly labor intensive and time consuming. To overcome these limitations the MC method was employed.

In this study, the CTDI was estimated for both partial and full-angle CBCT scan protocols by using the point dose method and numerical averaging methods. MC simulations were also performed to benchmark the accuracy of CTDI of the point dose measurements. As shown in Table III, MC simulations were validated by the comparison of $CTDI_w$ and $CTDI_{wb}$ values. As expected, the CTDI values of the head protocols were linearly proportional to the tube-current-time-product (mAs); the standard-dose head protocol produced twice as high doses as the low-dose head protocol and five times lower doses than the high-quality head protocol did. In the body protocols, the pelvis protocol produced higher doses than the pelvis spotlight protocol did in spite of its lower mAs. This is caused by the fan-type differences directly related to the shape of the bowtie filters as well as the irradiation pattern; a full-bowtie has ~2.8 cm thick aluminum filter in both left and right off-axial locations, while a half-bowtie has the thick part of the filter only in the right off-axis location (See FIG. 1). The irradiation patterns between full-fan and half-fan modes are also different as described in Section 6.1. These differences between full-fan and half-fan modes cause different attenuations of the off-axial beam, which consequently brought the non-linearity in CTDI. Note that CTDI values of the pelvis protocol (new) are proportionally smaller than those of the standard body protocol (old) with smaller mAs.

The differences between the conventional CTDI method ($CTDI_w$) and Bakalyar's CTDI method ($CTDI_{wb}$) for head scans were relatively smaller than those for body scan. To analyze this effect, lateral profiles were acquired from the 3D dose data of head and

body scans (old protocols) at center, middle and edge locations in the CT phantoms. As can be seen in FIG. 13(a) and FIG. 13(b), the profiles from the head scan are relatively linear, while those from the body scan are in parabolic shapes. In a linear curve such as the head profile, there will be no large differences between linear and parabolic fittings while large differences could be expected in a parabolic curve (body profile) because a linear fitting is inappropriate for parabolic functions.

The CTDI differences between the Bakalyar's CTDI method ($CTDI_{wb}$) and the central slice averaging method ($CTDI_{2D}$) were found as smaller than those between the conventional CTDI method ($CTDI_{w}$) and the central slice averaging method ($CTDI_{2D}$) for the body scans (See Table III), whereas the opposite results were found for the head scans. This can be explained by the previously described fitting effect for different size phantoms. The lateral profile of the head scan is relatively flat (linear), while that of the body scan shows a parabolic shape for the center profiles (See FIG. 13(b)); thus, one can expect that the linear fitting (fit method A) will produce smaller differences for the head scans, while the parabolic fitting (fit method B) will produce smaller errors for the body scan. To validate this observation, we performed linear and parabolic fittings to the lateral profiles of the center slice for both head and body scans using a MATLAB function, POLYFIT. Then, we estimated the dose profile integral (DPI) using true values and fitted curves to evaluate the deviations of the DPI values. In the results, the DPI deviation of the linear fit was 11.1% and that of the parabolic fit was 11.4% for the head scan. The deviation of the linear fit was 24.7% and that of parabolic fit was 16.3% for

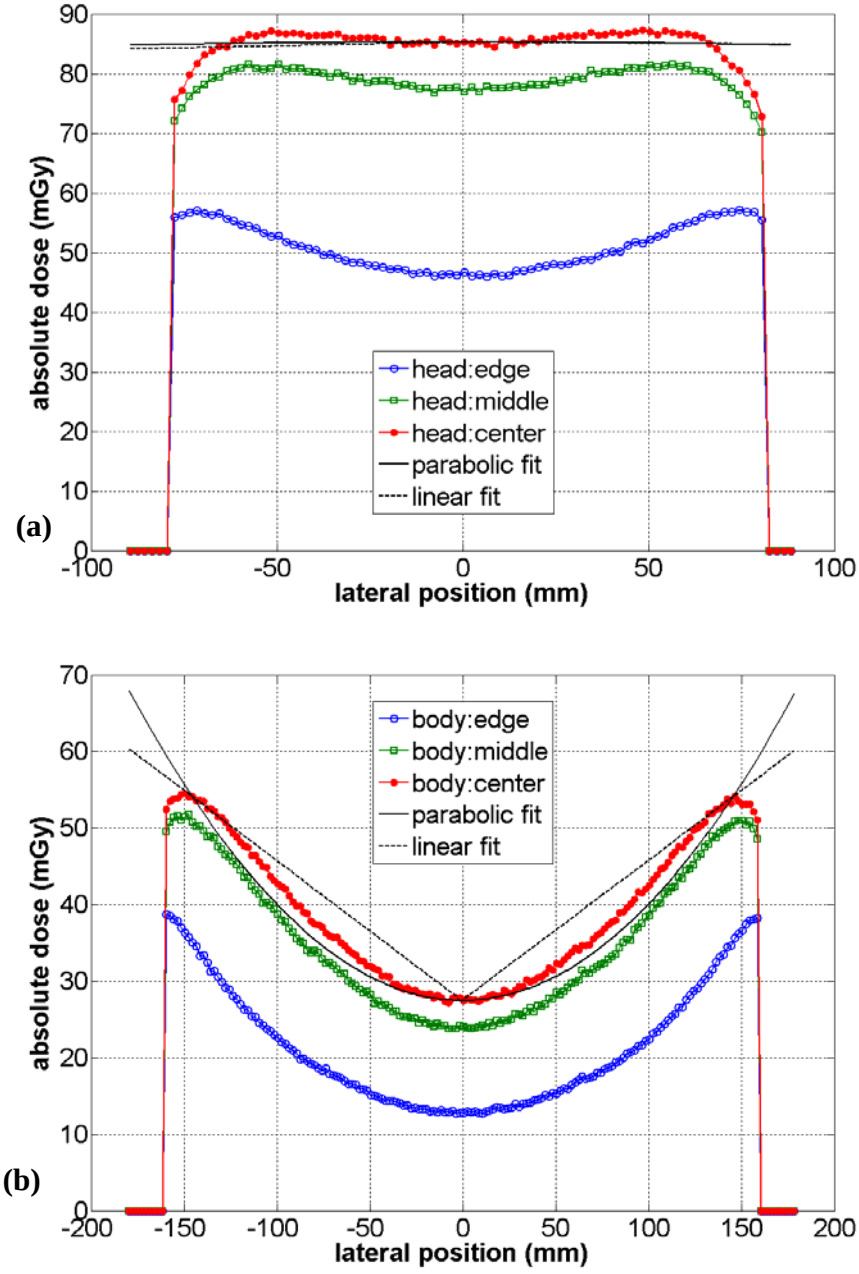

FIG. 13. (a) Cross-sectional profiles obtained from standard head scan and (b) from standard body scan. Solid circle, open square and open circle denote the profiles acquired at center, middle and edge locations in the CT phantoms.

the body scan. Thus, we verified that linear and parabolic fits do not produce significant differences for the head scan, whereas the parabolic fitting produces more accurate dose estimations than the linear fitting for the body scan.

Although the central slice averaging method ($CTDI_{2D}$) was expected to yield a better dose estimation to the entire volume averaging method ($CTDI_{3D}$) than the Bakalyar's CTDI method ($CTDI_{wb}$) does, opposite results were found in the body scan data; the differences between $CTDI_{2D}$ vs $CTDI_{3D}$ were larger than those between $CTDI_{wb}$ of IC vs $CTDI_{3D}$ (or $CTDI_{wb}$ of MC vs $CTDI_{3D}$) for the body scan, while those between $CTDI_{2D}$ vs $CTDI_{3D}$ were smaller for the head scan. This can also be explained with the fitting effect; as can be seen in FIG.13(b), the parabolic fitting curve is lower than the true lateral curve, while the linear fitting curve is higher than the true lateral curve. Thus, one can expect that the parabolic fitting (fit method B) will underestimate the dose, while the linear fitting (fit method A) will overestimate it for the body scan. This trend can be seen in Table III; the differences of $CTDI_{wb}$ of IC vs $CTDI_{2D}$ are all negative while $CTDI_{w}$ of IC vs $CTDI_{2D}$ are all positive. In summary, because Bakalyar's CTDI method ($CTDI_{wb}$) underestimates the dose compared to the central slice averaging method ($CTDI_{2D}$), results from the Bakalyar's CTDI method ($CTDI_{wb}$) are closer to the results from the entire volume averaging method ($CTDI_{3D}$), which is theoretically assumed to represent a most accurate model among the methods.

Large CTDI differences were noticed between the results of methods (1)-(3) and that of method (4), as shown in Table III. This can be explained by the nature of the

calculation methods. Methods (1)-(3) use the point dose or plane dose in the central-axial plane of the phantoms, while method (4) numerically averages the entire volumetric dose distribution. The differences are due to the variation of the longitudinal dose distribution. As can be seen in FIG. 14, the dose in the longitudinal direction for both head and body scans decreases with the distance from the central plane; this effect is not considered in methods (1)-(3). It was also found that $CTDI_{wb}$ of IC is slightly inferior to $CTDI_{w}$ of IC

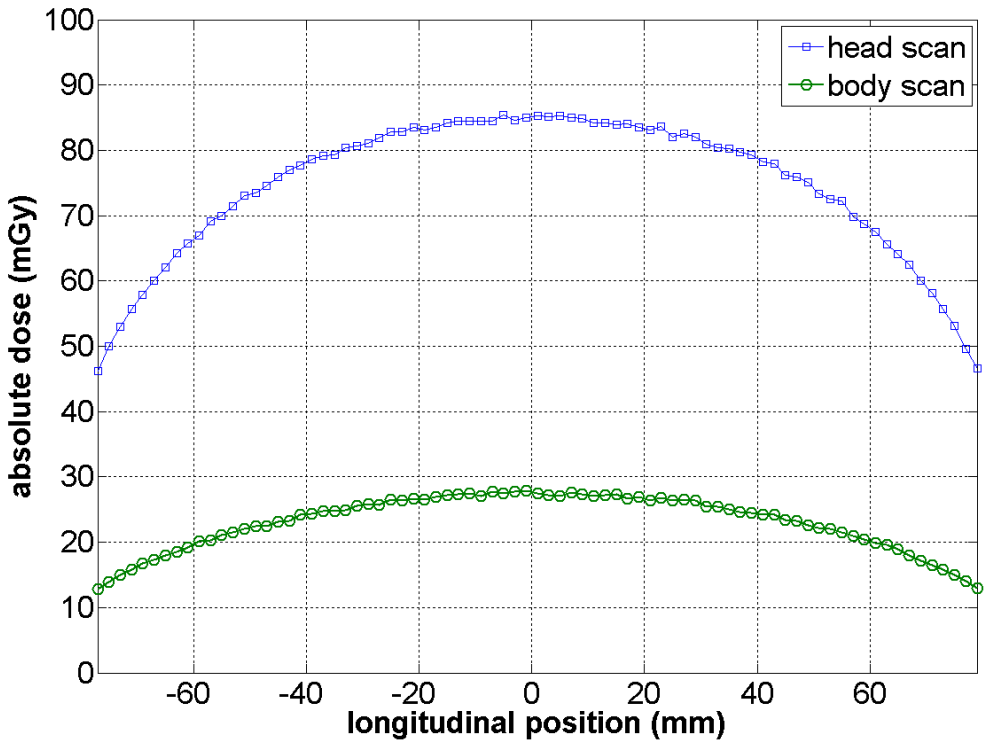

FIG. 14. Longitudinal profiles acquired from standard head and standard body scan. Note the dose drops at the edge location.

for the head phantom but remarkably better for the body phantom compared to $CTDI_{3D}$. Again, this is mainly due to the fitting discrepancies previously described.

Therefore, when IC measurements are chosen to estimate the CBCT dose, such as in the clinical environment, the use of method (2) is recommended to estimate the CBCT dose more accurately than method (1), especially for the body scans. In addition, it should be noted that methods (1) and (2) always overestimate the CTDI values compared to method (4) and the amount of radiation dose is as small as in the mGy level. Thus, the use of methods (1) and (2) would be still acceptable from the patient safety viewpoint.

The image qualities of the new CBCT protocols were not comparable to the old CBCT protocols as expected; e.g. the low-dose head and low-dose thorax could not pass the acceptance criteria of HU verification. Contrast resolution tests and most of the new protocols could not pass the contrast resolution test except the high-quality head and pelvis protocols. Note that all the old protocols passed every test of the QA protocol, which was referenced in Yoo et al.'s paper.[34] From the results, it is concluded that low x-ray intensity (mAs) and fan types are the main causes of HU deviation; low-dose head and low-dose thorax protocols failed the HU verification test for which both used the low mAs. However, it should be mentioned that the standard-dose head protocol did not fail the HU verification test though its mAs was lower than that of the low dose thorax protocol. Thus, one would expect that the HU values could be affected by the combination of both low x-ray statistics and half-fan scan geometry. Due to the HU inaccuracy, CBCT images from low-dose head and low-dose thorax protocols are

inadequate for the purpose of dose calculations unless corrections are applied. Systematic inaccuracies can be expected and accounted for. In addition, it should be noticed that only high mAs protocols such as high-quality head and pelvis protocols passed the contrast resolution test. Thus, when high soft tissue contrast images are needed, the use of a high-quality head or pelvis protocol is recommended depending on the imaging area.

As seen in Table IV, it can be found that high dose protocols (high-quality head, pelvis, pelvis spotlight) produced smaller standard deviations in HU verification and uniformity tests; larger photon statistics of higher dose protocols reduced the noise levels of the CBCT images obtained from higher dose protocols. It is interesting to note that the low-dose thorax protocol passed the HU uniformity test with small standard deviations (3.0) though it provided different HU values (80 HU) compared to other protocols (-3 HU). Thus, every QA test should be performed to accurately evaluate a certain CBCT protocol. It should be noted however that the main point of the OBI system is positional accuracy, which cannot be captured by simple image characterization such as HU accuracy or uniformity tests. Further research is needed to define a task-specific metric of the image quality for the OBI system.

It was found that only partial-angle CBCT scan protocols produce a crescent effect at the interface of two different density materials and the effect was more significant with high mAs; the high-quality head protocol produced a more significant crescent effect than the low and standard dose head protocols. However, within the

homogeneous region, the effect was not significant. More thorough investigation will be necessary for this effect, which is beyond the scope of this study.

6.7. Conclusion

The CTDI of new CBCT protocols was evaluated based on the point dose and numerical averaging methods using IC measurements and MC simulations; the results were compared with old protocols. It was found that CTDI of the new CBCT protocols has been significantly reduced compared to the old protocols. Thus, the use of new CBCT protocols is recommended in order to reduce the patient dose as long as the image quality meets the purpose of the CBCT scan. When high soft-tissue contrast data is needed, high-quality head protocol or pelvis scan protocol is recommended depending on the imaging area. The point dose calculation method showed the $CTDI_w$ values close to the volume averaging method of MC simulations within 9-21% for both partial and full-angle CBCT scan protocols. In addition, the Bakalyar's method ($CTDI_{wb}$) was found to provide more accurate dose estimations within 14%. Because dose deviation of ~10% may be normal in diagnostic x-ray[5-7], the point dose method may be used to estimate the $CTDI_w$ in the clinical CBCT environment. No significant deviations were found between the $CTDI_w$ equation calculations (methods (1) and (2)) and numerical averaging methods (methods (3) and (4)) both partial and full-angle CBCT scan protocols. Thus, the $CTDI_w$ equations (methods (1) and (2)) may be used to estimate the $CTDI_w$ with reasonable accuracy in the partial-angle CBCT scan protocols.

7. CONE BEAM CTDI AND CONE BEAM DLP APPLICATION

7.1. Introduction

As many researchers previously investigated, a direct CTDI application to the cone beam geometry has a critical limitation in measurements for several reasons: first, the active length of the standard pencil CT chamber is ~15 cm, which can not collect the ionizations outside of this range; second, the axial length of the standard PMMA CT phantoms are also ~15 cm, which cannot reproduce the exact amount of scattered radiation in the patient body habitus; third, even if the length of the pencil chamber may be extended from 15 cm to 30 cm or more, it would be technically difficult for the longer chamber to maintain the uniform voltage distribution between the positive and negative grid through the whole length of the chamber. Consequently, this could affect the ion collection efficiency of the chamber and result in larger inaccuracies in the measurements; forth, larger CT phantoms are expensive and heavy (35 cm length body phantom's weight = ~34.5 kg). In sum, the accuracy of the CTDI application to CBCT dosimetry is mainly dependent upon the phantom length and the dosimeter's accuracy.

Some research has been performed in order to evaluate the limitation of direct application of CTDI to CBCT dosimetry by using 30 cm long ion chambers. Mori et al.[5] studied the beam width effect on a 256-slice CT and found that the length of body phantom needs to be larger than 300 mm to collect >90% of dose profile integral (DPI) if

the beam width is over 20 mm. Geleijn et al.[44] introduced a pragmatic metric named average absorbed dose within the pencil ion chamber, D_{100} to characterize the CTDI for a 320 slice CT scanner. Their free-in-air measurements showed excellent agreements between $CTDI_{300air}$ and D_{100air}, while $CTDI_{100air}$ substantially underestimated $CTDI_{300air}$. They also found the same results in their MC simulations that used a 700 mm long CT body phantom. Finally, they concluded that 350 mm long CT phantoms would be adequate to obtain a reasonable CTDI for the 320 slice CT scanner.

Dixon et al.[45,46] introduced the CTDI-aperture ($CTDI_a$) concept and verified its constancy to within a few percent, for a GE Lightspeed 16-slice CT scanner. Mori et al.[5] also showed that DPI for the 256 slice CT scanner is linearly proportional to the beam width, which implies the constancy of the $CTDI_L$. The $CTDI_a$ and $CTDI_L$ are defined as follows:

$$CTDI_a = \frac{1}{a}\int_{-\infty}^{\infty} D(z)dz, \text{ and}$$

$$CTDI_L = \frac{1}{N \cdot T}\int_{-L/2}^{L/2} D(z)dz, \qquad (9)$$

where $a = N \cdot T$ = actual size of beam aperture, and

$D(z)$=absorbed dose at z location.

Note that $CTDI_a$ and $CTDI_L$ are conceptually same except the range of integration and they were validated in the MDCT scanners. However, these concepts were not validated in a CBCT system; also, they did not fully investigate whether their quantities ($CTDI_a$ and $CTDI_L$) can be applicable to the clinical situations in estimating the patient

dose from the CBCT scan or not. In order to ascertain the applicability of the Dixon's CTDI concept to CBCT, one should prove whether the dose length product (DLP), calculated by the CTDI, is close enough to the DPI value. Note that the DPI is a directly integrated dose quantity from an axial dose profile while the DLP value is calculated from the CTDI value.

In this study, the Dixon's CTDI concept was used to estimate the CTDI and DLP values for a commercial CBCT system; $CTDI_a$ was estimated by using an OBI for head and body CBCT scans with various beam widths. A MC technique with extended CT phantoms was used to overcome the limitation of the pencil ion chamber CTDI measurements. The Dixon's point dose method[7] was also used to establish a clinically feasible method in estimating the CBCT doses in CT phantoms. The DLP and DPI values were evaluated in terms of how they can be used as dose descriptors for CBCT, thus providing a gauge for the dose in image-guided radiation therapy (IGRT).

7.2. CBCT beam profile measurements

To check the size of actual beam widths and the relative beam profile of the CBCT scan, the axial dose profiles of the CBCT beams were measured with a radiochromic film (Model GafChromic XR-QA, International Specialty Products, Wayne, NJ). The experiment setup of the axial dose profile measurements is shown in FIG. 15.

The film strips (17×1 cm^2) were placed in a head CT phantom (diameter = 16 cm, length = 15 cm; CIRS, Norfolk, VA) and then a CBCT scan was performed with the

following settings: full-fan mode, 125 kVp, 80 mA, pulsed 25 msec, 360 degree rotation with 660 projections using the OBI system. One strip of the film was exposed for each of the CBCT beam width settings: 1 to 10 cm of nominal reconstructed lengths per 1 cm step.

The net optical density (NOD) to dose calibration for the film was performed on the CBCT beams. As can be seen in FIG. 15(b), a 6 cm^3 ion chamber (Model: 10x5-6, Radcal, Monrovia, CA) and a strip of the film were placed in parallel at the isocenter of the CBCT system and irradiated from a fixed CBCT beam by varying the exposure range from 0 to 16.07 R. All the exposed film strips (both calibration and axial dose profile

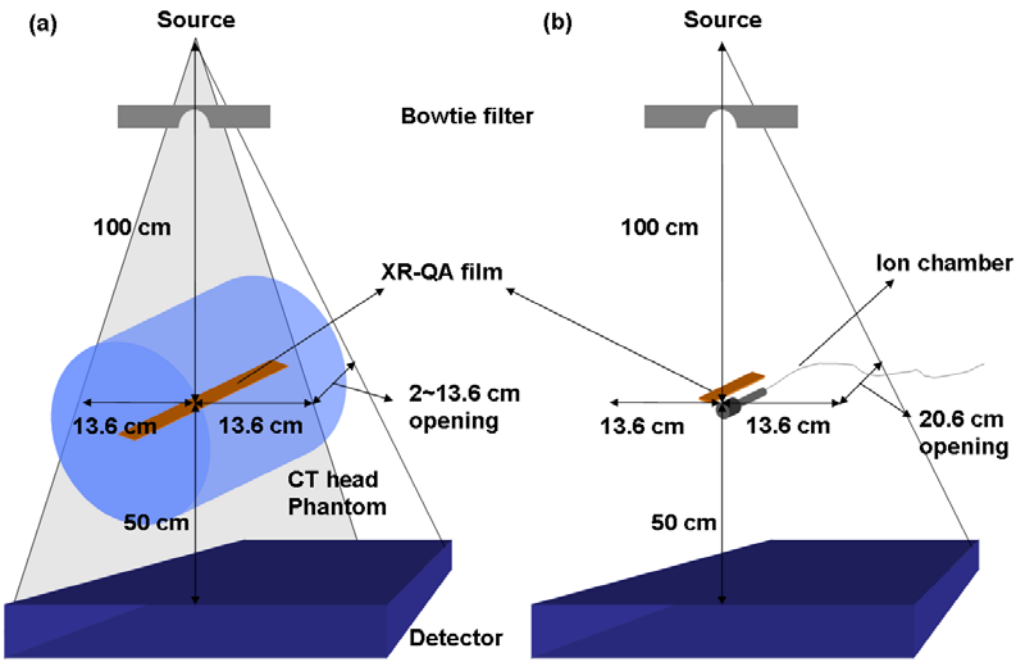

FIG. 15. Radiochromic film measurement setups for various CBCT beam widths. (a) Axial dose profile measurements with film strips. (a) Film calibration with an ion chamber. Note that CT profile measurements were performed by 360 degree CBCT scan procedures, while the film calibrations were performed by 0 degree fixed irradiations.

strips) were placed in a dark place for approximately one day to allow full development. A high-resolution flat-bed scanner (Model: Perfection 4990 Photo, Epson, Long Beach, CA) was used for the film digitization; the film strips were scanned in a reflective, red-green-blue (RGB) mode (16 bit per color), and 72 dot per inch (dpi) resolution with no color correction and the results were saved as in TIFF image file format. The image files were imported into MATLAB software to convert the pixel values (PV) of the film images into exposure (R). Since the absorption spectrum of the radiochromic film shows a maximum sensitivity for the red light as previously studied by Stevens et al.[47], only the PVs of red channel were used in the film dosimetry. To improve the statistics of the PVs, a region of interest (ROI) was drawn for each calibration image with an area of ~500 pixels and the mean value for the ROI was used as a representative of the PVs. The exposure values of the ion chamber were converted into the absorbed dose by multiplying the roentgen-to-rad conversion factor (0.869) and normalized to compare them with the MC results. The one dimensional (1D) bi-cubic interpolation method was used to convert the PVs into the exposures using the calibration data.

7.3. Monte Carlo simulations

The Monte Carlo model of the Varian OBI x-ray tube (developed in Section 4) was employed to simulate the CBCT scans. Using the model, the CBCT scans were simulated for the actual CBCT beam widths of the OBI system in the BEAMnrc/EGSnrc

MC system. The same old CBCT scanning protocol (full angle 360 degree rotation) was also used in the MC simulations.

Two extended MC phantoms were generated to simulate the dose distributions in the CT phantom without losing the long tail portions in the CT dose profiles, shown in FIG. 16. The polymethyl-methacrylate (PMMA) head/body phantoms (physical density, ρ=1.19 g cm^{-3}, 16 cm diameter for head and 32 cm diameter for body, 15.2 cm in length) were CT scanned using the GE Lightspeed RT 4 scanner (GE Medical Systems, Milwaukee, WI) and the CT DICOM files were used to create two extended MC phantoms (60 cm long for the head and 90 cm long the for body). These lengths were,

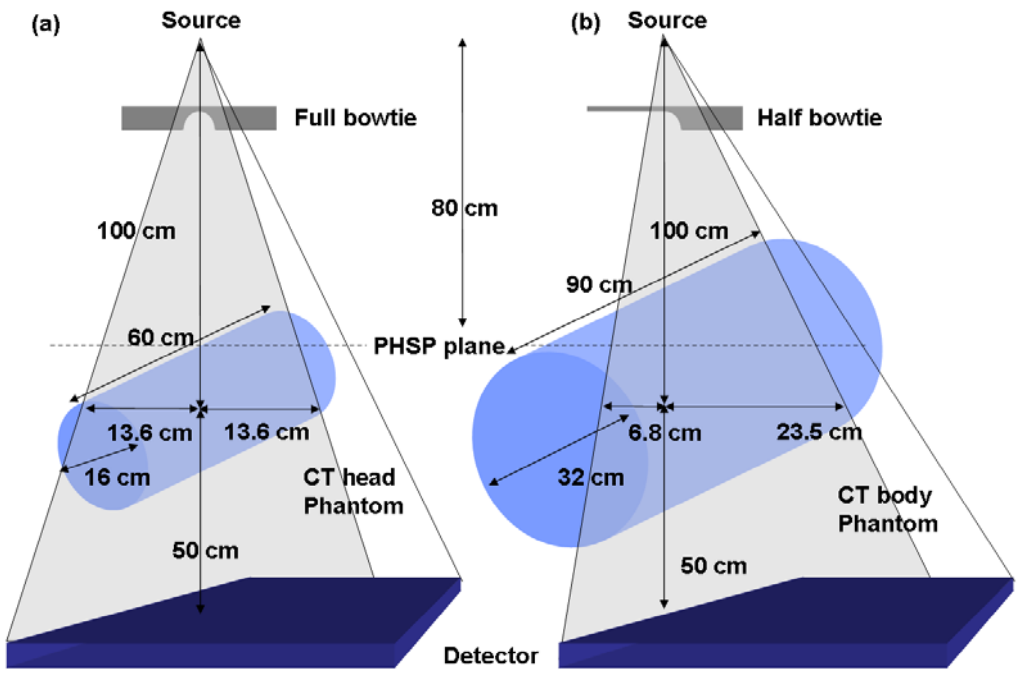

FIG. 16. CBCT irradiation setups with extended CT phantoms simulated in the MC systems – (a) head phantom and (b) body phantom scans. Note that different bowtie filters were employed for each protocol and source-to-isocenter distance was 100 cm.

determined from the results of preceded MC simulations, set to cover the entire dose profile. These extended MC phantoms enabled us to overcome the limitation of the physical CT phantom length.

When creating an extended phantom, a single representative slice of the CT DICOM file was imported into the MATLAB system (Mathworks, Natick, MA) and duplicated the slice into enough slices to compose the longer MC phantom. Then, the DICOM header information of each duplicated slice was modified to align with the location of the slice. With those duplicated DICOM data, both extended head and body MC phantoms were generated using CTCREATE user code.[11]

After the BEAMnrc simulation was finished, the phase space file obtained from the BEAMnrc simulation was re-used as an input source in DOSXYZnrc[31] simulations to calculate the absorbed dose in the extended MC phantoms. For the rotational irradiation simulation, the source type 8 (phase-space source from multiple directions) was used with 660 projections, which was the average number of projections of the OBI system. The number of histories was set to 20 billion, which produced less than 1% statistical uncertainties of the photon fluence. Because the MC simulations produce the absorbed dose per an incident particle, a normalization factor was used to correlate the MC results to physical measurements. A calculation method of the normalization factor was employed from a previous study.[48]

After the CBCT simulations, axial dose profiles at the center and peripheries were obtained by using the STATDOSE user code.[49] Subsequently, the absorbed doses on the dose profile were integrated to derive the DPI per location by the following equations:

$$DPI_{600} = \int_{-300mm}^{300mm} D(z)dz, \text{ (for head scan)}$$
$$DPI_{900} = \int_{-450mm}^{450mm} D(z)dz, \text{ (for body scan)} \quad (10)$$
where $D(z)$ =absorbed dose at z location

Similarly, the cone beam CTDI for each beam width was calculated by the following equations:

$$CTDI_{CB,600} = \frac{1}{T}\int_{-300mm}^{300mm} D(z)dz = \frac{1}{T}DPI_{600}, \text{ (for head scan)}$$
$$CTDI_{CB,900} = \frac{1}{T}\int_{-450mm}^{450mm} D(z)dz = \frac{1}{T}DPI_{900}, \text{ (for body scan)} \quad (11)$$
where T=actual beam width,
z=axial location of profile measurement

As aforementioned, $CTDI_{CB}$ is conceptually equivalent to Dixon et al.'s $CTDI_a$[45,46] and Mori et al.'s $CTDI_L$[5]; it uses actual beam width, not nominal beam width, at the divisor in the above equations. In the $CTDI_{CB}$ calculation, both central and peripheral dose profiles were integrated over the range of 60 and 90 cm in the extended CT phantoms. Similar to the conventional CT system, a weighted $CTDI_{CB}$ ($_wCTDI_{CB}$), was also introduced that can represent the volumetric average of the $CTDI_{CB}$ in the CT

phantoms. The $_{w}CTDI_{CB}$ for each beam width was estimated from the following equation:

$$
\begin{aligned}
&{}_{w}CTDI_{CB} = \frac{1}{3} CTDI_{CB,600,900}^{center} + \frac{2}{3} CTDI_{CB600,900}^{peripheries}, \\
&\text{where } CTDI_{CB,600,900}^{center} = CTDI_{CB,600,900} \text{ at a central axis,} \\
&\qquad CTDI_{CB,600,900}^{peripheries} = \text{averaged } CTDI_{CB,600,900} \text{ at peripheries}
\end{aligned}
\tag{12}
$$

The mean $_{w}CTDI_{CB}$ ($_{w}\overline{CTDI}_{CB}$) was calculated by averaging all the $_{w}CTDI_{CB}$ values; this can be interpreted as a single representative dose index for a certain CBCT scan protocol. Finally, the cone-beam dose length product (DLP_{CB}) was calculated as follows:

$$
\begin{aligned}
&DLP_{CB} = {}_{w}\overline{CTDI}_{CB} \times T, \\
&\text{where } {}_{w}\overline{CTDI}_{CB} = \text{averaged } {}_{w}CTDI_{CB}, \\
&\qquad T = \text{actual beam width}
\end{aligned}
\tag{13}
$$

To validate whether this DLP_{CB} can represent total scan dose or not, a new quantity called weighted DPI ($_{w}DPI$) was introduced that represents the volumetric average of DPI values per each scan as follows:

$$
\begin{aligned}
{}_{w}DPI_{600} &= \frac{1}{3} DPI_{600}^{center} + \frac{2}{3} DPI_{600}^{periphery} \\
{}_{w}DPI_{900} &= \frac{1}{3} DPI_{900}^{center} + \frac{2}{3} DPI_{900}^{periphery}
\end{aligned}
\tag{14}
$$

The DLP_{CB} value was compared with the $_{w}DPI$ value to evaluate the dose difference between two quantities. It should be noted that DLP_{CB} is derived from one representative value, $_{w}\overline{CTDI}_{CB}$, while $_{w}DPI$ is an averaged DPI value directly integrated

from the axial dose profile for a certain beam width. Thus, the closeness of these two quantities can determine whether the $_{w}\overline{CTDI}_{CB}$ value can be used as a CBCT dose index. To verify this, the linearity of $_{w}$DPI per beam width was analyzed for each head and body scan by using a linear regression method; the $_{w}$DPI plot was fitted to a linear equation and R^2 was calculated. Note that $_{w}$DPI is an un-normalized physical quantity of $_{w}CTDI_{CB}$.

For the situation when MC simulations are not feasible, i.e. clinical environment, the accuracy of the $CTDI_{CB}$ estimation was further investigated using Dixon's point dose method[7]; point doses at the center and peripheries in the central slice were extracted from the dose profile for a clinical beam width (20.6 cm) and used to calculate the $_{w}CTDI_{CB}$.

7.4. Results

The calibration curves of radiochromic film and raw film images are presented in FIG. 17. As can be seen, the PV to exposure graph shows an inverse relationship; the exposure to net optical density (NOD) is relatively linear, as expected. Note that the x-axis of FIG. 17(b) is in logarithmic scale (log 10).The exposure values are also presented in the raw film images.

The measured beam width was longer, due to the sampling requirements of the image reconstruction. The actual beam width shown in the CBCT system console was found as follows: 2.0, 3.4, 4.6, 6.0, 7.2, 8.4, 9.8, 11.0, 12.4, and 13.6 cm. These wider beam widths than the console-inputs were similar to the conventional CT system; the CBCT system opens its collimator 1~3 cm wider than its reconstruction image size.

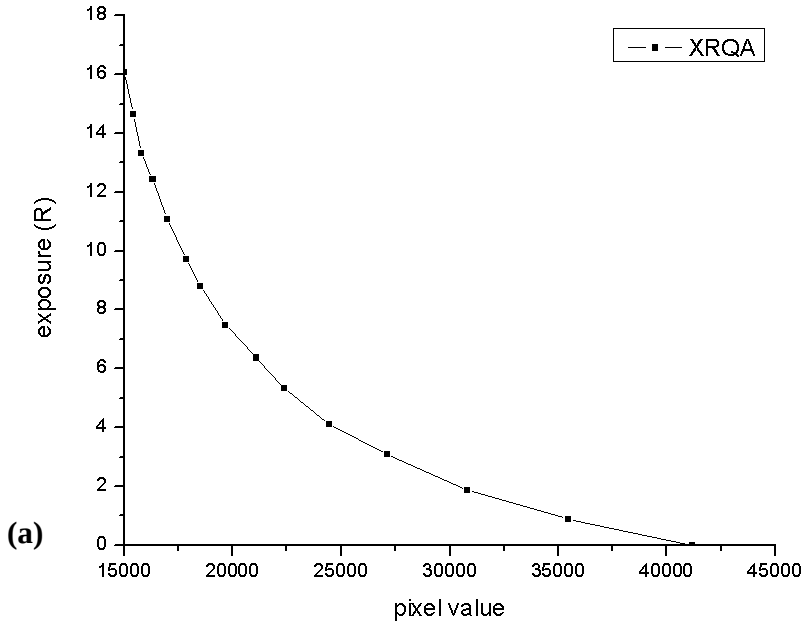
XRQA
exposure (R)
pixel value
0
2
4
6
8
10
12
14
16
18
15000
20000
25000
30000
35000
40000
45000

(a)

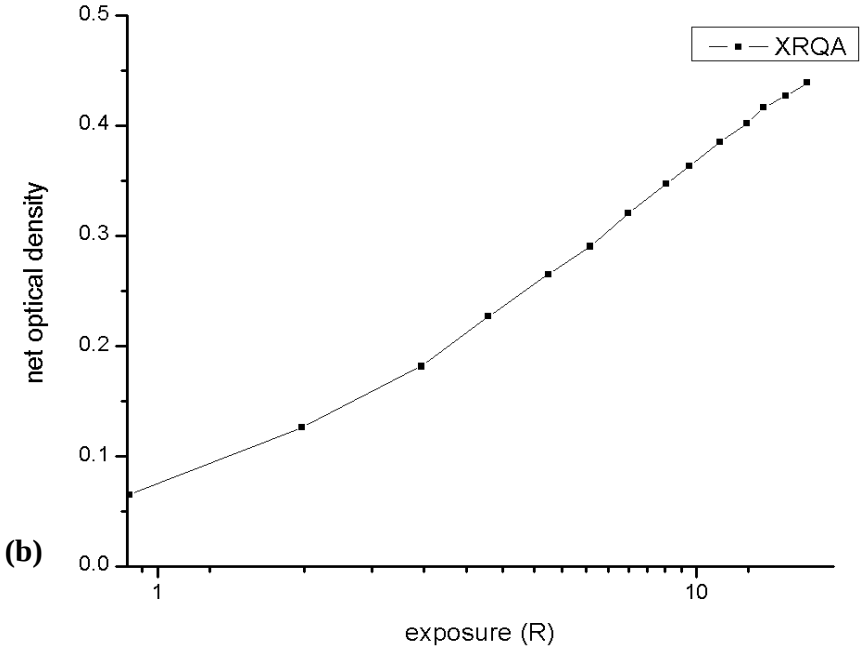
XRQA
net optical density
exposure (R)
0.0
0.1
0.2
0.3
0.4
0.5
1
10

(b)

FIG. 17. Results of the radiochromic film calibration. (a) Calibration curve as pixel value vs. exposure, (b) calibration curve as exposure vs. optical density, and (c) raw film images. Note that the x-axis in Fig. 17(b) is on the logarithmic scale (log 10). The numbers under the raw film images represent the average exposure values (unit in R).

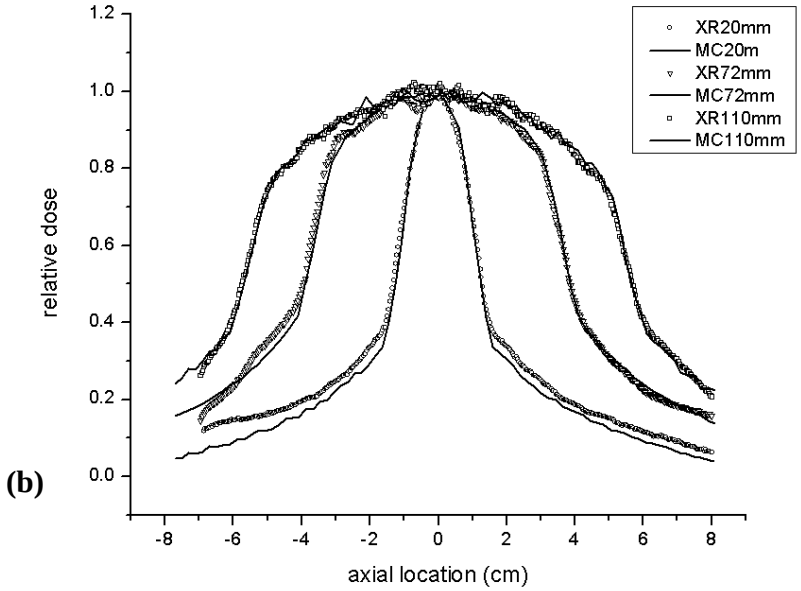

FIG. 18. Results of the axial dose profile measurements with radiochromic films – (a) raw film images and (b) comparison of axial dose profiles between film measurements and MC simulations. Note that all the profiles were normalized to unity using their central dose values.

The raw images of radiochromic film strips used for axial dose profile measurements are presented in FIG. 18(a). The increments of the beam width can be noticeable in the raw image data. The axial dose profiles from the radiochromic film measurements and MC simulations are presented in FIG. 18(b). As can be seen, the profiles of both methods are relatively well matched except at the tail portions.

Mean ${}_{w}\mathrm{CTDI}_{\mathrm{CB}}$ (${}_{w}\overline{CTDI}_{CB}$) was found as 8.590±0.010 cGy for head and 4.518±0.004 cGy for body scan. Note the small standard deviations for both scans.

The axial dose profiles of various beam widths for the head and body scans were presented in FIG. 19. The dose profiles at the center (FIG. 19(a) and (c)) were broader

than those at the periphery (FIG. 19(b) and (d)) , similar to the Mori et al's results. Note that there is no heel effect shown in the FIG. 19, because the anode orientation of the OBI system is perpendicular to the z-axis.

The $_{w}$DPI was quite linear for the beam width variation as shown in FIG. 20. All the R^2 values were found as unity. The detailed linear regression fitting results are shown in Table V.

The comparison between DLP_{CB} and $_{w}$DPI for both head and body CBCT scans are presented in Table VI. As can be seen, both $_{w}$DPI and DLP_{CB} values show increased linearly as the beam width gets wider. The differences are within 0.3%.
The $CTDI_{CB}$ calculated from Dixon's point dose method was found as 8.379 cGy for head and 4.562 cGy using a clinical beam width of 20.6 cm. This shows that the point dose method can estimate the $CTDI_{CB}$ within 3% difference compared to the DPI integration method.

7.5. Discussion and conclusion

These days, the dosimetry for the cone-beam geometry is getting more important from its wide applications – linac mounted or standalone CBCT systems for image guided radiation therapy (IGRT), C-arm interventional machines, multi-slice CT scanners (256 and 320 slices) for cardiology study. However, there is no consensus regarding

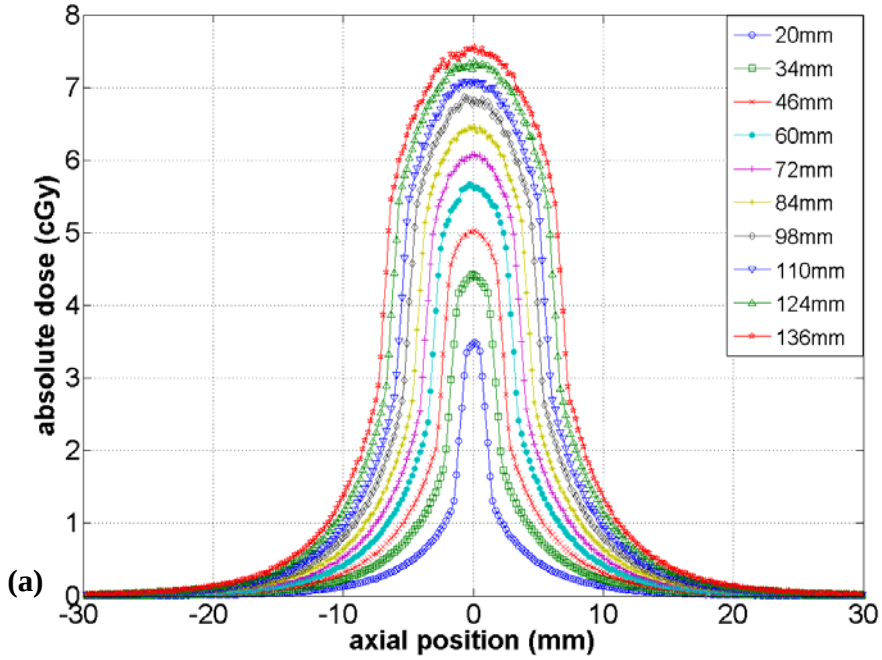
absolute dose (cGy)
axial position (mm)
20mm
34mm
46mm
60mm
72mm
84mm
98mm
110mm
124mm
136mm

(a)

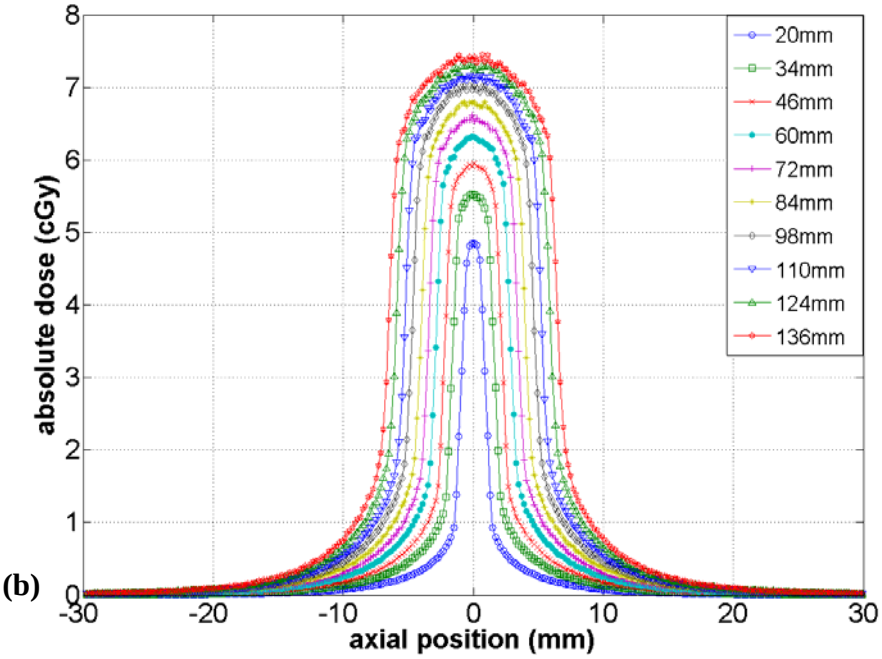
absolute dose (cGy)
axial position (mm)
20mm
34mm
46mm
60mm
72mm
84mm
98mm
110mm
124mm
136mm

(b)

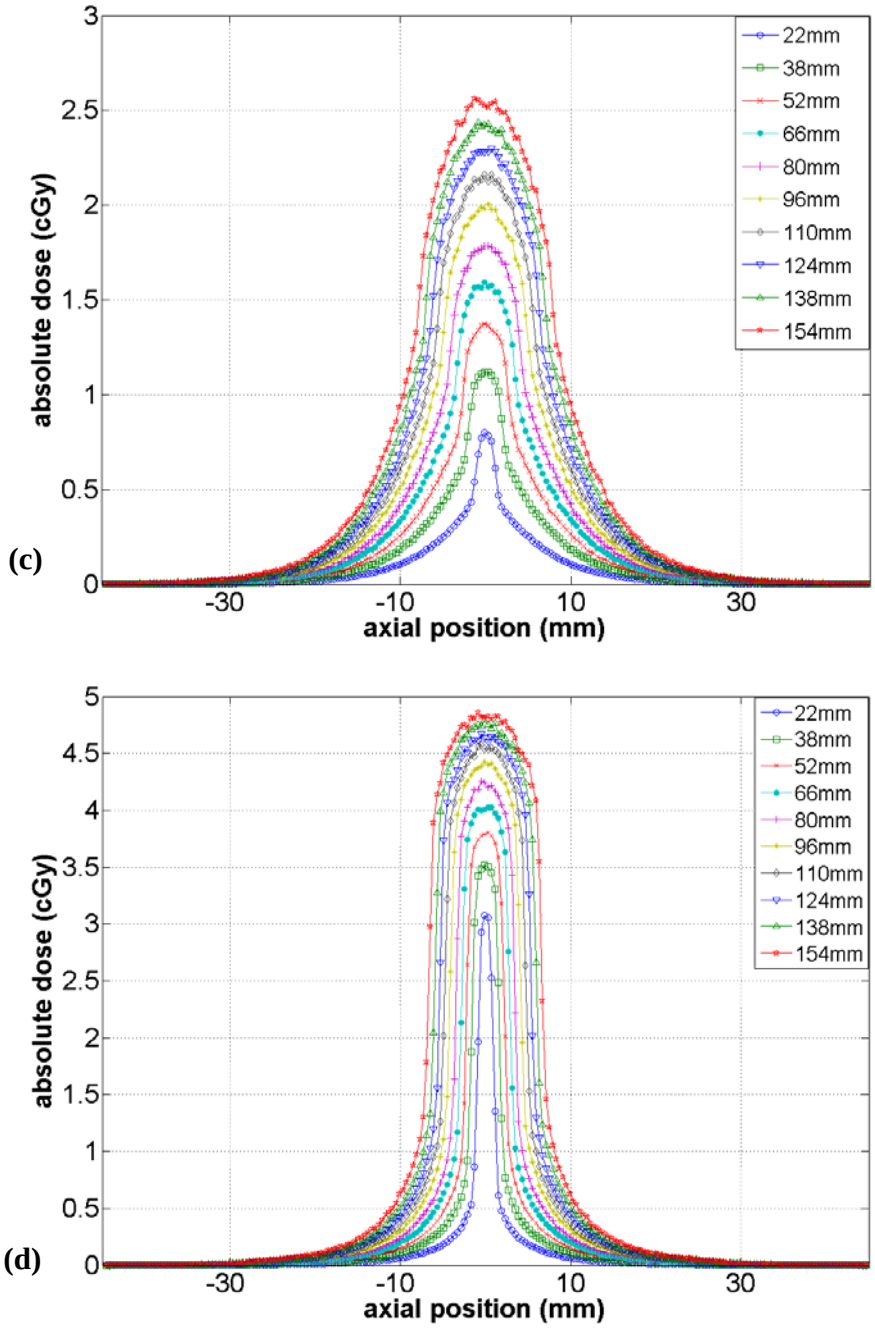

FIG. 19. Axial dose profiles of various beam widths at the (a) center and (b) 12 o'clock locations for the head scans and at the (c) center and (d) 12 o'clock locations for the body scans.

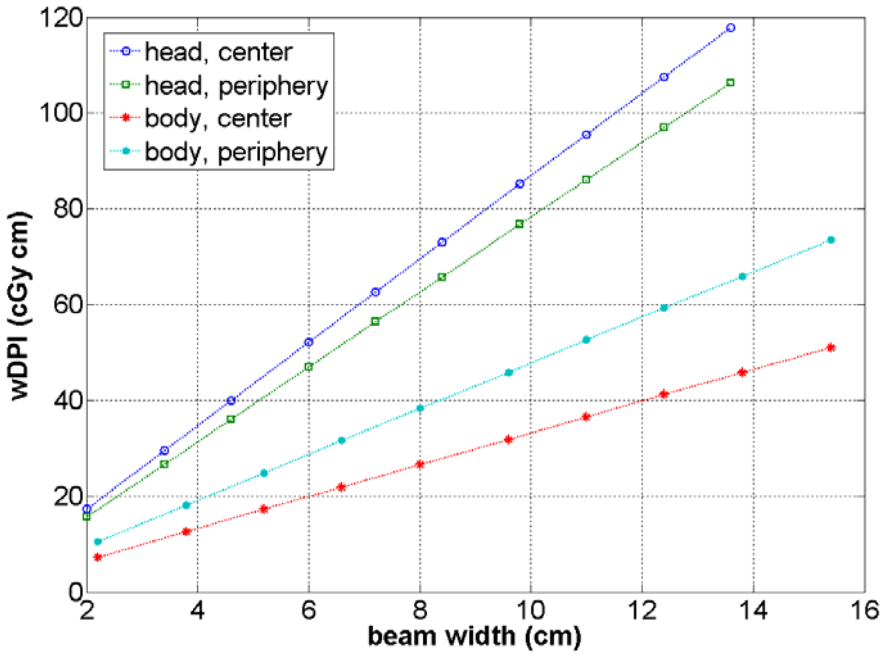

FIG. 20. Weighted dose profile integrals ($_{w}$DPI) as a function of beam width for the head and body CT phantoms. Note that the variations of the $_{w}$DPI are linear for both central and peripheral profiles.

how to evaluate the radiation dose from the CBCT systems; some researchers investigated the CTDI application to the CBCT dose estimation and others performed direct absorbed dose calculations in the patients from MC simulations. Although the latter method can provide more accurate dose information such as 3D dose distribution, it requires extensive work impractical in clinical environments. In addition, heavy computation time is a disadvantage of MC methods.

In this study, a MC method was employed to accurately estimate the CTDI and DPI for a clinical CBCT system. The MC model was also validated by comparing the CBCT beam profiles obtained from radiochromic film measurements to the MC simulations.

Table V. Linear regression fittings of $_{w}$DPI curves for head and body scans shown in FIG. 20. Both center and peripheral $_{w}$DPI values are fitted to first-order linear curves.

		Linear regression fitting: y=ax+b		
		a	b	R^2
Head	Center	8.6616	0.144	1
	Periphery	7.8157	0.0787	1
Body	Center	3.3159	0.0654	1
	Periphery	4.7764	0.0471	1

Table VI. Comparison of DLP_{CB} and $_{w}$DPI values for head and body CBCT scans. Note that the differences are less than 0.3%.

	Head CBCT Scan				Body CBCT Scan		
Beam width	$_{w}$DPI	DLP_{CB}	Diff (%)	Beam width	$_{w}$DPI	DLP_{CB}	Diff (%)
2	17.16	17.18	0.12	2.2	9.94	9.94	0.00
3.4	29.24	29.21	-0.10	3.8	17.17	17.17	0.00
4.6	39.56	39.51	-0.13	5.2	23.50	23.49	-0.04
6	51.58	51.54	-0.08	6.6	29.84	29.82	-0.07
7.2	61.90	61.85	-0.08	8	36.18	36.14	-0.11
8.4	72.15	72.16	0.01	9.6	43.36	43.37	0.02
9.8	84.26	84.18	-0.09	11	49.72	49.69	-0.06
11	94.49	94.49	0.00	12.4	56.02	56.02	0.00
12.4	106.38	106.52	0.13	13.8	62.69	62.34	0.08
13.6	116.58	116.83	0.21	15.4	69.43	69.57	0.20

This MC approach removed the technical limitation of the 100 mm pencil ion chamber measurements in the CTDI estimation in CBCT ($CTDI_{CB}$).

Due to the limitation of physical measurements, Dixon′s point dose method is a common approach to estimate the $CTDI_{CB}$). However, no validation research has yet been performed to determine the accuracy of the point dose method in estimating the $CTDI_{CB}$. In this study, the accuracy of the point dose method was investigated by comparing the $CTDI_{CB}$ values with the result of DPI method. The $CTDI_{CB}$ estimation from the point dose method could yield a

reasonable reflection (within 3%) of dose index for a clinical beam width of 20.6 cm. Thus, the point dose method is found to be a clinically useful tool in estimating $CTDI_{CB}$ of the OBI system.

It should be mentioned that $CTDI_{CB}$ and DLP_{CB} methods only provide an *estimation* of average absorbed dose to a local body section (head and body), not individual organ doses. Thus, they are not appropriate tools to assess the radiation risk of the CBCT. Although one can derive a conversion factor to relate DLP_{CB} to effective dose (ED), this process inevitably requires a MC simulation with real patients or anthropomorphic phantom geometries in order to estimate the individual organ doses.

This study has a limitation. Only one specific CBCT system (Varian OBI model) was employed, which is the only model available in our institution. Other CBCT systems such as Elekta XVI and Varian Acuity may produce different results. Further investigation will be helpful to understand the applicability of $CTDI_{CB}$ and DLP_{CB} to other CBCT systems.

This study applied the CTDI and DLP concepts in CBCT dosimetry, validated the applicability of CTDI as a dose index for CBCT, and demonstrated a clinically feasible approach to estimate the CBCT dose (DLP_{CB}) using the point dose method. This method can be readily applicable to other cone-beam or multi-detector CT (MDCT) system.

8. ORGAN AND EFFECTIVE DOSE CALCULATIONS USING A VOXELIZED PHANTOM MONTE CARLO MODEL

8.1. Introduction

Since the introduction of radiation to healthcare, considerable effort has been made to accurately estimate the radiation dose to the patient following the ALARA (as low as reasonably achievable) principle. For computed tomography (CT), the computed tomography dose index[4] (CTDI) and dose length product (DLP) have served as standard dose descriptors that provided estimations of the patient dose from CT imaging procedures. Despite the simplicity and conveniences, these quantities are not designed to estimate any radiobiological response to the human body from radiation. However, these quantities are useful for the machine output check.[50]

Beside the CTDI, International Commission on Radiological Protection (ICRP) proposed the effective dose (ED) concept incorporating the radiosensitivity of individual organs based on the atomic bomb survivors' data. By multiplying the tissue weighting factors to the organ doses and summing them, one can evaluate the ED; in part, this may be used for a more realistic measure of the radiation dose effect to the human body. However, it should be mentioned that the ED is originally proposed to evaluate the radiation detriments to the general population or the protection of radiation workers.[51] That is, it may not be appropriate to use it for the estimation of the radiation risk in

patients. Thus, as Drexler et al.[52] suggested, it should be used for the risk comparison purpose within similar age and gender distributions.

The Monte Carlo (MC) technique has been introduced to estimate the ED with stylized phantoms[53-55] or anthropomorphic phantoms[56-60] to overcome the limitation of physical measurements. However, paradoxically MC models need to be validated by the physical measurements. Several studies have validated their MC simulations with thermoluminescent dosimeter (TLD) measurements.[61-65] Their MC results were within the range of ~15 % to the measurements.

Recently, CT technology has advanced to cone-beam geometry in order to achieve wider scan coverage per rotation, while minimizing the scan time. Although there are several CTDI studies[5-9,66] performed on CBCT imaging, the dosimetric information of cone-beam CT (CBCT) is still limited especially for the ED evaluation. In addition, to the best of our knowledge, no ED research has been performed for pediatric CBCT with both MC simulations and measurements.

In this study, a CBCT MC model was established in BEAMnrc/EGSnrc MC system[10] and used to estimate the absorbed doses and the ED from the CBCT. To validate the MC model, an anthropomorphic phantom and metal-oxide-semiconductor-field-effect transistor (MOSFET) technology were employed for the dose measurements. A CT-scanned voxelized MC phantom was generated from the physical phantom for the dose calculations in the MC simulations. Finally absorbed doses and the ED were compared between the two methods.

8.2. MOSFET measurements

The absorbed doses for individual organs were measured in a 5-year-old pediatric anthropomorphic phantom (model: ATOM 705-D, CIRS, Norfolk, VA) using a Varian On-Board Imager® (OBI, Varian Medical Systems, Palo Alto, CA) mounted on the sides of a linear accelerator. The experimental setup is presented in FIG. 21. The pediatric phantom is made of bone, lung, and soft tissue equivalent materials whose compositions are based on the reference man[67] and ICRU report 44.[68] The specific dimensions of the phantom are as follows: height 110 cm, weight 19 kg, 14×17 cm^2 thorax. The phantom consists of 26 contiguous 2.5 cm thick slices. Each slice has several 5 mm dosimeters,

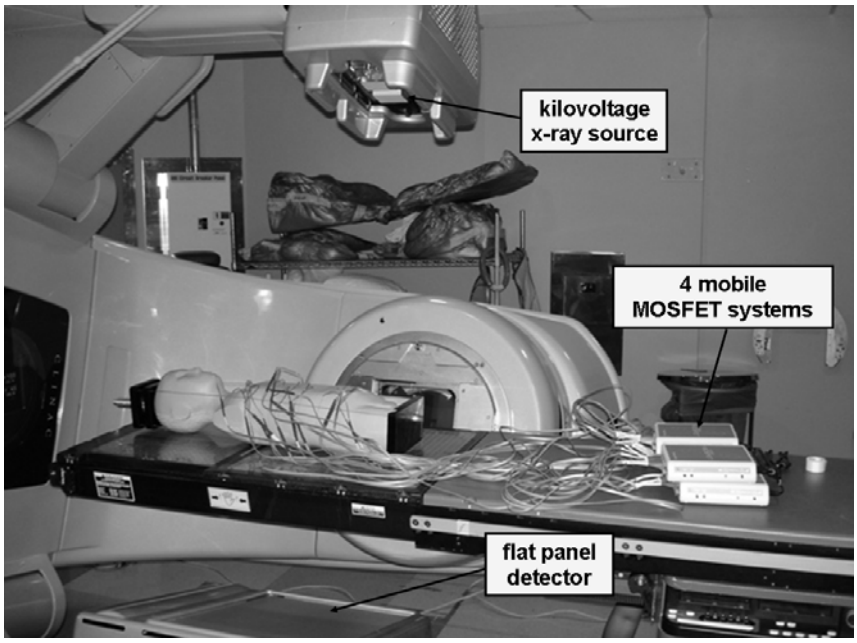

FIG. 21 MOSFET measurement setup for a 5-year-old anthropomorphic phantom CBCT. Twenty MOSFET detectors were placed at each organ location connected to four mobile MOSFET systems.

the locations of the dosimeters were carefully chosen based on the anatomical information obtained from the manufacturer.

Twenty high sensitivity diagnostic radiology MOSFET detectors (Model: TN-1002RD, Best Medical Canada, Ottawa, Canada) were placed at the assigned organ locations and connected to four mobile MOSFET wireless systems (Model: TN-RD-70-W, Best Medical Canada, Ottawa, Canada) to obtain the absorbed dose readings. The detectors were calibrated by adding a 1.5 mm aluminum filter to a conventional radiographic x-ray tube with HVL of 4.2 mm Al to approximate the beam quality of the CBCT (effective energy: 55.6 keV). Individual MOSFET detectors were calibrated with a 6 cm^3 ion chamber (Model: 10x5-6, Radcal, Monrovia, CA).

Using the imaging system, the phantom was scanned over the abdominal and pelvic regions (section number 19 at the isocenter) using "full-fan" mode with two x-ray source parameters: (1) standard dose mode with peak voltage of 125 kVp, tube current of 80 mA, and exposure time of 25 msec, and (2) low dose mode with 125 kVp, 40 mA and 10 msec. The beam collimation was 20.6 cm, which produced the axial dimension of a reconstructed image as 15.5 cm. Other CBCT scan parameters included effective focal spot size of 0.4-0.8 mm, source to isocenter distance of 100 cm, source to detector distance is 50 cm, total number of projections 650-700, field of view 25×25 cm^2, and full bowtie filters.

8.3. Monte Carlo simulations

MC simulations of the CBCT irradiation were performed by using the BEAMnrc/EGSnrc MC code system.[10] A personal computer (Intel Pentium 4, 3.8 GHz CPU, 2 GB RAM) with the Linux operating system was employed for the simulations. All the x-ray tube components of the CBCT system were provided by the manufacturer and implemented in the BEAMnrc/EGSnrc system as shown in FIG. 1 in Section 4.2. A phase space file, which contains all the particles' spatial and directional information with energies, was obtained at the source to surface distance (SSD) = 80 cm. Then, the particles in the phase space file were re-transported to the voxelized phantom generated

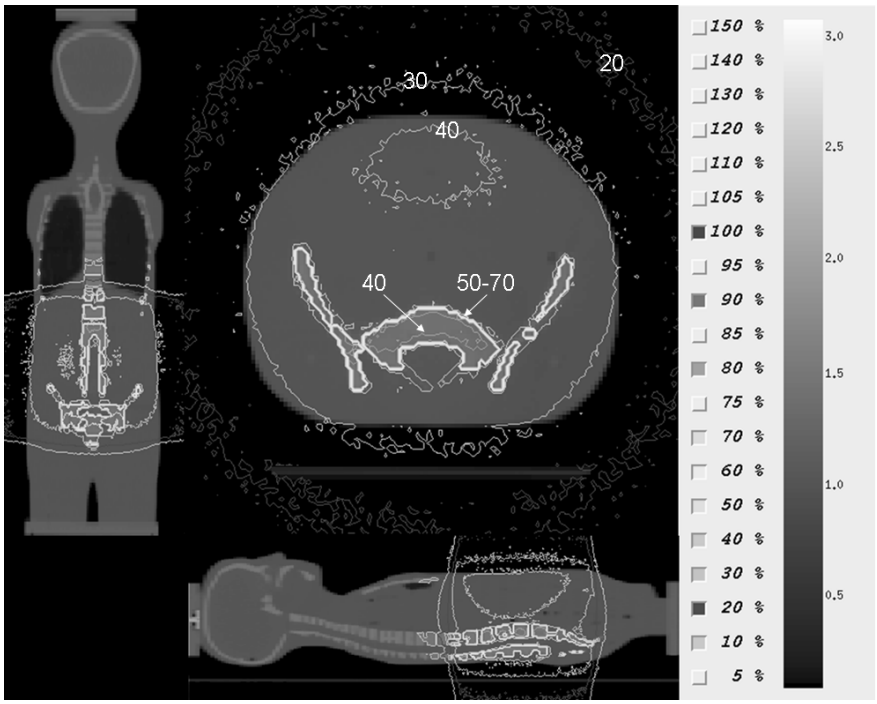

FIG. 22 Abdominal/pelvis dose distributions of the pediatric CBCT scan. Axial, coronal, and sagittal views are presented with percent dose level and density bar (g cm^{-3}).

with the anthropomorphic phantom CT data in the DOSXYZnrc user code.[31] The CTCREATE user code was employed to voxelize the phantom CT data into a MC phantom with the voxel dimension of $2\times2\times2$ mm^3. The number of histories was one billion for the BEAMnrc simulation and nine billion was used in the DOSXYZnrc dose calculation. The detailed MC transport parameters are as follows: ECUT= 512 KeV, PCUT= 1 keV, Bremsstrahlung cross sections = NIST, Photon cross sections = XCOM; all the low energy photon physics options were turned on for more accurate simulations.

After the DOSXYZnrc calculation, the absorbed doses for each individual organ were extracted from the calculation by using DOSXYZ_SHOW user code[35] as shown in FIG. 22 and compared with the MOSFET measurements. Because DOSXYZnrc code produces the absorbed dose per incident electron particle (i.e. relative dose distribution), the skin dose in the MC data was used to normalize the MC dose distribution to the MOSFET measurements.

8.4. Effective dose calculations

The ED for standard dose and low dose modes were evaluated from the organ doses by applying ICRP Publication 60 tissue weighting factors, assuming the radiation weighting factor of 1.0 for x-ray irradiation.[69] The organ doses were computed from the acquired absorbed doses by considering the mass distribution of the individual organs. The ED is formulated as follows:

$$ED = \sum W_{Ti} \cdot H_i, \quad (15)$$

where W_{Ti} = tissue weighting factor of individual organ,

$H_i = W_{Ri} \cdot D_i$ = equivalent dose of individual organ,

W_{Ri} = radiation weighting factor ($W_R = 1$ for x-ray),

D_i = individual organ dose.

Organ dose for colon D_{colon} was evaluated by following the weight fraction formula of ICRP Report 67 shown below[70]:

$$D_{colon} = 0.57 D_{ULI} + 0.43 D_{LLI} \quad (16)$$

where D_{ULI} = average organ dose of upper large intestine,

D_{LLI} = average organ dose of lower large intestine.

Similarly, the D_{ULI} was also calculated by weight fractioning of the organ dose to the transverse and ascending colon and D_{LLI} was calculated by weight fractioning of the organ dose to the descending and sigmoid-rectum colon based on the data of ICRP report 23.[67] For the red bone marrow, Cristy and Eckerman's fractional distribution of active marrow was employed.[55]

Because of the technical difficulty in directly measuring dose to the bone surfaces, the dose value of red bone marrow was re-used to estimate the dose to the bone surface.[71] However, we employed the dry fat-free skeleton weight fractions and the ratios of cortical and trabecular bone for the 5-year-old from ICRP Report 70[72] to derive the weight fractions of cortical bone in each bone location. Then, we multiplied the c-factor of B100 bone equivalent material (3.156 for x-rays with effective energy of 55.6 keV)[73] to this value to derive the final bone surface dose. The equation for this procedure is as follows:

$$D_{bs} = \left(\sum_i D_{rbm,i} \cdot W_{dry,i} \cdot W_{cort,i} \right) \times c\text{-}\,factor \quad (17)$$

where D_{bs} = bone surface dose,

$D_{rbm,i}$ = red bone marrow dose in each bone location, i,

$W_{dry,i}$ = weight fraction of dry bone in each bone location, i,

$W_{cort,i}$ = mass portion of cortical bone in each bone location, i,

$$c\text{-}\,factor = \frac{(\mu_{en}/\rho)_{bone\_B100}}{(\mu_{en}/\rho)_{tissue\_soft}}, \text{where}$$

$(\mu_{en}/\rho)_{bone\_B100}$ = mass energy coefficient for B-100, and

$(\mu_{en}/\rho)_{tissue\_soft}$ = mass energy coefficient for soft tissue.

For the skin dose calculation, a detector was placed on the surface of the phantom at the center of the irradiation field. We estimated the whole phantom skin area of the male phantom based upon information provided by manufacturer, assuming that the phantom is approximately an elliptical shape. The estimated whole skin area was 5,368 cm^2 and the irradiated skin area was 1,005 cm^2. The area fraction of the skin was estimated to be 0.187, which was multiplied by the entrance skin dose reading to evaluate the average skin dose.

8.5. Results

As can be seen in Table VII, a similar absorbed dose distribution was found in both MOSFET measurements and the MC simulation. The highest absorbed doses were recorded for the skin, stomach and ascending colon in both modalities. It was also found that both standard dose and low dose mode showed the same pattern in both modalities.

The absorbed doses ranged from 0.07 to 7.22 cGy in the MC simulation and from 0.05 to 7.22 cGy in the MOSFET measurements for the standard dose mode. For the low dose mode, the absorbed doses were from 0.02 to 1.56 cGy in both MC and MOSFET results. The dose differences between MC and MOSFET ranged from 0% to 40%; the dose differences for in-field organs were generally within 10%, while the differences for out-field organs were from 20 to 40%.

It was found that the ED from the MC simulation is quite close to that of MOSFET measurements; in the MOSFET measurements, the ED was 37.80±0.71 mSv

Table VII Absorbed doses obtained from MOSFET measurements and MC simulations for abdominal CBCT imaging.

Organs	Standard dose mode (cGy)			Low dose mode (cGy)		
	MOSFET	MC	% diff	MOSFET	MC	% diff
BM / Mandible	0.05±0.04	0.07	-40.00	0.02±0.03	0.02	0.00
Thyroid	0.15±0.08	0.12	20.00	0.05±0.01	0.03	40.00
Thymus	0.36±0.04	0.27	25.00	0.08±0.01	0.06	25.00
BM / Ribs	0.31±0.04	0.30	3.23	0.09±0.03	0.07	22.22
Breast (Left)	0.43±0.10	0.29	32.56	0.11±0.04	0.06	45.45
Lungs / Middle	0.86±0.02	0.64	25.58	0.17±0.01	0.14	17.65
Esophagus	1.28±0.10	1.21	5.47	0.25±0.02	0.26	-4.00
BM / Spine	2.01±0.07	2.46	-22.39	0.42±0.06	0.53	-26.19
Spleen	5.75±0.25	5.83	-1.39	1.28±0.09	1.26	1.56
Liver	6.17±0.18	6.26	-1.46	1.36±0.06	1.35	0.74
Kidney	5.68±0.20	5.95	-4.75	1.22±0.06	1.28	-4.92
Pancreas	5.57±0.16	5.92	-6.28	1.19±0.03	1.28	-7.56
Stomach	6.82±0.22	6.81	0.15	1.47±0.10	1.47	0.00
Intestine	6.18±0.24	6.21	-0.49	1.37±0.07	1.34	2.19
Ascending colon	6.95±0.37	6.51	6.33	1.53±0.12	1.40	8.50
BM / Pelvis	5.15±0.23	5.65	-9.71	1.12±0.09	1.22	-8.93
Ovaries (gonad)	5.37±0.29	4.96	7.64	1.13±0.02	1.07	5.31
Bladder	6.17±0.08	5.31	13.94	1.26±0.09	1.15	8.73
Descending colon	5.06±0.19	4.87	3.75	1.11±0.01	1.05	5.41
Skin	7.22±0.30	7.22	0.00	1.56±0.07	1.56	0.00

BM is the abbreviation of bone marrow. Note that the MC data is normalized to the MOSFET measurements based on the skin dose. The difference is calculated by following equation: $Dose_{MOSFET} - Dose_{MC} \Big/ Dose_{MOSFET} \times 100$.

for the standard dose mode and 8.09±0.16 mSv for the low dose mode; the ED was 36.08 mSv for the standard dose mode and 7.78 mSv for the low dose mode in the MC simulation.

8.6. Discussion

Absorbed doses were measured and simulated with the pediatric phantom for the abdominal pelvis CBCT protocol. From the absorbed dose data, the effective doses were also calculated and compared between the measurements and the MC simulation. As expected, the doses were highest for organs in the field of view (skin, colon, and stomach), while the doses in more superior body regions were relatively low. Brenner[74] calculated the organ dose of the abdominal multi-detector CT (MDCT) as a function of age at CT examination. This study's CBCT organ dose range for the standard dose mode was from 5.1 to 7.2 cGy (for abdominal organs), which is considerably higher than that of Brenner's estimation (0.4 to 1.7 cGy at age 5). However, the organ doses for low dose mode showed comparable values to the Brenner's results.

The same trend was found in ED estimations. Thomas and Wang[75] reported that the ED of abdominal/pelvic MDCT for 5-year-old patients was 8.4 mSv. In this study, the ED of pediatric CBCT for standard dose mode was found to be considerably higher than that of MDCT, while it was comparable for low dose mode. This large discrepancy between standard dose mode CBCT and MDCT could be caused by differences in the tube current-time product (mAs) and the irradiation pattern. Note that each organ in

CBCT was irradiated with ~1340 mAs per a single rotation, while in MDCT, each organ is normally exposed to an approximate range of 200 mAs per several rotations. In sum, the overall higher mAs of CBCT with the different irradiation pattern resulted in higher organ doses and consequently a higher ED than those of MDCT. It was found that the MC technique can predict the absorbed doses of the CBCT irradiation well enough within the reasonable accuracy. As can be seen in the result, the dose differences for in-field organs were approximately 10%, which is acceptable, because the intrinsic accuracy of the dosimeter for this CBCT photon energy range (55.6 keV) is about 5-10% at best. However, large deviations (20-40%) between the measurement and the simulations were noticed for the out-field organ doses. This is mainly due to the lack of photon statistics; uncertainty of the MOSFET measurements increases significantly in the low radiation exposure.[76] The situation is similar for the MC simulation as it is difficult to obtain a statistically sufficient number of photons in the out-field location.

The other limitation to this study is the number of MOSFET detectors used in the physical measurements; this limitation mainly comes from the actual cost of the detection systems. i.e., there is a trade-off between the cost of the detectors and the accuracy of the organ dose estimation; more detectors will produce more accurate organ dose estimation. In this study, each organ dose was assumed to represent the average organ dose for that organ. Fortunately, CT beam rotates 360 degrees around the phantom, which will produce relatively uniform dose distributions inside individual organs. Although this effect would

slightly compensate for the lack of the detectors, further research would be necessary to find the adequate number of detectors for accurate organ dose measurements.

Another limitation to the study is the use of the standard anthropomorphic phantom. Although this type of phantom would be expected to yield more accurate dose estimates than the stylized phantom, it is still representative of a "standard" patient. Actual patient organ doses may be different from the model we used.

8.7. Conclusion

A MC model for pediatric CBCT was established and validated by the comparison of the absorbed doses and ED in the MOSFET measurements. It was found that the MC model can successfully estimate the absorbed doses and the ED for the pediatric CBCT protocol with reasonable accuracy. This MC model can be extended to multi-detector CT dosimetry for future study.

9. RADIATION DOSE FROM CONE BEAM COMPUTED TOMOGRAPHY IN A PEDIATRIC PHANTOM: RISK ESTIMATION OF CANCER INCIDENCE

9.1. Introduction

The use of image-guided radiation therapy (IGRT) to improve the radiation conformity and accuracy of tumor localization while sparing normal tissues is gaining popularity. By using an integrated kilo-electron volt (keV) x-ray tube and an amorphous silicon flat panel detector on the linear accelerator, errors in patient positioning can be corrected immediately prior to the initiation of radiation therapy in the treatment room. Cone beam computed tomography (CT) is normally acquired to verify the location of the tumor in three dimensions.

There have been several reports about absorbed dose from cone beam CT (CBCT). Islam et al.[77] have investigated patient doses from the X-ray Volume Imaging (XVI) system (ELEKTA Oncology systems, Norcross, GA). They found that the maximum dose for the body phantom (30 cm diameter cylinder) was in the range from 1.8 to 2.3 cGy for 120 kVp and from 2.8 to 3.5 cGy for 140 kVp beams. For the head phantom (16 cm diameter cylinder), the maximum dose values were from 1.5 to 2.0 cGy for 100 kVp and from 2.6 to 3.4 cGy for 120 kVp beams. It should be mentioned that these cone beam CT doses were acquired with relatively smaller mAs (660 mAs) compared to the Varian On-Board imager® (OBI) (mean: 1300 mAs). Wen et al.[78] measured intensity modulated

radiation therapy (IMRT) patient doses for OBI using thermoluminescent dosimeters (TLD) in the region of the prostate gland using a RANDO® phantom (The Phantom Laboratory, Salem, NY). In summary, they found that the surface doses at the anterior and posterior locations ranged from 3 to 6 cGy and the largest doses were 6 –11 cGy at the femoral head and neck. Song et al.[9] reported the weighted computed tomography dose indices ($CTDI_w$) of the CBCT for both XVI and OBI systems. They found that the weighted computed tomography dose indices ($CTDI_w$) for OBI were 8.3 cGy for a head scan and 5.4 cGy for a body scan in standard dose mode.

Hurwitz et al.[79] reported the radiation doses from cardiothoracic multi-detector CT protocols in an anthropomorphic female phantom. They described a methodology to measure absorbed doses using metal-oxide-semiconductor-field-effect transistor (MOSFET) detectors in the phantom and estimated the lifetime attributable risk (LAR) and relative risk (RR) from the measured absorbed doses.

Due to the nature of IGRT and the radiosusceptibility of children, the radiation dose to the pediatric patients can be a great concern and needs to be carefully regulated. Because radiation treatments for patients are usually fractionated by 20 treatments, the total radiation dose from CBCT will be a factor of 20 greater than a single CBCT dose. Comparing the target prescription dose of radiation therapy, 50-70 Gy, the CBCT dose can be considered as negligible. However, one should be aware that this CBCT dose is distributed to the entire imaging region that contains a large amount of normal tissue, while the prescription dose is only focused on the tumor area. Despite all the works cited

above, to the best of our knowledge, the effective dose and cancer risk estimation of CBCT for pediatric patients has not been fully investigated.

The purpose of this study consisted of three stages: (1) to measure the absorbed doses from Varian OBI's CBCT in a 5-year-old phantom with MOSFET detectors considering the image quality variation, (2) to derive the effective dose from calculated organ doses, and (3) to estimate LAR and RR from the organ doses. The same method used in Hurwitz et al.'s study[79] was employed but it was used for the pediatric CBCT.

9.2. Materials and Methods

Absorbed doses were measured in the pediatric anthropomorphic phantom (model: ATOM 705-D, CIRS, Norfolk, VA) using On-Board Imager® (Varian Medical Systems, Palo Alto, CA) in Section 8. The detailed experimental setup – CBCT scan protocol, anthropomorphic phantom specification, and MOSFET detectors – can be referenced in Section 8.2.

In IGRT, the radiation therapist generally uses the bone structure to estimate the alignment of the patient's position. Thus, the image qualities for both standard and low dose mode were evaluated; a region of interest was selected with the size of 20×20 pixels at the center of the images and the image qualities were analyzed based on the Hounsfield units (HU) statistics – mean value, standard deviation and noise.

Effective dose (ED) value, calculated from Section 8, was also used in this study. The detailed ED calculation method can be referenced in Section 8.4.

The LAR of radiation-induced cancer incidence was evaluated in various organs from a single scan for both the standard and low dose modes of CBCT. LAR of cancer incidence for several solid tumors have been tabulated as a function of age at the time of exposure by the National Research Council.[80] Note that the LAR values represent the number of additional cancer cases per 100,000 persons exposed to a single dose of 0.1 Gy. The average LAR values at 5 years of age for males and females were employed. Based on this data, the LAR of cancer incidence was estimated by multiplying the ratio of each organ dose to 0.1 Gy by the corresponding tabulated LAR value.

Estimates of lifetime relative risk (RR) of radiation-induced cancer were calculated on the basis of baseline (unexposed) values[76] for lifetime risk (LR) as follows:

$$RR = \frac{(LAR + LR)}{LR} \tag{18}$$

9.3. Results

As with Section 8.5, the highest absorbed doses were recorded for the skin, ascending colon and stomach for the abdominal pelvis CBCT protocol. Both standard dose and low dose mode showed the same pattern. The absorbed doses ranged from 0.0 to 7.2 cGy for the standard dose mode and from 0.0 to 1.6 cGy for the low dose mode. The absorbed doses for standard dose and low dose mode are respectively shown in FIG. 23 (a) and (b).

It was found that the standard deviation of image noise (HU) in the low dose mode is two times greater than the standard deviation of the HU in the standard dose mode, while a similar mean pixel value is maintained. However, as shown in FIG. 24, the image quality between standard and low dose modes was not substantially different and did not affect the patient localization process.

As with Section 8.5, the estimated ED was 37.8±0.7 mSv for the standard dose mode and 8.1±0.2 mSv for the low dose mode.

As can be seen in Table VIII, the LAR of cancer incidence for various organs ranged from 23 to 144 additional cases per 100,000 exposed individuals for standard dose mode, and from 5 to 31 additional cases per 100,000 exposed individuals for low dose mode. The RR of cancer incidence ranged from 1.003 to 1.053 for standard dose mode and from 1.001 to 1.012 for low dose mode.

9.4. Discussion

As Brenner has stated in his recent articles, children have a higher risk of cancer incidence from radiation than adults for several reasons[74,81,82]. First, their tissues are more rapidly proliferating than those of adults. Consequently, their cells are more radiosensitive. Second, their expected life time is longer than adults, so the likelihood for developing a radiation induced cancer is higher for children than for adults. Another consideration is the size of the body. The smaller body size of children usually results in

higher absorbed doses than for adults. This is because x-ray beams are less attenuated, before exposing deeper organs.

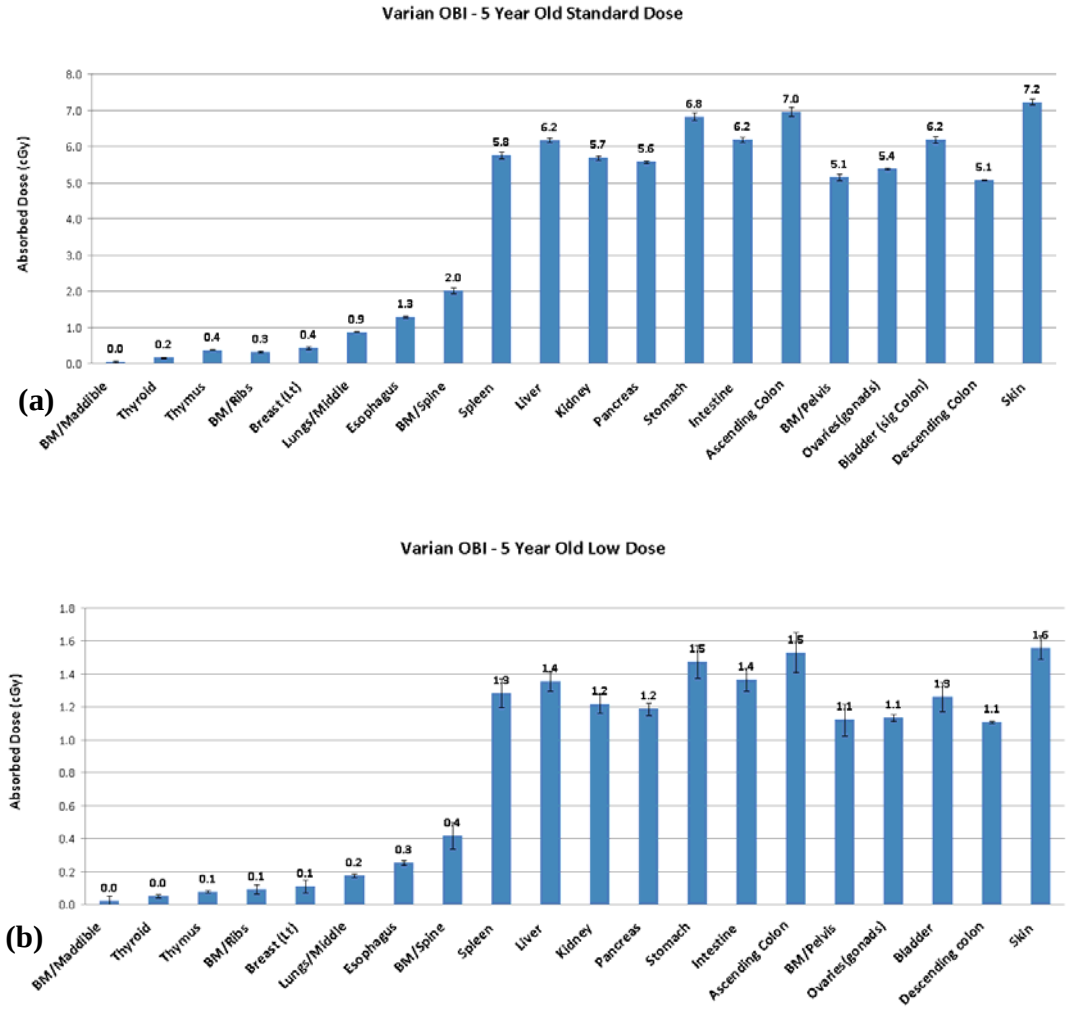

FIG. 23. Absorbed dose distribution from the abdominal CBCT for (a) standard dose mode and (b) low dose mode. Note that doses of skin, ascending colon, and stomach marked highest located in the irradiation field.

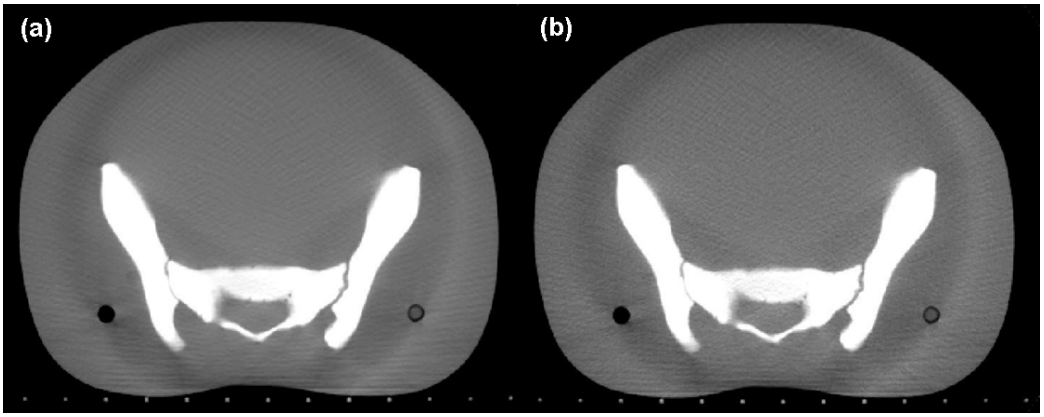

FIG. 24. (a) standard dose mode (125 kVp, 80 mA, 25 msec) and (b) low dose mode (125 kVp, 40 mA, 10 msec) images from pelvic cone beam CT. Note that the image noise increases in lower dose techniques (b), however this does not affect the ability to localize the patient based on bony structures.

Table VIII. LAR and RR of cancer incidence for various organs in standard and low dose CBCT modes.

Locations	Standard dose mode		Low dose mode	
	LAR*	RR	LAR*	RR
Colon	144	1.034	31	1.007
Stomach	51	1.053	11	1.012
Liver	23	1.049	5	1.011
Breast†	39	1.003	10	1.001
Lung	37	1.006	7	1.001
Bladder	112	1.050	22	1.010

*LAR is expressed as the number of additional cases of cancer attributable to radiation exposure per 100,000 exposed persons. †LAR and RR for breast cancer incidence were considered only for females.

Although this study discussed the risk of cancer incidence from pediatric CBCT in IGRT, the CBCT geometry is also widely used in diagnostic and interventional radiology these days. There is a 320-slice MDCT scanner commercially available for cardiothoracic CT applications in diagnostic radiology. Flat-panel CBCT machines are also frequently used in adult and pediatric interventional radiology. However, the dosimetry study related to the CBCT is still limited. More studies are needed to evaluate the CBCT dose more accurately, especially in children.

In this study, absorbed doses were measured with the pediatric phantom for the abdominal pelvis CBCT protocol. Because the MOSFET measurement data used in this study are the same as the previous study, all the discussion about the absorbed doses and ED can be referenced in Section 8.6.

It has been noticed that the image quality between standard dose and low dose mode does not affect the image guidance task in IGRT using bone structure despite the increase in image noise; thus radiation dose can be reduced in pediatric CBCT for IGRT.

It was also found that stomach cancer risk was highest in the RR estimation, while the colon cancer risk was highest in the LAR calculation. One should not be confused between these two quantities; the LAR accounts only for the cancer incidence from radiation exposure, while the RR considers both radiation-induced and non-radiation-induced cancer incidences.

The estimates of radiation risk, and their application to children in the U.S. population in this study, have several limitations. These have been discussed in detail

elsewhere.[79] Briefly, they include: (1) different baseline cancer incidence rates for the U.S. population and the populations reported in the BEIR VII document may limit the applicability of the LAR estimates; (2) the dose response curve in humans below 100 mSv is not well characterized, which may result in significant uncertainties in the parameters used to calculate relative risk in BEIR VII models; (3) diagnostic x-ray irradiation in the 80-140 kVp range may result in different rates of cancer induction than irradiation with high-energy gamma rays, upon which much of the BEIR VII tabulations are based; and (4) all such analyses are subject to common uncertainties such as sampling errors, incorrect diagnosis of cancer in the study populations, the use of an inappropriate dose response curve, uncertainties in the model parameters and so forth. Although the BEIR VII Committee introduced factors to correct for some of these limitations, the estimates of LAR and RR in this study represent expectation values only and are subject to the uncertainties.

Another limitation of this study is the quantification of radiation dose using an anthropomorphic phantom. Although this type of phantom would be expected to yield more accurate dose estimates than a phantom constructed of simple geometric shapes such as homogeneous ovoids or cylinders, it is still only a representative of a “standard” patient. Actual organ doses may vary among patients who may have different body habitus and body composition from the model we used.

9.5. Conclusion

In this study, absorbed doses were measured from pediatric CBCT protocols in an anthropomorphic phantom and ED, LAR and RR from the measurements were estimated. It was found that the ED for standard dose mode was higher than that of non-cone beam CT, while the ED for low dose mode was comparable. In the risk evaluation, it was found that the highest LAR were for incidence of colon and bladder and the highest RR were for incidence of stomach and liver cancer for the abdominal CBCT. As there is no technical difficulty for low dose mode CBCT to perform the image guidance task in IGRT based on bone structure localization, use of the pediatric CBCT with low dose mode should be considered to reduce the radiation exposure to the patients.

10. FUTURE WORKS

In this study, Monte Carlo (MC) approaches for CBCT dosimetry were investigated from x-ray tube model validation to effective dose (ED) estimation. The MC approach was found to be convenient (avoid labor intensive and time-consuming physical experiments) and relatively accurate comparing to the physical measurements, although it needs heavy computation time to achieve reasonable accuracy (2-5% statistical uncertainty). However, these drawbacks can be resolved by the use of high-performance computing environments such as supercomputers and computer clusters.

There is a limitation found in the organ and effective dose estimation study (Section 8); the study only considered point dose estimates due to the technical difficulties in physical measurements as well as image segmentation. However, it may be of interest to compare the limited point dose estimates of the measurements with average organ doses in MC simulations – this can provide the accuracy of the organ and effective dose estimation for the point dose measurements. The average organ doses can be derived from the MC results by segmenting individual organ doses with image segmentation techniques. For example, an organ consisting of bone material can be easily segmented from surrounding soft tissue by using the intensity threshold method or region growing technique (FIG. 25). This topic is a work-in-progress and will be fully investigated in the future.

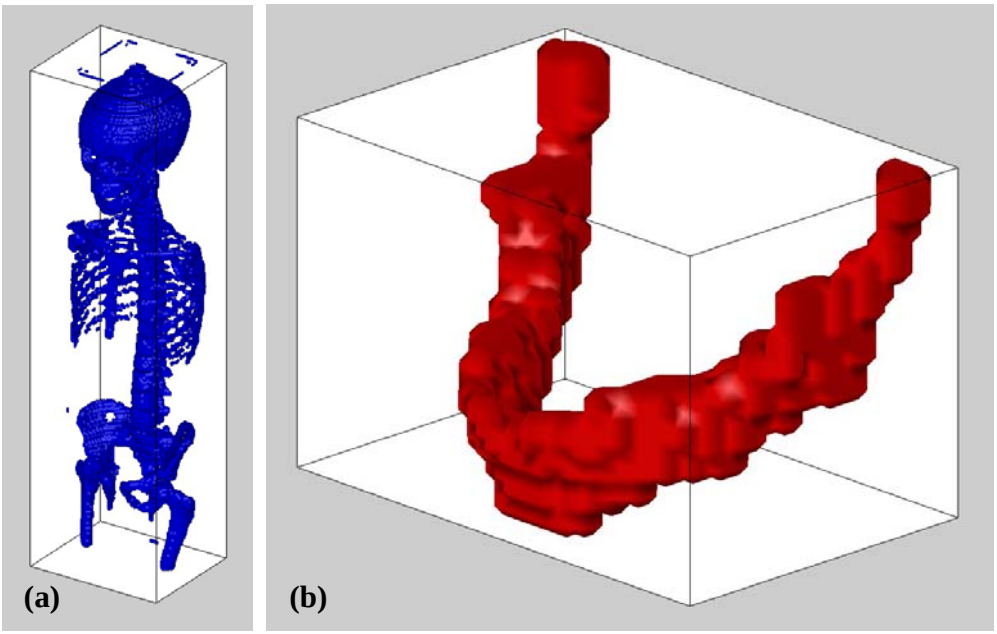

FIG. 25. (a) Whole body skeleton segmentation from a 5-year-old anthropomorphic phantom with intensity threshold method, (b) Mandible image segmented using region growing technique.

The MC approach used in this study can be easily extended to other diagnostic imaging modalities such as the multi-detector CT (MDCT) or interventional imaging system.

REFERENCES

[1]G. N. Hounsfield, "Computed Medical Imaging," Nobel lecture, December 8, 1979.

[2]J. T. Bushberg, J. A. Seibert, E. M. Leidholdt, Jr., and J. M. Boone, *The Essential Physics of Medical Imaging,* 2nd Ed. (Lippincott W. & W., NY, 2002).

[3]F. A. Mettler, B. R. Thomadsen, M. Bhargavan, D. B. Gilley, J. E. Gray, J. A. Lipoti, J. McCrohan, T. T. Yoshizumi, and M. Mahesh, "Medical radiation exposure in the U.S. in 2006: Preliminary results." Health. Phys. **95** (5), 502-507 (2008).

[4]T. B. Shope, R. M. Gagne, and G. C. Johnson, "A method for describing the doses delivered by transmission x-ray computed tomography," Med. Phys. **8** (4), 488-495 (1981).

[5]S. Mori, M. Endo, K. Nishizawa, T. Tsunoo, T. Aoyama, H. Fujiwara, and K. Murase, "Enlarged longitudinal dose profiles in cone-beam CT and the need for modified dosimetry," Med. Phys. **32** (4), 1061-1069 (2005).

[6]J. M. Boone, "The trouble with $CTDI_{100}$," Med. Phys. **34** (4), 1364-1371 (2007).

[7]R. L. Dixon, "A new look at CT dose measurement: beyond CTDI," Med. Phys. **30** (6), 1272-1280 (2003).

[8]K. D. Nakonechny, B. G. Fallone, and S. Rathee, "Novel methods of measuring single scan dose profiles and cumulative dose in CT," Med. Phys. **32** (1), 98-109 (2005).

[9]W. Y. Song, S. Kamath, S. Ozawa, S. Al Ani, A. Chvetsov, N. Bhandare, J. R. Palta, C. Liu, and J. G. Li, "A dose comparison study between XVI® and OBI® CBCT systems," Med. Phys. **35** (2), 480-486 (2008).

[10]D. W. O. Rogers, B. A. Faddegon, G. X. Ding, C. M. Ma, J. We, and T. R. Mackie, "BEAM: A Monte Carlo Code to Simulate Radiotherapy Treatment Units," Med. Phys. **22** (5), 503-524 (1995).

[11]D. W. O. Rogers, B. Walters, and I. Kawrakow, *BEAMnrc User Manual*, NRCC Report PIRS-0509(A)revK (NRCC, Ottawa, Canada, 2004).

[12]G. Jarry, J. J. DeMarco, U. Beifuss, C. H. Cagnon, and M. F. McNitt-Gray, "A Monte Carlo-based method to estimate radiation dose from spiral CT: from phantom testing to patient-specific models," Phys. Med. Biol. **48** (16), 2645-2663 (2003).

[13]G. X. Ding, D. M. Duggan, and C. W. Coffey, "Characteristics of kilovoltage x-ray beams used for cone-beam computed tomography in radiation therapy," Phys. Med. Biol. **52** (6), 1595-1615 (2007).

[14]G. X. Ding, D. M. Duggan, and C. W. Coffey, "Accurate patient dosimetry of kilovoltage cone-beam CT in radiation therapy," Med. Phys. **35** (3), 1135-1144 (2008).

[15]J. M. Hammersley, and D. C. Handscomb, *Monte Carlo methods*, (Methuen & Co, London, UK, 1964).

[16]I. Lux, and L. Koblinger, *Monte Carlo Particle Transport Methods: Neutron and Photon Calculations*, (CRC Press, Boca Raton, FL, 1991).
[17]R. Y. Rubinstein, *Simulation and the Monte Carlo Methods*, (John Wiley and Sons, New York, 1981).

[18]A. F. Bielajew, *Fundamentals of the Monte Carlo method for neutral and charged particle transport*, graduate course book of Monte Carlo Methods, (Department of Nuclear Engineering, University of Michigan, 2001).

[19]H. Kahn, "Use of different Monte Carlo sampling techniques," *Symposium on Monte Carlo Methods*, H. A. Meyer ed. (John Wiley and Sons, New York, 1956), pp. 146-190.

[20]J. H. Curtiss et al., Monte Carlo method, National Bureau of Standards Applied Mathematics Series 12.

[21]I. Kawrakow, D. W. O. Rogers, and B. R. B. Walters, "Large efficiency improvements in BEAMnrc using directional bremsstrahlung splitting," Med. Phys. **31** (10), 2883-2898, (2004).

[22]D. W. O. Rogers, and A. F. Bielajew, "Monte Carlo Techniques of Electron and Photon Transport for Radiation Dosimetry," *The Dosimetry of Ionizing Radiation,* K. R. Kase ed. (Academic Press, 1990), pp. 427-529.

[23]F. B. Brown, *Fundamentals of Monte Carlo Particle Transport*, Lecture Notes for Monte Carlo Course, LA-UR-05-4983, (Los Alamos National Laboratory).

[24]T. R. Mackie, S. S. Kubsad, D. W. O. Rogers, and A. F. Bielajew, "The OMEGA Project: Electron Dose Planning Using Monte Carlo Simulation," (Abstr.), Med. Phys. **17**, 732 (1990).

[25]E. Mainegra-Hing, and I. Kawrakow, "Efficient x-ray tube simulations," Med. Phys. **33** (8), 2683-2690 (2006).

[26]K. Cranley, B. J. Gilmore, G. W. A. Fogarty, and L. Desponds, *Catalogue of diagnostic x-ray spectra and other data*, IPFM Report 78 (Institute of Physics and Engineering in Medicine, York, 1997).

[27]D. W. O. Rogers, I. Kawrakow, J.P. Seuntjens, B.R.B. Walters, and E. Mainegra-Hing, *NRC User Codes for EGSnrc*, NRCC Report PIRS-702(revB) (NRCC, Ottawa, Canada, 2005).

[28]M. J. Berger, J. H. Hubbell, S. M. Seltzer, J. Chang, J. S. Coursey, R. Sukumar, and D. S. Zucker, *XCOM: Photon Cross Sections Database*, NIST (National Institute of Standards and Technology), WWW Document, (http://physics.nist.gov/PhysRefData/Xcom/Text/XCOM.html), Accessed on 10 June 2008.

[29]F. Hobeila, and J. P. Seuntjens, "Effect of XCOM photoelectric cross-sections on dosimetric quantities calculated with EGSnrc," Proc. IAEA-CN-96-17 (2003).

[30]W. R. Nelson, H. Hirayama, and D. W. O. Rogers, *The EGS4 code system*, Technical Report SLAC-265 (Stanford Linear Accelerator Center, 1985).

[31]B. Walters, I. Kawarakow, and D. W. O. Rogers, *DOSXYZnrc users manual*, NRCC Report PIRS-794revB (NRCC, Ottawa, Canada, 2004).

[32]C. -M. Ma, and D. W. O. Rogers, *BEAMDP users manual*, NRCC Report PIRS-0509(C)revA (NRCC, Ottawa, Canada, 2006).

[33]IXAS, *X-ray data for W*, IXAS (International X-ray Absorption Society), WWW Document, (http://csrri.iit.edu/cgi-bin/mucal-form?name=w), Accessed on 12 June 2008.

[34]S. Yoo, G. Kim, R. Hammoud, E. Elder, T. Pawlicki, H. Guan, T. Fox, G. Luxton, F. Yin, and P. Munro, "A quality assurance program for the on-board imager®," Med. Phys. **33** (11), 4431-4447 (2006).

[35]I. Kawrakow, *The dose visualization tool DOSXYZ_SHOW*, NRCC Report PIRS-0624 (NRCC, Ottawa, Canada, 2006).

[36]I. Kawrakow, M. Fippel, and K. Friedrich, "3D electron dose calculation using a Voxel based Monte Carlo algorithm (VMC)," Med. Phys. **23** (4), 445-457 (1996).

[37]F. Verhaegen, and S. Devic, "Sensitivity study for CT image use in Monte Carlo treatment planning," Phys. Med. Biol. **50** (7), 937-946 (2005).

[38]T. T. Yoshizumi, P. C. Goodman, D. P. Frush, G. Nguyen, G. Toncheva, M. Sarder, and L. Barnes, "Validation of metal oxide semiconductor field effect transistor technology for organ dose assessment during CT: comparison with thermoluminescent dosimetry," Am. J. Roentgenol. **188**, 1332-1336 (2007).

[39]Best Medical Canada, *Introduction to the MOSFET dosimeter*. Technical Note, TN#101248.04, WWW Document, (http://www.thomson-elec.com/global/pdf/technotes/te_4.pdf), Accessed on 16 July 2008.

[40]J. N. Rashu, and D. E. Hintenlang, "Characterization of the angular response of an isotropic MOSFET dosimeter," Health Phys. **84**, 376-379 (2003).

[41]A. B. Wolbarst, *Physics of Radiology*, with illustrations by G. Cook (Appleton & Lange, Norwalk, Connecticut, 1993).

[42]W. Leitz, B. Axelsson, and G. Szendro, "Computed tomography dose assessment – a practical approach," Radiat. Prot. Dosim. **57**, 377-380 (1995).

[43]D. M. Bakalyar, "A Critical look at the numerical coefficients in $CTDI_{VOL}$," Med. Phys. **33** (6), 2003-2003 (2006).

[44]J. Geleijns, M. Salvado Artells, P. W. de Bruin, R. Mather, Y. Muramatsu, and M. F. McNitt-Gray, "Computed tomography dose assessment for a 160 mm wide, 320 detector row, cone beam CT scanner," Phys. Med. Biol. 54, 3141-3159 (2009).

[45]R. L. Dixon, M. T. Munley, and E. Bayram, "An improved analytical model for CT dose simulation with a new look at the theory of CT dose," Med. Phys. 32, 3712-3728 (2005).

[46]R. L. Dixon and A. C. Ballard, "Experimental validation of a versatile system of CT dosimetry using a conventional ion chamber: Beyond CTDI100," Med. Phys. 34, 3399-3413 (2007).

[47]M. A. Stevens, J. R. Turner, R. P. Hugtenburg, and P. H. Butler, "High-resolution dosimetry using radiochromic film and a document scanner," Phys. Med. Biol. **41**, 2357-2365 (1996).

[48]P. Downes, R. Jarvis, E. Radu, I. Kawrakow, and E. Spezi, "Monte Carlo simulation and patient dosimetry for a kilovoltage cone-beam CT unit," Med. Phys. 36, 4156-4167 (2009).

[49]H. C. E. McGowan, B. A. Faddegon, and C. M. Ma, *STATDOSE for 3D dose distributions*, NRCC Report PIRS-0509(F) (NRCC, Ottawa, Canada, 2007).

[50]D. J. Brenner, C. H. McCollough, and C. G. Orton, "It is time to retire the computed tomography dose index (CTDI) for CT quality assurance and dose optimization," Med. Phys. **33**, 1189-1191 (2006).

[51]C. H. McCollough, and B. A. Schueler, "Calculation of effective dose," Med. Phys. **27**, 828-837 (2000).

[52]G. Drexler, W. Panzer, N. Petoussi, and M. Zankl, "Effective dose – how effective for patients?" Radiat. Environ. Biophys. **32**, 209-219 (1993).

[53]W. S. Snyder, H. L. Jr. Fisher, M. R. Ford, and G. G. Warner, "MIRD Pamphlet No.5: estimates of absorbed fractions for monoenergetic photon sources uniformly distributed in various organs of a heterogeneous phantom," J. Nucl. Med. **10**, 1-52 (1969).

[54]R. Kramer, M. Zankl, G. Williams, and G. Drexler, *The calculation of dose from external photon exposures using reference human phantoms and Monte Carlo methods. Part I. The male (Adam) and female (Eva) adult mathematical phantoms*, GSF report S-885. Neuherberg (1982).

[55]M. Cristy, and K. F. Eckerman, *Specific absorbed fractions of energy at various ages from internal photon sources*, Report ORNL/TM-8381 vol. 1-7 (Oak Ridge National Laboratory (ORNL), Oak Ridge, TN, 1987).

[56]I. G. Zubal, C. R. Harrell, E. O. Smith, Z. Rattner, G. Gindi, and P. B. Hoffer, "Computerized three-dimensional segmented human anatomy," Med. Phys. **21**, 299-302 (1994).

[57]R. Kramer, J. W. Viera, H. J. Khoury, and F. de Andrade Lima, "MAX meets ADAM: a dosimetric comparison between a voxel-based and a mathematical model for external exposure to photons," Phys. Med. Biol. **49**, 887-910 (2004).

[58]R. Kramer, H. J. Khoury, J. W. Vieira, E. C. M. Loureiro, J. V. M. Lima, F. R. A.Lima, and G. Hoff, "All about FAX: a Female Adult voXel phantom for Monte Carlo calculation in radiation protection dosimetry," Phys. Med. Biol. **49**, 5203-5216 (2004).

[59]M. Zankl, and A. Wittmann, "The adult male voxel model 'Golem' segmented from whole-body CT patient data," Radiat. Environ. Biophys. **40**, 153-162 (2001).

[60]X. G. Xu, T. C. Chao, and A. Bozkurt, "VIP-Man: An Image-Based Whole-Body Adult Male Model Constructed from Color Photographs of the Visible Human Project for Multi-Particle Monte Carlo Calculations," Health Phys. **78**, 476-486 (2000).

[61]R. Veit, W. Panzer, M. Zankl, and C. Scheurer, "Vergleich berechneter und gemessener dosen an einem anthropomorphen phantom," Z. Med. Phys. **2**, 123-126 (1992).

[62]M . Cohnen, L. W. Poll, C. Puettmann, K. Ewen, A. Saleh, and U. Modder, "Effective dose in standard protocols for multi-slice CT scanning," Eur. Radiol. **13**, 1148-1153 (2003).

[63]G. Brix, U. Lechel, R. Veit, R. Truckenbrodt, G. Stamm, E. M. Coppenrath, J. Griebel, and H. D. Nagel, "Assessment of a theoretical formalism for dose estimation in CT: an anthropomorphic phantom study," Eur. Radiol. **14**, 1275-1284 (2004).

[64]P. Deak, M. van Straten, P. C. Shrimpton, M. Zankl, and W. A. Kalender, "Validation of a Monte Carlo tool for patient-specific dose simulations in multi-slice computed tomography," Eur. Radiol. **18**, 759-772 (2008).

[65]L. Struelens, F. Vanhavere, and K. Smans, "Experimental validation of Monte Carlo calculations with a voxelized Rando-Alderson phantom: a study on influence parameters," Phys. Med. Biol. **53**, 5831-5844 (2008).

[66]R. Fahrig, R. Dixon, T. Payne, R. L. Morin, A. Ganguly, and N. Strobel, "Dose and image quality for a cone-beam C-arm CT system," Med. Phys. **33**, 4541-4550 (2006).

[67]International Commission on Radiological Protection. *Report on the task group on reference man*, ICRP Publication 23, (Oxford: Pergamon Press, 1975).

[68]International Commission of Radiation Units and Measurements. *Tissue substitutes in radiation dosimetry and measurement*, ICRU Report 44, (IRCU: Bethesda, MD, 1989).

[69]International Commission on Radiological Protection, *1990 Recommendations of ICRP*, ICRP Publication 60, Ann. ICRP **21**(1-3) (Oxford: Elsevier Science Ltd, 1991).

[70]International Commission on Radiological Protection, *Age-dependent doses to members of the public from intake of radionuclides: Part 2: ingestion dose coefficients*, ICRP Publication 67, Ann. ICRP **23**(3/4) (Oxford: Elsevier Science Ltd, 1993).

[71]C. Kawaura, T. Aoyama, S. Koyama, M. Achiwa, and M. Mori, "Organ and effective dose evaluation in diagnostic radiology based on in-phantom dose measurements with novel photodiode-dosemeters," Radiat. Prot. Dosim. **118**, 421-430 (2006).

[72]International Commission on Radiological Protection, *Basic anatomical & physiological data for use in radiological protection: The skeleton*, ICRP Publication 70, Ann. ICRP **25**(2) (Oxford: Elsevier Science Ltd, 1996).

[73]National Institute of Standards and Technology. *X-ray mass attenuation coefficients – Polymethyl Methacrylate (PMMA) and Air, Dry (near sea level)*, WWW Document, (http://physics.nist.gov/PhysRefData/XrayMassCoef/tab4.html), Accessed on Jan. 06, 2009.

[74]D. J. Brenner, "Estimating cancer risks from pediatric CT: going from the qualitative to the quantitative," Pediatr. Radiol. **32**, 228-231 (2002).

[75]K. E. Thomas, and B. Wang, "Age-specific effective doses for pediatric MSCT examinations at a large children's hospital using DLP conversion coefficients: a simple estimation method," Pediatr. Radiol. **38**, 645-656 (2008).

[76]T. T. Yoshizumi, P. C. Goodman, D. P. Frush, G. Nguyen, G. Toncheva, M. Sarder, and L. Barnes, "Validation of Metal Oxide Semiconductor Field Effect Transistor Technology for Organ Dose Assessment During CT: Comparison with Thermoluminescent Dosimetry," Am. J. Roent. **188**, 1332-1336 (2007).

[77]M. K. Islam, T. G. Purdie, B. D. Norrlinger, H. Alasti, D. J. Moseley, M. B. Sharpe, J. H. Siewerdsen, and D. A. Jaffray, "Patient dose from kilovoltage cone beam computed tomography imaging in radiation therapy," Med. Phys. **33**, 1573-1582 (2006).

[78]N. Wen, H. Guan, R. Hammoud, D. Pradhan, T. Nurushev, S. Li, and B. Movsas, "Dose delivered from Varian's CBCT to patients receiving IMRT for prostate cancer," Phys. Med. Bio. **52**, 2267-2276 (2007).

[79]L. M. Hurwitz, R. E. Reiman, T. T. Yoshizumi, P. C. Goodman, G. Toncheva, G. Nguyen, and C. Lowry, "Radiation dose from contemporary cardiothoracic multidetector CT protocols with an anthropormorphic female phantom: Implications for cancer induction," Radiology **245**, 742-750 (2007).

[80] National Research Council, Committee to Assess Health Risks from Exposure to Low Levels of Ionizing Radiation, *Health risks from exposure to low levels of ionizing radiation: BEIR VII phase 2*, (National Academies, Washington, DC, 2006).

[81]D. J. Brenner, "Estimated risks of radiation-induced fatal cancer from pediatric CT," Am. J. Roent. **176**, 289-296 (2001).

[82]D. J. Brenner, C. D. Elliston, E. J. Hall, "Estimates of the cancer risks from pediatric CT radiation are not merely theoretical," Med. Phys. **28**, 2387-2388 (2001).

BIOGRAPHY

Sangroh Kim

Citizenship The Republic of Korea

EDUCATION

Duke University, Durham, North Carolina
Ph.D. in Medical Physics, 2010

Duke University, Durham, North Carolina
MS in Medical Physics, 2007

The Catholic University of Korea, Seoul, Korea
MS in Medical Physics, 2003

KAIST (Korea Advanced Institute of Science and Technology), Daejon, Korea
BS in Nuclear Engineering, 2001
*Finished Korean military duty from 07/95 to 09/97

ACADEMIC ACHIEVEMENTS

Mar 13, 2009 **Best Student Paper Award,** S. Kim, T. Yoshizumi, G. Toncheva, F. Yin, and D. Frush, "A Monte Carlo dose estimation method using a voxelized phantom for pediatric CBCT." from North Carolina Health Physics Society

2007 – 2008 **Carestream Health Fellowship**, Carestream Health

May 9, 2007 **Award for Excellence in Research** in Medical Physics Graduate Program at Duke University

03/01 – 02/03 **Half Tuition Waiver Scholarship** in the Catholic University of Korea

07/02 – 08/02 Visit **MIR (Mallinckrodt Institute of Radiology)** for Master Thesis Research

Sept 99 **Department Scholarship in KAIST**

ACADEMIC ACTIVITIES

08/08 – 01/09 **Teaching Assistant – MP210 Radiation protection**
Taught students radiation protection, regulation and shielding techniques. (Instructor: Terry T. Yoshizumi, PhD)

01/08 – 05/08 **Teaching Assistant – MP322 Advanced photon beam radiation therapy**
Taught students MATLAB programming of 2D/3D treatment planning and IMRT optimization. (Instructor: Shiva K. Das, PhD)

INTERNSHIPS

Winter 1999 B.S. Thesis Research in **KINS (Korea Institute of Nuclear Safety)**
Researched into the analysis of nuclear power plant safety for the BS degree.

EMPLOYMENTS

01/04 – 06/05 **Research Scholar**, Case Western Reserve University, Cleveland, Ohio
Researched the topic; "Three-Dimensional Surface Image Registration for Image-Guided Radiation Therapy to Breast".

09/03 – 12/03 **Researcher**, the Catholic University of Korea, Seoul, Korea
Researched **IMRT/IGRT** and involved in **RTP development project** with Seoul C&J Inc.

MEMBERSHIP

09/04 – Pres. American Association of Physicists in Medicine (AAPM) student member.

09/06 – Pres. Health Physics Society (HPS) student member.

EXTRA-CURRICULAR ACTIVITIES

03/93 – 02/01 Producer in VOK (Voice of KAIST)
Produced some school broadcasting programs in KAIST.

PUBLICATIONS

S. Kim, H. Song, E. Samei, F. Yin, and T. Yoshizumi, "**Computed tomography dose index and dose length product for cone-beam CT: Monte Carlo simulations of a commercial system**," Med. Phys. (submitted).

S. Kim, S. Yoo, F. Yin, E. Samei, and T. Yoshizumi, "**Kilovoltage cone-beam CT: comparative dose and image quality evaluations in partial and full-angle scan protocols**," Med. Phys. (tentatively accepted).

S. Kim, T. Yoshizumi, G. Toncheva, F. Yin, and D. Frush, "**Radiation Dose from Cone Beam Computed Tomography in a Pediatric Phantom: Risk Estimation of Cancer Incidence,"** Am. J. Roent. 194, 1-5 (2010).

S. Kim, T. Yoshizumi, G. Toncheva, D. Frush, and F. Yin, "**Estimation of Absorbed Doses from Pediatric Cone-Beam CT Scans: MOSFET Measurements and Monte Carlo Simulations**," Radiat. Prot. Dosim. Advance access published on Nov. 4, (2009).

S. Kim, T. Yoshizumi, G. Toncheva, S. Yoo, F. Yin, and D. Frush, "**Estimation of Computed Tomography Dose Index in Cone Beam Computed Tomography: MOSFET Measurements and Monte Carlo Simulations**," Health Phys. (in press).

S. Kim and T. Suh, "**Characterization of Generalized Elliptical Sources in a Medical Linear Accelerator by Using the BEAMnrc/EGSnrc Monte Carlo System**," JKPS. **55** (4), 1632-1639 (2009).

S. Kim, "**Characteristics of elliptical sources in BEAMnrc Monte Carlo system: implementation and application**," Med. Phys. **36** (4), 1046-1052 (2009).

S. Kim, T. T. Yoshizumi, D. Frush, C. Anderson-Evans, and G. Toncheva, "**Dosimetric Characterization of Bismuth Shields in Computed Tomography: Measurements and Monte Carlo Simulations,"** Radiat. Prot. Dosim. **133** (2), 105-110 (2009).

S. Kim, G. Toncheva, C. Anderson-Evans, B. K. Huh, L, Gray, and T. Yoshizumi, "**The Kerma Air Product (KAP) Method for the Effective Dose Estimation in Lumbar Epidural Steroid Injection Procedure: Phantom Study,"** Am. J. Roent. **192** (10) (2009).

S. Kim, T. T. Yoshizumi, G. Toncheva, S. Yoo, and F. Yin, "**Comparison of Radiation Doses between Cone Beam CT and Multi Detector CT: TLD Measurements,"** Radiat. Prot. Dosim. **132** (3), 339-345 (2008).

M. D. Lin, G. Toncheva, G. Nguyen, S. Kim, C. Anderson-Evans, G.A. Johnson and T.T. Yoshizumi, "**Application of MOSFET Detectors for Dosimetry in Small Animal Radiography Using Short Exposure Times,"** Radiat. Res. **170**, 260-263 (2008).

S. Kim, J. Sohn and T. Suh, "**Comparison of Film Measurements, Convolution/superposition Model and Monte Carlo Simulations for Small fields in Heterogeneous Phantoms,"** Journal of Biomedical Engineering Research (Korean), **25** (2), 89-95 (2004).

S. Kim, B. Cho, T. Suh, H. Bae, B. Choi, and H Lee, "**Preliminary Study for Clinical Application of Virtual micro-IMRT Technique,"** The Journal of Medical Physics in Korea, **13** (1), (2002).

PRESENTATIONS

Oral Presentations

S. Kim*, T. Yoshizumi, D. Frush, C. Anderson-Evans, G Toncheva, "**Dose Reductions of Bismuth Shields in Diagnostic Radiology: Measurements and Monte Carlo Simulations,** Med. Phys. AAPM 2009.

S. Kim*, T. Yoshizumi, G. Toncheva, F. Yin, D. Frush, **A Monte Carlo Dose Estimation Method Using A Voxelized Phantom for Pediatric CBCT,** Health Phys. 2009.

S. Kim*, S. Yoo, B Koonts, S. Das, M. Anscher, F. Yin, **Dosimetric Evaluation of Prostate IMRT Treatments Positioned Based On Cone-Beam CT**, Med. Phys. AAPM Vol. 33, No 6, p. 2254, 2006.

B. Koontz, S. Yoo, S. Kim, S. Das, M. Anscher, F. Yin, **Evaluation of Adequate Margin Size for Prostate IMRT by Cone-Beam CT Interfraction Imaging,** Int. J of Radiat. Oncol. Biol. Phys. ASTRO Vol. 66 No 3, p. S623, 2006.

J. Sohn*, S. Kim, J. Monroe, A. Chvetsov, B. Wessels, **Human and System Error Analysis of a 3D Optical Laser Scanning System for Image-Guided Patient Positioning,** AAPM meeting, 2005.

J. Sohn*, S. Kim, et al, **Surface Image Registration For Image-Guided IMRT To Breast**, The 14th International Conference on the use of computers in Radiation Therapy, 2004.

J. Sohn*, S. Kim, et al, **Three-Dimensional Surface Image Registration for Image-Guided IMRT to Breast**, AAPM meeting, 2004.

S. Kim*, J.W. Sohn and T.S. Suh, **Comparison Of Film Measurements, Convolution/Superposition And Monte Carlo Calculations For Small Field In**

Heterogeneous Phantoms, WC2003.

S. Kim*, J. Sohn, T. Suh, **Comparison of Measurements with Radiochromic Films and Monte Carlo Simulation for Small Beams in Heterogeneous Phantoms**, Med. Phys. AAPM, Vol. 29, No 6, 2002.

S.Kim*, J. Sohn, T. Suh, et al, **6MV Photon Beam Commissioning in Varian 2300C/D with BEAM/EGS4 Monte Carlo Code**, The 3th Korea-Japan Joint Meeting On Medical Physics and The 2nd Asia Oceania Congress of Medical Physics, 2002.

S. Kim*, B. Cho, et al., **Preliminary Study for Clinical Application of Virtual micro-IMRT Technique,** KSMP, 2001.

Poster Presentations

S. Kim, T. Yoshizumi, G. Toncheva, F. Yin, D. Frush, **Eradiation Dose Estimation from Pediatric Cone Beam Computed Tomography,** AAPM, 2009.

S. Kim, G. Toncheva, C. Anderson-evans, B. Huh, L. Leithe, T.T. Yoshizumi, **Effective Dose Measurement in Pain Clinic Using an Adult Male Anthropomorphic Phantom and Derivation of Dose Conversion Coefficient from Dose Area Product (DAP).** HPS, 2008.

S. Yoo, S. Das, S. Kim, B. Koontz, W. Lee, K. Light, F. Yin, **Dosimetric Comparison of Patient-Specific Margins Vs. Uniform Margins for Prostate IMRT Treatments**, AAPM, 2007.

S. Stakhursky, S. Das, S. Yoo, F. Yin, S. Kim, B. Koontz, **Estimation of Dose Variations During Prostate Radiation Treatment Due to Elastic Deformations of Soft Tissues**, AAPM, 2007.

S. Kim, T. Yoshizumi, F. Yin, **Implementation of Helical CT Source in DOSXYZnrc/EGSnrc Monte Carlo Code**, AAPM, 2007.

S. Kim, S. Yoo, T. Yoshizumi, F. Yin, **Monte Carlo Benchmark for Radiation Dose Assessment in Varian On-Board Imager**, AAPM, 2007.

J. Sohn, S. Kim, J. Monroe, B, Wessels, **Breast Image-Guided Radiation Therapy Using an Optical Laser Scanner**, ASTRO, 2005.

T. Suh, K. Cheong, J. Song, S. Oh, S. Kim, C. Yoo, J. Choi, **Development of the new PC based 3D radiation therapy planning systems for the optimal plan**, Korea Radiation Protection Society Meeting, 2004.

S. Kim, T. Suh, et al, **The Separation of Phase Space in BEAM/EGS4 Monte Carlo Simulation**, KSMP, 2003.

- S. Kim, J. Sohn, and T. Suh, **Comparison of Film Measurements, Convolution and Monte Carlo Dose Calculation Methods in Small Field IMRT**, The First Asia Oceania Congress for Radiation Protection, 2002.

S. Kim, J. Sohn, T. Suh, et al, **Comparison of Dose Calculations in Convolution/Superposition Method and Monte Carlo Simulations for Small Beams in Heterogeneous Phantoms**, KOSOMBE, KOSTRO, 2002.

S. Kim, B. Cho, et al., **Preliminary Study for Clinical Application of Virtual micro-IMRT Technique**, KOSOMBE, 2001.